



Universiteit
Leiden
The Netherlands

Where photons meet phonons

Buters, F.M.

Citation

Buters, F. M. (2017, December 21). *Where photons meet phonons. Casimir PhD Series*. Retrieved from <https://hdl.handle.net/1887/58471>

Version: Not Applicable (or Unknown)

License: [Licence agreement concerning inclusion of doctoral thesis in the Institutional Repository of the University of Leiden](#)

Downloaded from: <https://hdl.handle.net/1887/58471>

Note: To cite this publication please use the final published version (if applicable).

Cover Page



Universiteit Leiden



The handle <http://hdl.handle.net/1887/58471> holds various files of this Leiden University dissertation.

Author: Buters, F.M.

Title: Where photons meet phonons

Issue Date: 2017-12-21

Where photons meet phonons

PROEFSCHRIFT

TER VERKRIJGING VAN
DE GRAAD VAN DOCTOR AAN DE UNIVERSITEIT LEIDEN,
OP GEZAG VAN RECTOR MAGNIFICUS PROF. MR. C.J.J.M. STOLKER,
VOLGENS BESLUIT VAN HET COLLEGE VOOR PROMOTIES
TE VERDEDIGEN OP DONDERDAG 21 DECEMBER 2017
KLOKKE 11:15 UUR

DOOR

Frank Maurice Buters

GEBOREN TE VELSERBROEK
IN 1989

Promotor: Prof. dr. D. Bouwmeester

Promotiecommissie: Prof. dr. A. Schliesser (University of Copenhagen)
Dr. P.-F. Cohadon (UPMC Laboratoire Kastler Brossel)
Prof. dr. E. Verhagen (AMOLF and TU Eindhoven)
Dr. M.J.A. de Dood
Dr. ir. S.J. van der Molen
Prof. dr. J.M. van Ruitenbeek
Prof. dr. E.R. Eliel

Casimir PhD series, Delft - Leiden 2017 - 34

ISBN 978-90-8593-318-2

An electronic version of this thesis can be found at:
<https://openaccess.leidenuniv.nl>

The work described in this thesis was performed at the Huygens - Kamerlingh Onnes Laboratory, Leiden University of Physics, Leiden University, The Netherlands. This work is part of the research program of the Foundation for Fundamental Research (FOM), which is part of the Netherlands Organization for Scientific Research (NWO).

The back cover shows an optical image of a trampoline resonator fabricated by Matthew Weaver at UCSB. This trampoline resonator is used throughout this thesis to investigate the interaction of a mechanical resonator coupled to an optical cavity.

We zijn hier aan de oever van een machtige rivier
De andere oever is daarginds, en deze hier is hier
De oever waar we niet zijn noemen wij de overkant
Die wordt dan deze kant zodra we daar zijn aangeland
En dit heet dan de overkant, onthoudt u dat dus goed
Want dat is van belang voor als u oversteken moet
Dat zou nog best eens kunnen, want er is hier veel verkeer
En daarom vaar ik steeds maar vice versa heen en weer

Drs. P
uit: *Veerpont*
Polydor, 1973

Contents

1	Introduction	1
1.1	Radiation pressure	1
1.2	Macroscopic superposition	1
1.3	Overview of this thesis	3
2	Theory and Experimentals	5
2.1	Optomechanical equations of motion	5
2.1.1	Uncoupled equations	5
2.1.2	Optomechanical interaction	7
2.1.3	Optical cooling	10
2.2	Experimentals	13
2.2.1	Optical bench	13
2.2.2	Trampoline resonators	14
2.2.3	Aligning the optical bench	16
2.2.4	Performing an optomechanical experiment	17
3	Experimental exploration of the optomechanical attractor diagram and its dynamics	21
3.1	Introduction	22
3.2	Theoretical model	22
3.3	Experimental setup	24
3.4	Results	25
3.5	Conclusion	30
4	A simple method to measure optomechanically induced transparency	33
4.1	Introduction	34
4.2	Theory	35
4.3	Experimental details	37

4.4	Results	39
4.5	Conclusion	42
5	Optical side-band cooling of a low frequency optomechanical system	45
5.1	Introduction	46
5.2	Experiment	47
5.3	Results and discussion	49
5.4	Conclusion	52
6	Optomechanics with a polarization nondegenerate cavity	53
6.1	Introduction	54
6.2	Experimental details	54
6.3	Results	56
6.4	Conclusion	60
7	Intermezzo: picking up not-so-good vibrations	61
7.1	The issue of vibrations	61
7.2	Low frequency vibrations	61
7.2.1	Introduction	61
7.2.2	Theory	62
7.2.3	Combining with optomechanical interaction	66
7.2.4	Comparison with experiment	68
7.2.5	High-Q metals at low temperatures	68
7.3	Noise from sample	70
8	Optomechanical cooling with a nested resonator	73
8.1	Introduction	74
8.2	Optical cooling	75
8.3	Model of a nested resonator	78
8.4	Conclusions	81
9	High-Q nested resonator in an actively stabilized optomechanical cavity	83
9.1	Introduction	84
9.2	Experimental details	84
9.3	Results	86
9.3.1	Active feedback cooling	86
9.3.2	Active stabilization	88
9.4	Conclusion	89
10	Optomechanical experiments in a cryogen free dilution refrigerator	91
10.1	Mechanical low-pass filters	91
10.1.1	Correspondence between electrical and mechanical networks	92
10.1.2	Mechanical low-pass filter	94
10.2	Optical side-band cooling at cryogenic temperatures	98
10.2.1	Measurements at 5.7 Kelvin	98
10.2.2	Thermalization of the trampoline resonator	101

11 Outlook: High-Q membranes, Coherent state transfer and Future directions	107
11.1 High-Q silicon nitride membranes	108
11.2 Coherent optomechanical state transfer	110
11.3 The optimal platform to investigate optomechanical state transfer . . .	114
Bibliography	115
Samenvatting	127
Acknowledgment	129
Curriculum vitae	131
List of publications	134

1.1 Radiation pressure

Light has some truly amazing properties which has puzzled scientists for many centuries. Nothing can move faster than the speed of light and light can be considered both as a wave and a particle. As a particle, light has zero rest mass, while when reflecting off a surface it does exert a force. The concept of this force or radiation pressure, is already centuries old. In 1619 Kepler, based on observations by Brahe, suggested the existence of radiation pressure from observing the tail of a comet [1]. Kepler observed that a comet has two tails, of which one always points away from the sun. It took, however, more than 200 years for theory to catch up with observations. Maxwell's theory of electromagnetism [2] showed that electromagnetic waves carry momentum and can therefore exert a force. In 1901, Lebedev [3] and Nicholas and Hull [4] used a torsion balance to confirm Maxwell's theory, while carefully accounting for any thermal effects. This is perhaps the first optomechanical experiment.

Meanwhile, measurements of black body radiation let Planck to suggest in 1901 that the energy in electromagnetic waves might be released in packets of energy [5]. In 1905, Einstein supported this idea and named such package a "light quantum" [6]. The theory of quantum mechanics was soon developed afterwards.

1.2 Macroscopic superposition

To highlight the peculiar nature of quantum mechanics, Schrödinger proposed a thought experiment involving a cat whose fate was tied to the state of a radioactive atom [7]. Both the cat and the atom are placed together in a box. When the atom decays, a Geiger counter registers this decay upon which a deadly toxin is released and the cat dies. When the box is closed, we do not know the state of the atom and therefore also not the state of the cat. The cat is in a superposition between alive and dead. Such a superposition state is common in quantum mechanics, but certainly

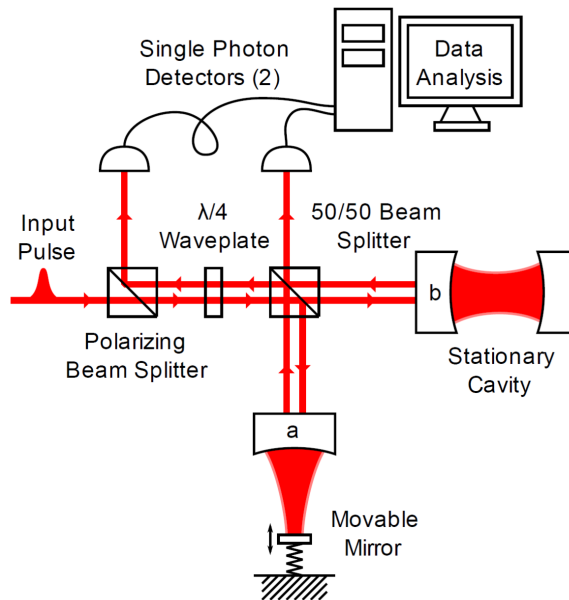


Figure 1.1: Schematic overview of the experiment proposed by Marshall et al.[8]. Figure is adapted from [9].

not in the everyday world. It is of course tempting, but not really ethical, to perform such an experiment with animals to find out where the border lies between quantum and classical. Fortunately several analogous experiments are possible to investigate the quantum to classical transition.

In 2003, Marshall et al. [8] proposed an optomechanical equivalent to this experiment. A schematic overview of the proposal is shown in Fig. 1.1. Ignoring for now the polarizing beam splitter and $\lambda/4$ waveplate, an input pulse consisting of a single photon is sent to a 50/50 beam splitter. After the 50/50 beam splitter, the photon ends up simultaneously in cavity A and cavity B. In cavity A, the photon will hit a movable mirror, which, due to the radiation pressure exerted by the photon, starts to move a little bit. Since beforehand the path of the photon is not known, the state of the movable mirror, namely standing still or moving a little, is also not known. Similar to Schrödinger's cat, the path the photon takes (the atom) is entangled with the state of the mirror (the cat).

This is where the analogy ends between the experiment proposed in Fig. 1.1 and Schrödinger's thought experiment. With the cat in the box, the only way to check if the cat is still alive is to open the box and look. No information about the state of the cat leaves the box as long as the box is closed. This is not true for the photon and the movable mirror, since the photon, which is simultaneously in cavity A and B, will leak out of the cavities back onto the 50/50 beam splitter. Depending on the state of the movable mirror, this photon is detected on either one of the single photon detectors. The precise details regarding the photon detection will not be discussed now, but the crucial part is that the experiment can be repeated many times to build

up statistics on the state of the mirror as function of time. This will reveal in the end the lifetime of the superposition state.

The creation of such a macroscopic superposition state is in itself already interesting to explore, irrespectively of whether there are limits to quantum mechanics. The experiment, however, looks also beyond the known theories of quantum mechanics. Several ideas have been proposed, such as continuous spontaneous localization (CSL) and gravitationally induced decoherence [10, 11, 12, 13], suggesting that a superposition state involving a macroscopically sized object will be short lived. These theories can in principle be tested using the scheme depicted in Fig. 1.1.

1.3 Overview of this thesis

Although the scheme depicted in Fig. 1.1 is highly simplified, and more elaborate versions are already proposed [14, 15], an essential requirement for all proposals is the state of the movable mirror at the start of the experiment. In order for the interaction with a single photon to have maximal effect, the movable mirror should stand as still as possible. This is only achieved by cooling down the mirror to ultra low temperatures (below 10 microKelvin). In this thesis, a combination of optical and cryogenic cooling is investigated to reach these temperatures.

First in chapter 2 the necessary theory to describe an optical cavity with movable mirror (cavity A in Fig. 1.1) is presented. In chapter 2 also some of the experimental details are discussed, for example the movable mirror, which in this work is a trampoline resonator.

Chapters 3 and 4 deal with the dynamics of such an optomechanical cavity. In particular, the mechanical motion of the movable mirror can not only be cooled, but also driven, either using a single laser (chapter 3) or multiple lasers (chapter 4). In chapter 5 the core method of optical cooling is demonstrated. This method is also used in Chapter 6 to highlight how the polarization of light can play an important role in optomechanical systems in general.

In chapter 7 a full numerical simulation is presented to investigate how mechanical noise can influence our experiment. To isolate the movable mirror better from unwanted vibrations, a new type of trampoline resonator, the nested resonator, was designed. The first measurements using this new type of resonator are reported in chapter 8. In chapter 9, additional control for the nested trampoline resonator was implemented, improving the overall performance.

In chapter 10, all experimental techniques are combined, together with an improved vibration isolation system to perform optical cooling at cryogenic temperatures. Finally, chapter 11 presents initial measurements of a new method to create a macroscopic superposition state and discusses which optomechanical system is based suited to demonstrate this method in the quantum regime.

Theory and Experimentals

In this chapter we present a derivation of the optomechanical equations of motions and connect these to observable quantities. In the second part of this chapter a brief overview of the experimental set-up and methods is presented. Both the theory and experimental details form the basis for the following chapters.

2.1 Optomechanical equations of motion

Although the field of cavity optomechanics contains a wide variety of optical and microwave cavities coupled to an assortment of mechanical oscillators (see Ref. [16] for an overview), most systems can be represented by the schematic picture in Fig. 2.1. In such a Fabry-Perot cavity, the displacement of the mirror is parametrically¹ coupled to the cavity field, leading to intricate dynamics. Since most of the work presented in this thesis is classical, we will derive the semi-classical equations of motions because these provide a more intuitive understanding of the physics involved. The approach presented here is inspired by the work of Schliesser [17] and Rivière [18]. A more detailed Hamiltonian description is presented in the work of Law [19] and a quantum mechanical treatment can be found in the works of Marquardt [20] and Wilson-Rae [21].

2.1.1 Uncoupled equations

As can be seen from Fig. 2.1, the two main ingredients are a harmonic oscillator and an optical cavity. First we consider the harmonic oscillator and cavity separately. The motion of the harmonic oscillator is described by the following differential equation:

$$\frac{d^2 x(t)}{dt^2} = -\Gamma_m \frac{dx(t)}{dt} - \Omega_m^2 x(t) + \frac{F_{ex}}{m} \quad (2.1)$$

¹A parametric oscillator is an oscillator of which one parameter varies with time. In an optomechanical system, the cavity field varies with the frequency of the mechanical resonator, leading to a resonant optical force.

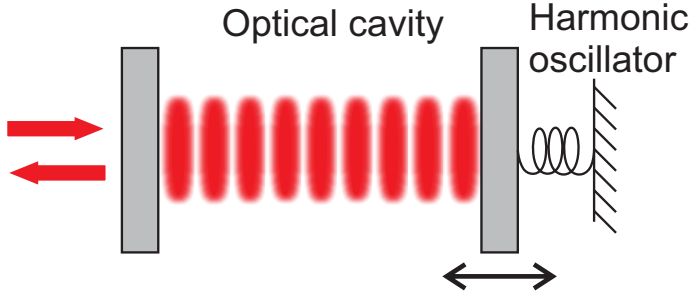


Figure 2.1: Schematic overview of an optomechanical system. In a Fabry-Perot cavity with one moving end mirror the motion of the harmonic oscillator is parametrically coupled to the cavity field.

where we have defined the mechanical displacement $x(t)$, the mechanical damping rate Γ_m , the mechanical frequency Ω_m , the mode mass m and some external force F_{ex} .

Eq. (2.1) can be solved easily by introducing the Fourier transform $x(\omega) = \int_{-\infty}^{\infty} x(t)e^{i\omega t} dt$. The solution can then be written as $x(\omega) = \chi_{xx}F_{ex}(\omega)$ where χ_{xx} is the mechanical susceptibility defined as:

$$\chi_{xx}(\omega) = (m(\Omega_m^2 - \omega^2) - im\Gamma_m\omega)^{-1}. \quad (2.2)$$

When Γ_m is small, this equation is well described by a Lorentzian:

$$\chi_{xx}(\omega) = (m\Omega_m[2(\Omega_m - \omega) - i\Gamma_m])^{-1}.$$

A Fabry-Perot cavity is typically described in terms of the circulating electrical field E_{circ} : [22]²

$$E_{circ} = t_1 E_{inc} + r_1 r_2 e^{-2i\phi} E_{circ} \quad (2.3)$$

where E_{inc} is the incoming electrical field, t_1 the amplitude transmission coefficient of the entrance mirror, r_1 and r_2 the amplitude reflection coefficient of both mirrors and ϕ the phase acquired after one round-trip through the cavity. This equation is useful to describe the steady state of an optical cavity. However, we are interested in the dynamics of the circulating intensity inside the cavity, as will become clear in the next section. It is therefore useful to describe the field inside the optical cavity in terms of a complex mode amplitude $\alpha(t)$ which is normalized such that $|\alpha(t)|^2$ is the photon number or stored energy [23]:

$$\frac{d\alpha(t)}{dt} = -\frac{\kappa}{2}\alpha(t) - i\omega_{cav}\alpha(t) + \sqrt{\kappa_{ex}}\sigma_{in}(t) \quad (2.4)$$

where we have defined the optical decay rate κ , the cavity frequency ω_{cav} , the external optical coupling rate κ_{ex} and the optical input power σ_{in} . An elegant classical

²Equation (2.3) describes only the magnitude of the circulating electrical field. The spatial profile can be described using Hermite-Gaussian modes. In this thesis only the fundamental Hermite-Gaussian mode is used.

derivation of this equation using an LC-circuit as an example is provided by Haus [23] while a quantum treatment is given by Gardiner and Collet [24].

To solve Eq. (2.4), it is convenient to choose a coordinate frame rotating with the laser frequency ω_L by defining $\alpha(t) = a(t)e^{-i\omega_L t}$ and $\sigma_{in}(t) = s_{in}(t)e^{-i\omega_L t}$. This yields the following equation:

$$\frac{da(t)}{dt} = (i\Delta - \frac{\kappa}{2})a(t) + \sqrt{\kappa_{ex}}s_{in}(t) \quad (2.5)$$

where the laser detuning Δ is introduced as the difference between laser and cavity frequency, $\Delta = \omega_L - \omega_{cav}$. Typically negative or red detuning is used to indicate a laser with a frequency lower than the cavity resonance ($\Delta < 0$) and positive or blue detuning for the case where the laser frequency is higher than the cavity resonance ($\Delta > 0$).³ The steady state solution to Eq. (2.5) is obtained by assuming a constant input mode amplitude $s_{in}(t)$ and setting $da(t)/dt$ to zero, resulting in a mean mode amplitude of:

$$\bar{a} = \frac{\sqrt{\kappa_{ex}}s_{in}}{-i\Delta + \kappa/2}. \quad (2.6)$$

2.1.2 Optomechanical interaction

With the terminology in place, we can turn our attention to the optomechanical interaction itself. In particular, we will show how the coupling between the mechanical motion and the cavity field modifies the response of both the harmonic oscillator (Eq. (2.2)) and the mode amplitude (Eq. (2.6)). The parametric coupling of the mechanical motion to the cavity mode modulates the cavity resonance frequency:

$$\omega_{cav}(x) = \omega_{cav} + x\partial\omega_{cav}/\partial x \quad (2.7)$$

where we have assumed the mechanical motion to be small, such that this linear approximation holds. The expression can be simplified by introducing the optical frequency per displacement as $G = -\partial\omega_{cav}/\partial x$. The typical convention is to define G in such a way that for $x > 0$ the cavity length increases, leading to a decrease in ω_{cav} , hence the minus sign. For a Fabry-Perot cavity as depicted in Fig. 2.1, $G = \omega_{cav}/L$ with L the cavity length. Due to the displacement of the mirror, the cavity resonance frequency changes as $Gx(t)$. Therefore the optomechanical equation for the cavity mode is:

$$\frac{da(t)}{dt} = \left[i(\Delta + Gx(t)) - \frac{\kappa}{2} \right] a(t) + \sqrt{\kappa_{ex}}s_{in}(t). \quad (2.8)$$

The radiation pressure arises from the momentum transfer when a photon reflects off the moving mirror. The radiation pressure is therefore proportional to the number of circulating photons $|a(t)|^2$ and to twice the photon momentum $\hbar k$, with $k = \omega_{cav}/c$ the wave vector. Finally, the photon round-trip time, $c/2L$ with c the

³A small warning: In literature the definition of detuning can vary from article to article. In this thesis terminology and definitions are chosen to be consistent with the work of Aspelmeyer et al. [16]

speed of light, needs to be taken into account. The radiation pressure force is therefore:

$$\begin{aligned} F_{rad} &= \frac{\Delta p}{\Delta t} \\ &= |a(t)|^2 \frac{c}{2L} 2\hbar k = \hbar G |a(t)|^2 \end{aligned} \quad (2.9)$$

where $G = \omega_{cav}/L$ is used to simplify the expression. The equation of motion of the harmonic oscillator becomes:

$$\frac{d^2 x(t)}{dt^2} = -\Gamma_m \frac{dx(t)}{dt} - \Omega_m^2 x(t) + \frac{\hbar G}{m} |a(t)|^2 + \frac{F_{ex}}{m}. \quad (2.10)$$

Equations (2.8) and (2.10) form the theoretical basis of the work presented in this thesis. These coupled non-linear equations are difficult to solve. However, with appropriate assumptions, analytic solutions can still be found. For example, the motion of the harmonic oscillator can be treated as a small perturbation around some mean displacement: $x(t) = \bar{x} + \delta x(t)$. Similarly, the effect of this motion on the cavity field can be treated as a perturbation: $a(t) = \bar{a} + \delta a(t)$. Substituting these assumptions in Eqs. (2.8) and (2.10) yields:

$$\frac{d\delta a(t)}{dt} = (i[\Delta + G(\bar{x} + \delta x(t))]) - \frac{\kappa}{2})(\bar{a} + \delta a(t)) + \sqrt{\kappa_{ex}} s_{in} \quad (2.11)$$

$$\frac{d^2 \delta x(t)}{dt^2} = -\Gamma_m \frac{d\delta x(t)}{dt} - \Omega_m^2 (\bar{x} + \delta x(t)) + \frac{\hbar G}{m} [(\bar{a} + \delta a(t))(\bar{a}^* + \delta a^*(t))] + \frac{F_{ex}}{m} \quad (2.12)$$

As with the uncoupled case, a steady state solution can be found by setting $\delta a(t) = 0$ and $\delta x(t) = 0$:

$$\bar{a} = \frac{\sqrt{\kappa_{ex}} s_{in}}{i(\Delta + G\bar{x}) - \kappa/2} \quad (2.13)$$

$$\bar{x} = \frac{\hbar G}{m\Omega_m^2} |\bar{a}|^2. \quad (2.14)$$

Already the steady-state solution shows an interesting effect: the mean photon number in the cavity depends on the mean displacement. However, the mean photon number also causes a static radiation pressure force on the mirror, thus changing the cavity resonance frequency. This in turn influences the mean photon number. Solving Eqs. (2.13) and (2.14) yields a cubic expression for \bar{a} with stable and unstable solutions [25].

We can also solve for $\delta a(t)$ and $\delta x(t)$. Using Eqs. (2.13) and (2.14), dropping second-order terms and introducing $\tilde{\Delta} = \Delta + G\bar{x}$ one obtains:⁴

$$\frac{d\delta a(t)}{dt} = \left[i\tilde{\Delta} - \frac{\kappa}{2} \right] \delta a(t) + iG\bar{a}\delta x(t) \quad (2.15)$$

⁴Note that we have also used $\bar{a} = \bar{a}^*$. This is valid since the phase of \bar{a} , which follows from the phase of the incoming beam, can always be set to zero.

$$\frac{d^2\delta x(t)}{dt^2} = -\Gamma_m \frac{d\delta x(t)}{dt} - \Omega_m^2 \delta x(t) + \frac{\hbar G \bar{a}}{m} [\delta a(t) + \delta a^*(t)] + \frac{F_{ex}}{m}. \quad (2.16)$$

As for the uncoupled equations, this is best solved by applying the Fourier transform. Besides taking the Fourier transform of the equations above, it is convenient to also write down the Fourier transform of the complex conjugate of Eq. (2.15) to obtain the following three equations:⁵

$$-i\omega\delta a(\omega) = (i\tilde{\Delta} - \frac{\kappa}{2})\delta a(\omega) + iG\bar{a}\delta x(\omega) \quad (2.17)$$

$$-i\omega\delta a^*(\omega) = (-i\tilde{\Delta} - \frac{\kappa}{2})\delta a^*(\omega) - iG\bar{a}\delta x(\omega) \quad (2.18)$$

$$-\omega^2\delta x(\omega) = +i\omega\Gamma_m\delta x(\omega) - \Omega_m^2\delta x(\omega) + \frac{\hbar G \bar{a}}{m} [\delta a(\omega) + \delta a^*(\omega)] + \frac{F_{ex}(\omega)}{m}. \quad (2.19)$$

Solving Eqs. (2.17) - (2.18) gives:

$$\delta a(\omega) = \frac{iG\bar{a}\delta x(\omega)}{\kappa/2 - i(\tilde{\Delta} + \omega)} \quad (2.20)$$

$$\delta a^*(\omega) = \frac{-iG\bar{a}\delta x(\omega)}{\kappa/2 + i(\tilde{\Delta} - \omega)} \quad (2.21)$$

which can readily be used to derive an expression for the radiation pressure force

$$\begin{aligned} \delta F_{rad}(\omega) &= \hbar G \bar{a} (\delta a(\omega) + \delta a^*(\omega)) \\ &= -\hbar G^2 \bar{a}^2 \left(\frac{\tilde{\Delta} + \omega}{\kappa^2/4 + (\tilde{\Delta} + \omega)^2} + \frac{\tilde{\Delta} - \omega}{\kappa^2/4 + (\tilde{\Delta} - \omega)^2} \right) \delta x(\omega) \\ &+ i\hbar G^2 \bar{a}^2 \left(\frac{\kappa/2}{\kappa^2/4 + (\tilde{\Delta} + \omega)^2} - \frac{\kappa/2}{\kappa^2/4 + (\tilde{\Delta} - \omega)^2} \right) \delta x(\omega). \end{aligned} \quad (2.22)$$

In the Fourier domain, the radiation pressure has both a real and imaginary component. The real component results in an optical spring effect, while the imaginary component generates an optical damping force. This can be shown explicitly by inserting the result of Eq. (2.22) back in Eq. (2.19). As for the uncoupled case, the solution can be written as $x(\omega) = \chi_{eff}(\omega)F_{ex}(\omega)$ with $\chi_{eff}(\omega)$ the effective susceptibility:

$$\chi_{eff}(\omega) = \left[m(\Omega_m^2 + \frac{k_{opt}(\omega)}{m} - \omega^2) \right] - im\omega [\Gamma_m + \Gamma_{opt}(\omega)]^{-1}. \quad (2.23)$$

in which the optical spring constant $k_{opt}(\omega)$ and optical damping $\Gamma_{opt}(\omega)$ are defined as:

$$k_{opt}(\omega) = \frac{\hbar G^2 \bar{a}^2}{m} \left(\frac{\tilde{\Delta} + \omega}{\kappa^2/4 + (\tilde{\Delta} + \omega)^2} + \frac{\tilde{\Delta} - \omega}{\kappa^2/4 + (\tilde{\Delta} - \omega)^2} \right). \quad (2.24)$$

⁵Again we have used the freedom to set the phase in such a way that δx is real.

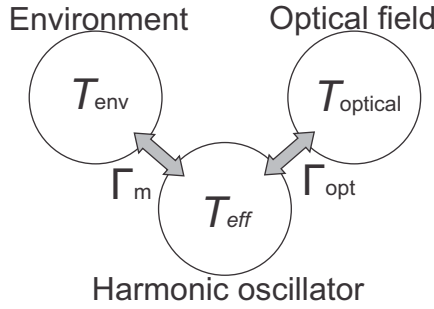


Figure 2.2: The harmonic oscillator is coupled to the environment with coupling rate Γ_m and to the optical field with coupling rate Γ_{opt} .

$$\Gamma_{opt}(\omega) = \frac{\hbar G^2 \bar{a}^2}{m\omega} \left(\frac{\kappa/2}{\kappa^2/4 + (\tilde{\Delta} + \omega)^2} - \frac{\kappa/2}{\kappa^2/4 + (\tilde{\Delta} - \omega)^2} \right) \quad (2.25)$$

Finally, when the optical spring effect and optical damping are small, the effective resonance frequency and effective damping rate are given by:⁶

$$\Omega_{eff} = \Omega_m + g^2 \left(\frac{\Delta + \Omega_m}{\kappa^2/4 + (\Delta + \Omega_m)^2} + \frac{\Delta - \Omega_m}{\kappa^2/4 + (\Delta - \Omega_m)^2} \right) \quad (2.26)$$

$$\Gamma_{eff} = \Gamma_m + g^2 \left(\frac{\kappa}{\kappa^2/4 + (\Delta + \Omega_m)^2} - \frac{\kappa}{\kappa^2/4 + (\Delta - \Omega_m)^2} \right) \quad (2.27)$$

where the multi-photon coupling rate g , defined as $g^2 = \frac{\hbar G^2 \bar{a}^2}{2m\Omega_m}$ is introduced, and the static radiation pressure is assumed to be small such that $\tilde{\Delta} \approx \Delta$.

Comparing the uncoupled case with the case including optomechanical interaction, one sees that the motion of the harmonic oscillator creates a radiation pressure force which, when acting back on the mirror, modifies the resonance frequency and damping rate. The magnitude of this effect, not surprisingly, varies with input laser power. More importantly, however, for specific laser detunings the radiation pressure causes predominantly an optical spring effect or an optical damping. Furthermore, for positive detunings, anti-damping can occur, leading to a reduction of the effective damping rate and even driving of the mechanical motion. This phenomena is explored in detail in chapter 3.

So far we have only discussed the modifications to the mechanical response. The optical damping however couples the harmonic oscillator to the laser bath. In the next section the consequence, namely optical cooling, will be discussed together with methods to measure this effect.

2.1.3 Optical cooling

When deriving the response for the harmonic oscillator in the presence of an optical field, Γ_m has only been thought of as a damping rate. However, it also couples the

⁶The Taylor approximation $\Omega_{eff} = \sqrt{\Omega_m^2 + \frac{k_{opt}(\omega)}{m}} \approx \Omega_m + k_{opt}/2m\Omega_m$ is used.

oscillator to the environment which is at some temperature T_{env} . The fluctuation-dissipation theorem describes the thermodynamics of such coupled systems [26, 27, 28]. Coupling to a thermal environment (or thermal bath) generates a force which acts on the oscillator in such a way that, when in equilibrium, the variance of the displacement is proportional to the environmental temperature T_{env} :

$$\left. \begin{aligned} E &= \frac{1}{2} m \Omega_m^2 \langle x(t)^2 \rangle \\ E &= \frac{1}{2} k_b T_{env} \end{aligned} \right\} \quad \langle x(t)^2 \rangle = \frac{k_b T_{env}}{m \Omega_m^2} \quad (2.28)$$

which is the equipartition theorem. In other words: the displacement of a harmonic oscillator coupled to a thermal bath is such that the mode temperature is equal to the bath temperature. When now the coupling with the cavity field is included, we have the situation as depicted in Fig. 2.2. The harmonic oscillator is coupled with coupling rate Γ_m to a bath at temperature T_{env} , and coupled with coupling rate Γ_{opt} to the optical field. By assuming thermal equilibrium, the effective temperature of the harmonic oscillator can therefore be written as:

$$T_{eff} = \frac{T_{env} \Gamma_m + T_{optical} \Gamma_{opt}}{\Gamma_{opt} + \Gamma_m}. \quad (2.29)$$

Although it might be strange to label a coherent optical field with a temperature, from a noise perspective, a coherent optical field has an effective temperature of zero [29]. With this, Eq. 2.29 reduces to

$$T_{eff} = T_{env} \frac{\Gamma_m}{\Gamma_{opt} + \Gamma_m}. \quad (2.30)$$

Note that at sufficiently low effective temperatures, this equation no longer holds and one has to take the photon shot noise into account as well. For the results presented in this thesis, the effective temperature is still high enough for Eq. (2.30) to be valid. With the full quantum theory, one can also show that optical cooling to the quantum mechanical ground state is possible when $\kappa \ll \Omega_m$ ⁷. This limit is often referred to as the side-band resolved limit. Most of the experiments presented in this thesis operate in the side-band resolved limit.

One can obtain the effective mode temperature by recording $x(t)$, determining the variance and using the equipartition theorem. A more elegant way would be to record $x(t)$ and take the Fourier transform to obtain the power spectral density (PSD) S_{xx} , because the fluctuation-dissipation theorem relates S_{xx} to the effective temperature by:

$$S_{xx}(\omega) = 2 \frac{k_b T_{eff}}{\omega} \text{Im} \chi_{eff}(\omega). \quad (2.31)$$

⁷The requirement of $\kappa \ll \Omega_m$ only applies when optical side-band cooling is used as the cooling method. Active feedback cooling [30] and so called "dissipative" optomechanical coupling [31] do not require to be side-band resolved. So far, however, only side-band cooling has successfully been used to reach the quantum mechanical ground-state.

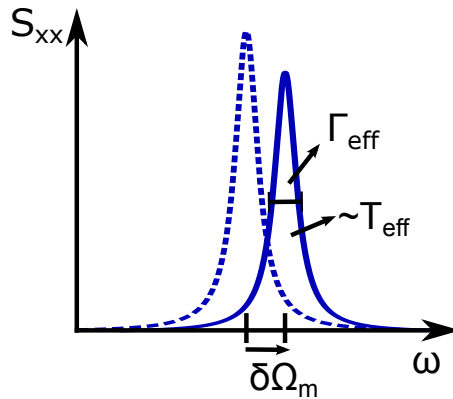


Figure 2.3: A measurement of the power spectral density of the mechanical motion gives directly the parameters of interest, namely the effective temperature, mechanical linewidth and resonance frequency.

Integrating S_{xx} over all frequencies, results in the following:

$$\begin{aligned} \int_{-\infty}^{\infty} S_{xx}(\omega) \frac{d\omega}{2\pi} &= \frac{k_b T_{eff}}{m\Omega_m^2} \\ &= \langle x(t)^2 \rangle \end{aligned} \quad (2.32)$$

where Eq. (10.4) was used in the last line.

Not only does integrating the mechanical PSD directly give the effective temperature, but the Lorentzian resonance also gives the effective linewidth and frequency shift, as is shown in Fig. 2.3. Therefore, the full optomechanical interaction is characterized by measuring the PSD of the mechanical motion. But how to measure $x(t)$ to obtain the mechanical PSD?

We have already seen that due to the movement of the mirror, the cavity resonance frequency changes according to $Gx(t)$. Therefore, any change in cavity resonance frequency is directly proportional to the displacement. There are two methods for measuring changes in the cavity resonance frequency. In Fig. 2.4(a) the side-of-fringe method is shown. By placing a laser to the side of the cavity resonance, a small change in cavity length leads to a change in mode amplitude which can be measured by monitoring the transmitted intensity. The resulting signal can also be used to keep a laser locked to a certain frequency with respect to the cavity resonance (side-of-fringe lock).

The other method is a phase sensitive detection method, as is shown in Fig. 2.4(b). This method is actually preferred, because the read-out can take place exactly at the cavity resonance, which is not possible with the side-of-fringe method. Since there is no optomechanical effect at zero detuning, the motion of the resonator can be obtained without influencing the system.⁸ Finally, the phase sensitive method is, to first order, not sensitive to laser intensity fluctuations.

⁸Here we consider only the classical case. In the quantum description, the photon shot noise sets

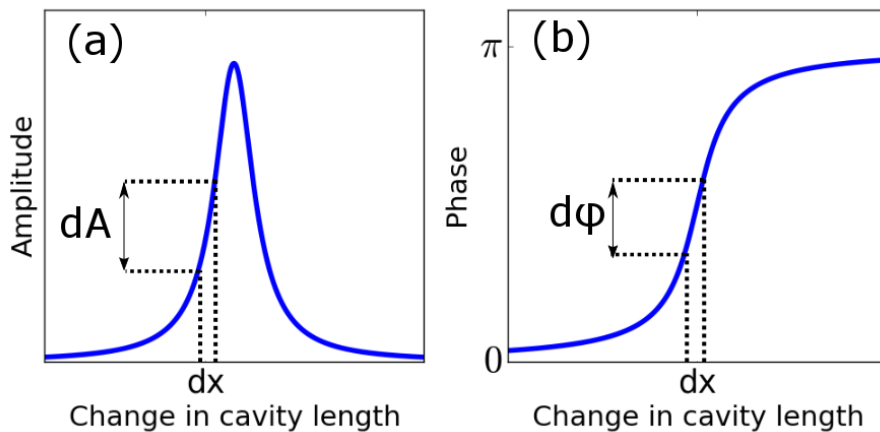


Figure 2.4: Amplitude (a) and phase response (b) of an optical resonance. The mirror displacement can be measured in two ways: side-of-fringe method as shown in (a) and via a phase sensitive detection method shown in (b).

2.2 Experimentals

With the basics of the optomechanical interaction discussed, such as optical cooling and displacement transduction, we turn to the experimental aspects of this thesis. First, the “optical bench” containing the cavity and trampoline resonator is briefly described, before continuing with an overview of the trampoline resonator. Finally, we introduce the core of the experimental methods used in this thesis, including the laser scheme.

2.2.1 Optical bench

The optical bench, designed by H. van der Meer, has a compact footprint such that integration in a cryogenic system is possible. The bench is made from brass and constructed around a 5 cm long optical cavity. A length of 5 cm was chosen as a compromise between optical path length and mirror quality. A larger cavity length would benefit the superposition schemes mentioned in the introductory chapter. However, a longer cavity requires larger mirrors, which are more difficult to fabricate.

In Fig. 2.5(a) a schematic overview of the bench is shown. The light enters the system via an optical fiber (Nufern 1060-XP) after which it is collimated using an aspheric lens (Edmund Optics 15 mm diameter 22.5 mm EFL). Via a periscope consisting of two adjustable mirrors the light passes through a mode-matching lens (Thorlabs Best Form LBF254-050-C) and enters the cavity through a 1/2 inch super-polished mirror with a 5 cm radius of curvature (Advanced Thin Films and Laser Optik). After passing through the trampoline resonator, the transmitted signal is col-

a lower limit to the measurement precision, leading to the formulation of the standard quantum limit (SQL).

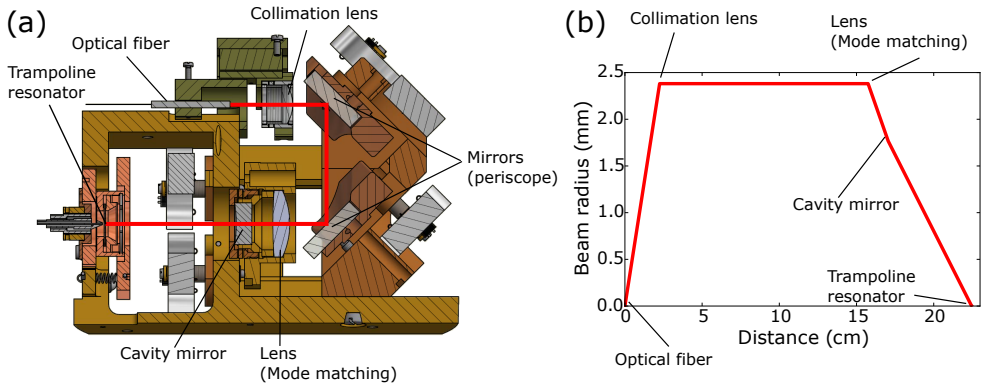


Figure 2.5: (a) Schematic overview of the optical bench with the key components indicated. (b) Beam radius as function of propagation distance along the optical path represented by the red line in (a) calculated using Gaussian beam optics.

lected via a photo-detector (Hamamatsu G10899-005K, connected to a Femto DHP-100 amplifier) placed behind the cavity. The reflected light is collected by the fiber that also brings the light to the set-up. The optical components are chosen to ensure optimal mode-matching to the fundamental cavity mode by using Gaussian beam theory and ray matrices [32]. The resulting beam radius as function of propagation distance is shown in Fig. 2.5(b).

The cavity alignment is quite sensitive, requiring sub-micron adjustments. Therefore, the collimation lens is placed on an Attocube translation stage and both the large cavity mirror and periscope mirrors are adjustable by Piezoknobs from JPE. These cryogenic compatible actuators also ensure that the alignment is adjustable to compensate for the inevitable contraction that occurs when cooling down the set-up.

The entire set-up is placed in a vacuum chamber with passive vibration isolation involving a damped mass-spring system to decouple the set-up from any environmental disturbances. For the cryogenic experiments in a cryogen-free cryostat, a more elaborate vibration isolation stage is developed, which we will discuss in more detail in chapter 10. All experiments discussed in this thesis are performed in medium to high vacuum (typically $<1 \times 10^{-3}$ mbar) to eliminate the effect of gas damping on the mechanical properties of the trampoline resonator.

2.2.2 Trampoline resonators

The trampoline resonators used throughout this thesis are fabricated by colleagues at UCSB (B. Pepper, M. Weaver and F. Luna). Here we will highlight the important fabrication steps of these trampoline resonators, the precise details can be found elsewhere [33, 34].

High stress silicon nitride (typically 850 MPa) is deposited on a super-polished silicon wafer. Next, a distributed Bragg reflector (DBR) of alternating layers of Ta_2O_5 and SiO_2 is deposited by Advanced Thin Films and in later stages of this work by Laser Optik. A DBR mirror is the only way to achieve the reflectivity ($R > 0.99997$)

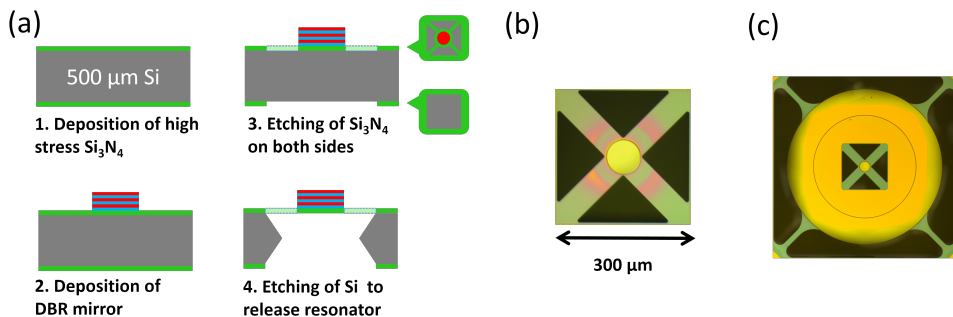


Figure 2.6: (a) The four main fabrication steps to make a trampoline resonator. (b) Optical microscope image of the trampoline resonator. (c) Optical microscope image of a nested trampoline resonator.

we need to create a high quality cavity. Using lithography and etching, the silicon nitride is patterned to achieve the desired resonator design. Finally the silicon is etched away to release the resonator. These steps are schematically indicated in Fig. 2.6(a) together with an optical microscope image of the finished resonator in Fig. 2.6(b). Typically the mirror has a diameter between 60 and $130\ \mu\text{m}$, while the frequency of the resonator lies between 150 and $350\ \text{kHz}$, with a mode-mass between 100 and $500\ \text{ng}$.

The design with four arms, as shown in Fig. 2.6(b), ensures that higher order mechanical modes have a much higher frequencies than the fundamental mechanical mode and couple poorly to the cavity field. The only mechanical mode that is therefore considered in this thesis is the fundamental out-of-plane mode of the trampoline resonator.

Besides a single resonator, also a nested resonator [35], as shown in Fig. 2.6(c), was used in parts of this thesis. In chapter 7, we will come back to the necessity for this modified design. The fabrication process of the nested resonator is essentially the same as depicted in Fig. 2.6(a).

2.2.3 Aligning the optical bench

The alignment of the optical bench shown in Fig. 2.5(a) has two parts: the coupling to the cavity mode, and the alignment of the cavity itself. The coupling to the correct cavity mode is achieved by adjusting the periscope, together with the collimation lens. If the periscope is set incorrectly, higher order Hermite-Gaussian modes become visible as is shown in Fig. 2.7.

Because of the small mirror on the trampoline resonator, the cavity operates as a near-hemispherical resonator [22] with the beam waist close to the small mirror. As a consequence, the size of the cavity mode at the entrance mirror is quite large. The influence of cavity length on the beam radius⁹ for both the large entrance mirror and the small mirror is shown in Fig. 2.8(a) and (b). When the cavity approaches

⁹The beam radius is defined as the radius at which the intensity drops by $1/e^2$

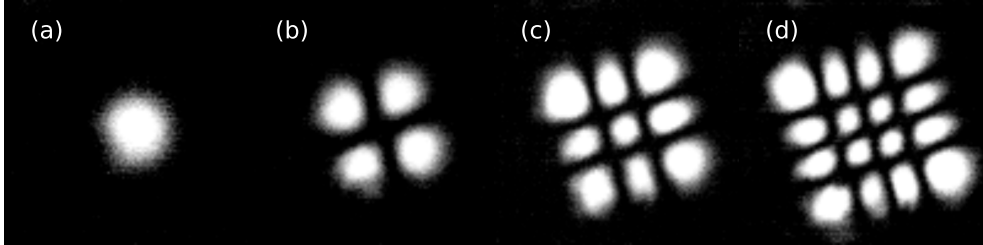


Figure 2.7: Different Hermite-Gaussian modes exist in the optical cavity, depending on the settings of the periscope. (a) The fundamental mode (TEM_{00}) considered here in this thesis. Examples of other possible modes are: (b) TEM_{11} mode (c) TEM_{22} and (d) TEM_{33} mode.

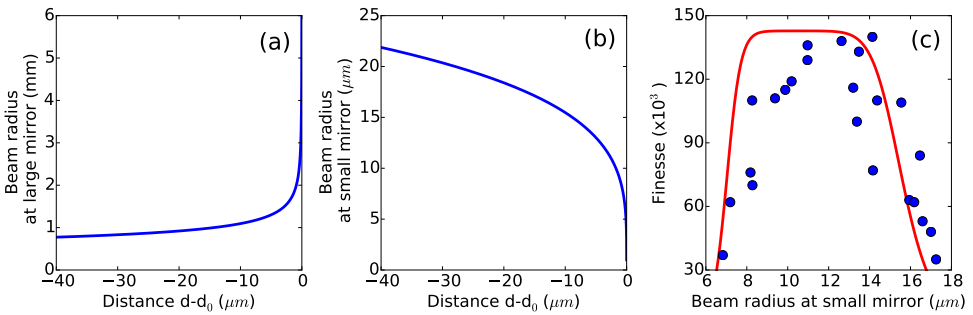


Figure 2.8: Beam radius as function of distance for (a) the mode at the large entrance mirror and (b) the mode at the small mirror of the trampoline resonator. (c) The finesse measured as function of the size of the mode at the small mirror. The red line is the expected finesse based Eqs. (2.33) and (2.34). For this measurement the diameter of the small mirror is 70 micrometer.

$d_0 = 5$ cm, the beam size at the large mirror increases rapidly, while the beam size at the small mirror decreases rapidly. The length can be set such that the beam size is small enough to fit on the trampoline resonator and not too big to clip on the large entrance mirror. These clipping losses L , both at the large and small mirror, can be modeled using the overlap between the size of the mirror and the size of the mode [36]:

$$L = 1 - \exp(-2r_{\text{mirror}}^2/w^2) \quad (2.33)$$

in which r_{mirror} is the radius of the mirror, and w the beam radius at the mirror. Together with the reflectance defined as $R = 1 - T - L$ where T is the mirror transmittance, the finesse for a high quality cavity can be written as:¹⁰

$$\mathcal{F} = \frac{\pi(R_1 R_2)^{1/4}}{1 - (R_1 R_2)^{1/2}}. \quad (2.34)$$

The effect of cavity length on the finesse has been investigated experimentally by measuring the finesse via an optical ring-down together with the beam size at the small mirror. The size of the beam at the entrance mirror can be calculated using the beam size at the small mirror. With the total clipping losses calculated via Eq. (2.33), a prediction for the finesse using Eq. (2.34) is obtained. The results are shown in Fig. 2.8(c) for a trampoline resonator with mirror radius of 35 micrometer. When the beam radius at the small mirror is large, clipping losses at the small mirror reduce the finesse. For small beam sizes, obtained when the cavity length is close to d_0 (see Fig. 2.8 (b)), the dominant loss source is clipping of the beam at the large mirror. In between a flat region exists where the finesse is limited only by the coating of the mirrors.

Adjusting the cavity length carefully therefore results in the optimal finesse. Unfortunately, due to size constraints of the optical bench, the cavity length can only be adjusted by moving the entrance mirror, resulting in a misalignment of the periscope. Only via a non-trivial iterative process is the optimal alignment achieved.

2.2.4 Performing an optomechanical experiment

In section 2.1.3 we have shown how the mechanical motion can optically be reduced by using a laser with the correct detuning Δ . The laser detuning is indicated with respect to the cavity resonance. The cavity resonance frequency and laser frequency might vary over time.¹¹ These variations are eliminated by actively keeping track of the cavity resonance. For this the Pound-Drever-Hall (PDH) method is used [37, 38]. This is a phase sensitive detection method to keep an oscillator (laser), locked to a resonator (cavity). There are other phase sensitive methods such as homodyne detection, in which an additional laser beam serves as a phase reference. This, however,

¹⁰Finesse is related to optical linewidth via $\mathcal{F} = \frac{FSR}{\kappa}$, where FSR is the free spectral range of the cavity. The cavity used in this work has an FSR of 3 GHz.

¹¹In practice two types of variations play a role: fast, small scale variations caused by vibrations of the set-up from external influences and slow drift in environmental temperature. To highlight the sensitivity of the set-up: when at room temperature, if the temperature changes by 1 mK, the cavity resonance frequency changes by 5 MHz, many times the optical linewidth (~ 100 kHz) of the cavity.

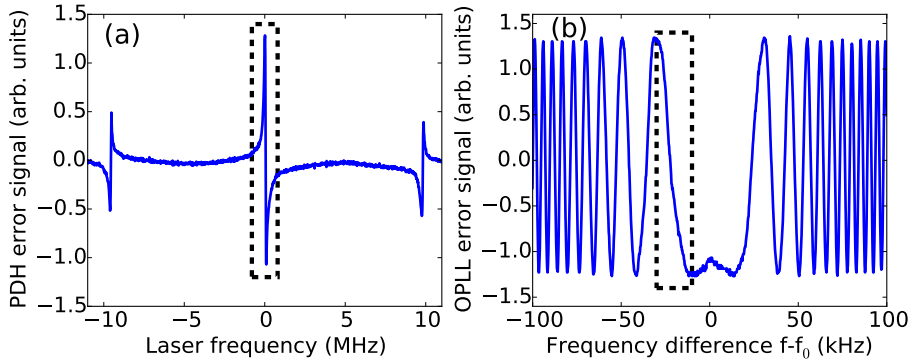


Figure 2.9: (a) PDH open-loop error signal generated by scanning the laser across a cavity resonance. (b) Open-loop error signal of the optical phase-locked loop generated by scanning the frequency of one laser while the other laser is free-running. The x-axis displays the difference frequency $f-f_0$ between the two lasers where $f_0=3$ GHz. The dashed box in both figures indicate the linear region used for the feedback.

requires that the beat signal between transmitted light and the additional laser can be measured, which is not possible for our experimental set-up.

In the case of PDH, one carrier and two sidebands created via phase modulation, are sent to the cavity. Any cavity length change will directly cause a change in phase of the resonant carrier (see Fig. 2.4(b)), while the off-resonant side-bands are directly reflected. These side-bands serve as a phase reference when measuring the interference between carrier and side-bands. In this way, any cavity length changes (or laser frequency changes) can be measured, including the motion of the trampoline resonator.

The resulting PDH signal can be used as the error signal for a PID controller to keep the laser on resonance with the cavity. An example of the open-loop error signal is shown in Fig. 2.9(a). The PDH method, therefore, serves two purposes in our experiment: the error signal provides a reference and is used for the read-out of the mechanical motion. This is only possible when the frequency of the trampoline resonator is much higher than the feedback bandwidth. If the mechanical resonance frequency falls within the feedback bandwidth, the motion of the resonator will be visible in the output of the PID controller.

In addition to a read-out laser, another laser is used to generate the optical force. Technically, the same laser can be used to generate the optical force as well, but to avoid any unwanted interference it is easier to use a second laser (when available). This second laser operates one free spectral range (FSR) of the cavity (~ 3 GHz) away from the first laser, again to avoid unwanted interference. Any drift in laser frequency is resolved by having the second laser follow the first laser via an optical phase-locked loop (OPPL), which works exactly like a normal phase-locked loop. The beat signal of the two lasers is mixed with an electrical local oscillator operating

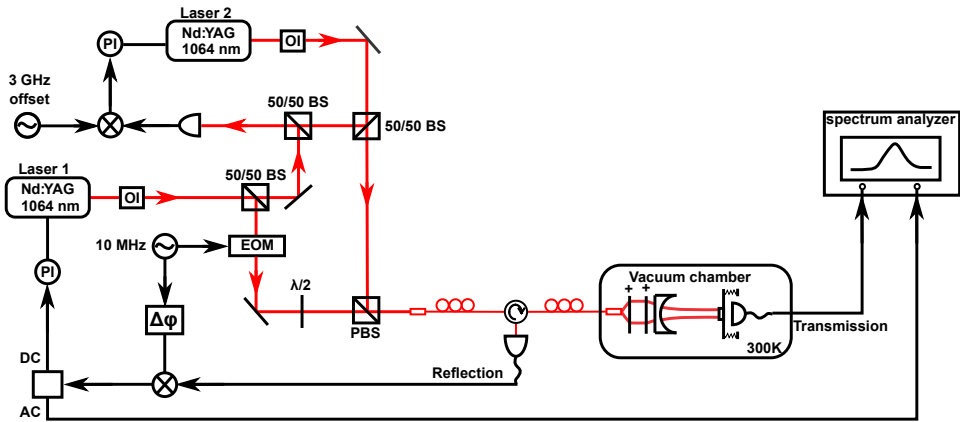


Figure 2.10: Simplified schematic of the optical set-up. The components displayed are: LO: local oscillator, BS: beam splitter, PBS: polarizing beam splitter, EOM: electro-optical modulator, OI: optical isolator and PI: proportional-integral feedback controller.

at approximately the FSR of 3 GHz.¹² The output of the mixer is shown in Fig. 2.9(b). The dashed box indicates the linear region which can be used as an error signal for a feedback loop to keep the phase of the beat signal constant with respect to the local oscillator. If we would like to change the detuning of the second laser, we change the local oscillator frequency. The frequency of the second laser is then, via a PID controller, adjusted to keep the phase of the beat the same as the phase of the local oscillator.

After alignment of the optical bench and placing the whole set-up either in a vacuum chamber or a cryostat, an optomechanical experiment begins by locking the first laser via the PDH method to a cavity resonance to provide both the reference and the read-out of the mechanical motion. Next, the second laser is locked to the first laser via the OPPL. Finally, the detuning is adjusted to see, for example, optical cooling by monitoring the mechanical power spectral density.

In Fig. 2.10 a simplified schematic is shown of the optical set-up and we will give a quick run through of the set-up and components. Laser 1 (Coherent Mephisto S) is sent through an electro-optical modulator (EOM) to generate the two sidebands needed for the PDH scheme. The light reflected from the cavity is, via a fiber circulator, picked up with a photodiode. The electrical signal is mixed with the local oscillator (LO) at 10 MHz that also drives the EOM. The low-frequency part is routed to a PI controller (VU lock-box with ~ 30 kHz bandwidth) to lock the frequency of laser 1 to a cavity resonance. The high-frequency part is sent to a spectrum analyzer (Zurich Instruments HF2LI) to record the mechanical thermal noise spectrum S_{xx} of the mechanical resonator. To lock laser 2 (Coherent Mephisto) with a variable frequency difference to laser 1 via an OPLL, the beat signal of laser 1 and 2 is continuously monitored using a fast PIN diode (EOT ET-3500F). This signal is mixed with

¹²Alternatively, a frequency divider can be used when an appropriate frequency generator is not available. Using a divider will, however, reduce the phase stability of the OPLL.

a local oscillator around 3 GHz (Rohde and Schwarz SMA100A) to provide the error signal for the OPLL, which is directed to a fast PI-controller (VU lock-box with ~ 30 kHz bandwidth). By adjusting the frequency of the OPLL LO, laser 2 can be set to a specific cavity detuning.

The frequency tunable range of the lasers via the piezos is limited to approximately 10 MHz. However, both lasers are also temperature tunable over a broader frequency range (~ 1 GHz), although with < 1 Hz bandwidth. Therefore a slow laser frequency feedback loop for each laser is implemented based on temperature control that enables measurements for many hours with a fully automated measurement protocol.

Experimental exploration of the optomechanical attractor diagram and its dynamics

In this chapter we investigate the optomechanical interaction in more detail. In particular we explain how the motion of the mirror leads to phase modulation of the cavity field, creating optical side-bands. These side-bands interact back again with the mirror, leading to intricate dynamics.

We demonstrate this experimentally by exploring the attractor diagram of an optomechanical system where the optical forces compensate for the mechanical losses. In this case stable self-induced oscillations occur but only for specific mirror amplitudes and laser detunings. We demonstrate that we can amplify the mechanical mode to an amplitude 500 times larger than the thermal amplitude at 300 K. The lack of unstable or chaotic motion allows us to manipulate our system into a nontrivial steady state and explore the dynamics of self-induced oscillations in great detail.

The work presented in this chapter is based on: F.M. Buters, H.J. Eerkens, K. Heeck, M.J. Weaver, B. Pepper, S. de man and D. Bouwmeester, "Experimental exploration of the optomechanical attractor diagram and its dynamics", *Phys. Rev. A* 92, 013811 (2015) and F.M. Buters, H.J. Eerkens, K. Heeck, M.J. Weaver, B. Pepper, P. Sonin, S. de man and D. Bouwmeester, "Large parametric amplification in an optomechanical system", *Physica Scripta* 2015.T165 (2015)

3.1 Introduction

Laser or microwave cooling of a mechanical degree of freedom has led several groups to come close to or even reach the quantum-mechanical ground state of a macroscopic harmonic oscillator [39, 40, 41]. This has opened up many new research avenues to investigate the foundations of quantum mechanics [42], novel decoherence mechanisms [9, 14, 43], and strong photon-phonon coupling [44, 45, 46]. Besides cooling, heating of the mechanical degree of freedom is possible, leading to parametric instabilities, self-induced oscillations, and even chaos. Braginsky et al. have derived the condition for achieving parametric instability in a Fabry-Perot interferometer such as LIGO [47], which is still a topic of interest [48]. The theoretical framework has been expanded by Marquardt et al., with the introduction of an attractor diagram and an expression for the optomechanical gain [49, 50]. From an experimental point of view Carmon et al. showed how self-induced oscillations of the mechanical mode are imprinted on the cavity output field [51, 52]. Finally the transition from self-induced oscillation to chaos has been investigated with some interesting prospects for observing the quantum to classical transition [53, 54].

The dynamics of self-induced oscillations are best understood using an attractor diagram. So far only a small part of this diagram has been explored experimentally by Metzger et al. with the photothermal effect as the driving force [55]. Little effort has been made to investigate the attractor diagram experimentally using radiation pressure force. It has therefore been to date an open problem to explore the full attractor diagram experimentally [16]. One reason for this is that a transition from self-induced oscillations to chaotic mirror motion can occur due to second-order effects, such as absorption-induced heating of the optical components [51, 53]. This restricts the exploration of the attractor diagram to small values of the mirror amplitude.

Here we demonstrate an optomechanical setup, consisting of a Fabry-Perot cavity with a trampoline resonator, that does not suffer from optical absorption in the mirrors. Not only does this enable us to explore a large part of the attractor diagram in a controlled fashion, but also we find surprisingly rich dynamics and non-trivial steady states of our optomechanical system.

3.2 Theoretical model

Our optomechanical system is described by two coupled equations of motion:

$$\frac{da(t)}{dt} = \frac{-\kappa}{2}a(t) + i(\Delta + Gx(t))a(t) + \sqrt{\kappa_{ex}}s_{in} \quad (3.1)$$

$$\frac{d^2x(t)}{dt^2} = -\Omega_m^2x(t) - \Gamma_m \frac{dx(t)}{dt} + \frac{\hbar G}{m} |a(t)|^2, \quad (3.2)$$

in which a is the cavity field and x is the mirror displacement. The parameters in Eqs. (3.1) and (3.2) are defined as follows: s_{in} is the laser field, κ is the overall cavity decay rate, κ_{ex} is the cavity entrance loss rate, $\Delta = \omega_L - \omega_{cav}$ is the laser detuning defined as the difference between cavity and laser frequencies, the optical frequency shift per displacement $G = \omega_{cav}/L$, with L being the length of the cavity, Ω_m as

the fundamental mode frequency of the mechanical oscillator, Γ_m as the mechanical damping rate and m as the mode mass of the harmonic oscillator. Thermal and mechanical noise sources have been neglected; an important assumption that will be justified for our optomechanical system by the results below.

The optomechanical attractor diagram displays the optomechanical gain ζ_{opt} , the ratio of the radiative force P_{rad} and frictional losses P_{fric} , as a function of laser detuning Δ and mirror amplitude A . From Eqs. (3.1) and (3.2) an expression for ζ_{opt} can be derived [49],

$$\zeta_{opt}(\Delta, A) = \frac{P_{rad}}{P_{fric}} = -\frac{1}{\Gamma_m} \frac{2\hbar G \kappa_{ex} s_{in}^2}{m\Omega_m A} \text{Im} \left(\sum_n a_{n+1}^* a_n \right) \quad (3.3)$$

with

$$a_n = \frac{J_n(-GA/\Omega_m)}{\kappa/2 - i\tilde{\Delta} + in\Omega_m}, \quad (3.4)$$

in which α_n is the n th harmonic (or sideband) in the optical field created by the mirror motion, J_n is the Bessel function of the first kind, and $\tilde{\Delta}$ is the effective laser detuning defined as $\tilde{\Delta} = \omega_L - \omega_{cav} + G\bar{x}$, where \bar{x} is the static displacement of the mirror due to the radiation pressure. For most situations, including ours, the static displacement is negligible and $\Delta \approx \tilde{\Delta}$. Stable self-induced oscillations occur when $\zeta_{opt}(\Delta, A) = 1$, whereas amplification (attenuation) of the mechanical mode occurs when $\zeta_{opt}(\Delta, A) > 1$ ($\zeta_{opt}(\Delta, A) < 0$).

To give a better understanding of the phenomena of self-induced oscillations we describe the parametric process in an optomechanical system qualitatively and connect this back to Eqs. (3.1)-(3.4). When the incoming laser field at frequency ω_L interacts with the moving mirror (the term $Gx(t)a(t)$ in Eq.(3.1)), the laser field is phase modulated such that sidebands appear at $\omega = \omega_L \pm n\Omega_m$ with n a positive integer. The number of sidebands that appear depends on the modulation depth $\phi_o = -GA/\Omega_m$. The larger the amplitude, the more sidebands or harmonics of the mechanical frequency Ω_m are imprinted on the cavity field, as is clear from Eq.(3.4) where ϕ_o is the argument of the Bessel function. Note that to take into account the enhancement of the optical field by the presence of a cavity, $J_n(-GA/\Omega_m)$ is scaled for the cavity line shape (see denominator of Eq.(3.4)). If the cavity field, with all the harmonics, interact again with the mirror, only resonant force components contribute to the motion of the mirror (resonant terms of $\frac{\hbar G}{m} |a|^2$). These resonant force components arise by the non-linear mixing of neighboring harmonics a_n at the moving mirror (the term $\sum_n a_{n+1}^* a_n$ in Eq.(3.3)). By taking the imaginary part of this sum, the damping due to the optical field is obtained. Alternatively, by taking the real part the term responsible for the optical spring effect is obtained. By changing the laser frequency detuning Δ or varying the amplitude of the mirror A , the optical damping and thereby also the optomechanical gain ζ_{opt} is either positive (attenuation) or negative (amplification).

One way to map out the attractor diagram $\zeta_{opt}(\Delta, A)$ is to measure the mirror amplitude while varying the laser detuning. Such measurement schemes have already successfully been used for demonstrating optical cooling. With optical cooling, the change in cavity resonance frequency due to the motion of the mirror is usually much

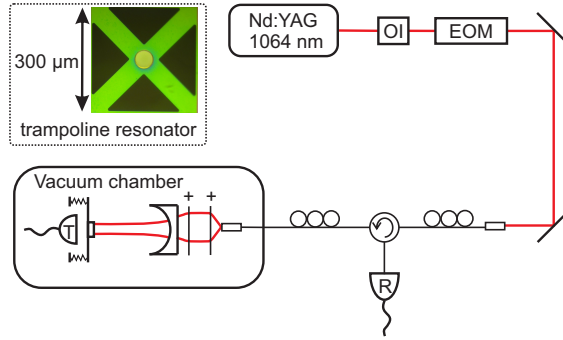


Figure 3.1: Schematic of the set up. A piezo tunable cw Nd:YAG laser is passed through an optical isolator (OI) and a 9.5 MHz electro-optical modulator (EOM) before it enters a fiber circulator that is fed into a vacuum chamber that contains a 5 cm Fabry-Perot cavity. Both the transmitted and the reflected intensities are recorded with photo-detectors. The inset shows an optical image of the trampoline resonator.

smaller than the linewidth of the cavity resonance, i.e., $GA \ll \kappa$. In the optical field only the first sideband is visible, and the magnitude of this sideband is linear with mirror amplitude. For optical excitation, however, the change in cavity resonance frequency can be much larger than the cavity linewidth, i.e., $GA \gg \kappa$, resulting in multiple sidebands present in the optical field. The linear relation between the first sideband and the mirror amplitude no longer holds. Now the mirror amplitude can only be obtained by taking into account all optical sidebands.

3.3 Experimental setup

To map out the attractor diagram we make use of a 5 cm long Fabry-Perot cavity operating around 1064 nm, with a trampoline resonator as one of the end mirrors [33]. By using a multilayer Bragg stack on both cavity mirrors, absorption losses are minimized to about 1 ppm. The system is placed inside a vacuum chamber with a vibration isolation system containing several eddy-current dampers. All measurements are performed at room temperature. A schematic of the set-up is given in Fig. 3.1. We use a piezo tunable cw Nd:YAG laser and control it with a typical scan speed of $\frac{d\omega_L}{dt} = 100 - 400$ MHz/s, which is slow compared to the cavity build up time, i.e. $\frac{d\omega_L}{dt} \ll \kappa/\tau$ with κ as the cavity linewidth and τ as the cavity lifetime. An EOM at 9.5 MHz is used to calibrate the laser detuning. The mechanical properties of the trampoline resonator are characterized by measuring the thermal noise spectrum and the optical properties by performing an optical ring-down measurement [33]. Both transmitted and reflected cavity light are detected using photo-detectors, and the data-acquisition is performed using a digital storage scope. For our system only the fundamental mechanical mode and fundamental optical mode (TEM_{00}) are relevant. The parameters for our system are the following: $\kappa = 175 \times 10^3 \times 2\pi$ rad/s, $\kappa_{ex} = 50 \times 10^3 \times 2\pi$ rad/s, $\Omega_m = 343 \times 10^3 \times 2\pi$ rad/s, $\Gamma_m = 1.7 \times 2\pi$ rad/s at a

pressure of 10^{-6} mbar and $m = 110 \times 10^{-12}$ kg. To achieve a sufficiently large optomechanical gain, the input laser power should also be sufficiently large. A typical laser input power of 50 to 100 μ W is used, corresponding to an intracavity photon number of $2.8 - 5.6 \times 10^8$.

3.4 Results

Figure 3.2(a) shows the optical intensity transmitted by the cavity when the laser is scanned back and forth across the cavity resonance. Several peaks are visible, not only at the cavity resonance $\Delta/\Omega_m = 0$, but also at multiples of Δ/Ω_m . In the appendix of this chapter, the behavior of these peaks is investigated in more detail. The appearance of sidebands can be explained as follows. Suppose the laser frequency is at $\omega_L = \omega_{cav} + \Omega_m$ and the amplitude of the mirror is small such that only the first sideband is created by the moving mirror at frequencies $\omega = \omega_L \pm \Omega_m$. Only the Stokes sideband at $\omega = \omega_{cav}$ is resonant with the cavity and enhanced, whereas the anti-Stokes sideband at $\omega = \omega_{cav} + 2\Omega_m$ is suppressed. So the interaction of the blue detuned laser field with the resonator leads to a resonant field in the cavity. The non-linear interaction of the resonant cavity field plus the incoming laser field with the mirror lead to a resonant driving force. By creating sidebands, the mirror generates its own driving force, which increases the mirror amplitude. The increased mirror amplitude leads to a stronger modulation of the cavity field, and this process repeats until the gain is reduced to $\zeta_{opt} = 1$ (limit cycle behavior). When the laser detuning is slowly increased further, the process repeats whereby the ever increasing mechanical motion allows sideband generation to drive the mirror to larger amplitudes. This process continues until the laser is swept back rapidly to $\Delta/\Omega_m = -30$. At first the laser detuning and mirror amplitude do not match to produce an optical force that influences the mirror motion. The mirror amplitude decreases only due to the intrinsic mechanical damping. Although the laser detuning is slowly increased towards zero detuning at some point, in this case at $\Delta/\Omega_m = -12$, the laser detuning and mirror amplitude are such that sidebands created by the mirror motion result in an optical force. However the sign of the optical force has changed compared to the situation with positive detuning. Instead of parametric amplification, now parametric attenuation occurs, resulting in a decrease in mirror amplitude. The interaction of the laser field with the resonator again leads to a resonant cavity field, resulting in peaks at multiples of Δ/Ω_m also for negative laser detunings. This is only visible when the mirror amplitude was driven to large values previously. Driven oscillations at negative laser detunings reveal therefore something about the state and history of the system and are non-trivial.

To compare the experimental result of Fig. 3.2(a) with theory, a numerical simulation is performed with the same experimental parameters. For this we solve numerically Eqs. (3.1) and (3.2) using the following initial conditions: $\alpha(0) = 0$, $\alpha'(0) = 0$, $x(0) = x_0$ and $x'(0) = 0$ where x_0 denotes the initial mirror amplitude x_0 . The value for x_0 is chosen to correspond to the thermal mirror amplitude at 300K: $x_0 = \sqrt{k_b T / m \Omega_m^2}$. Although no mechanical and thermal noises are required to reproduce the experimental results, an initial mirror amplitude is needed to start the

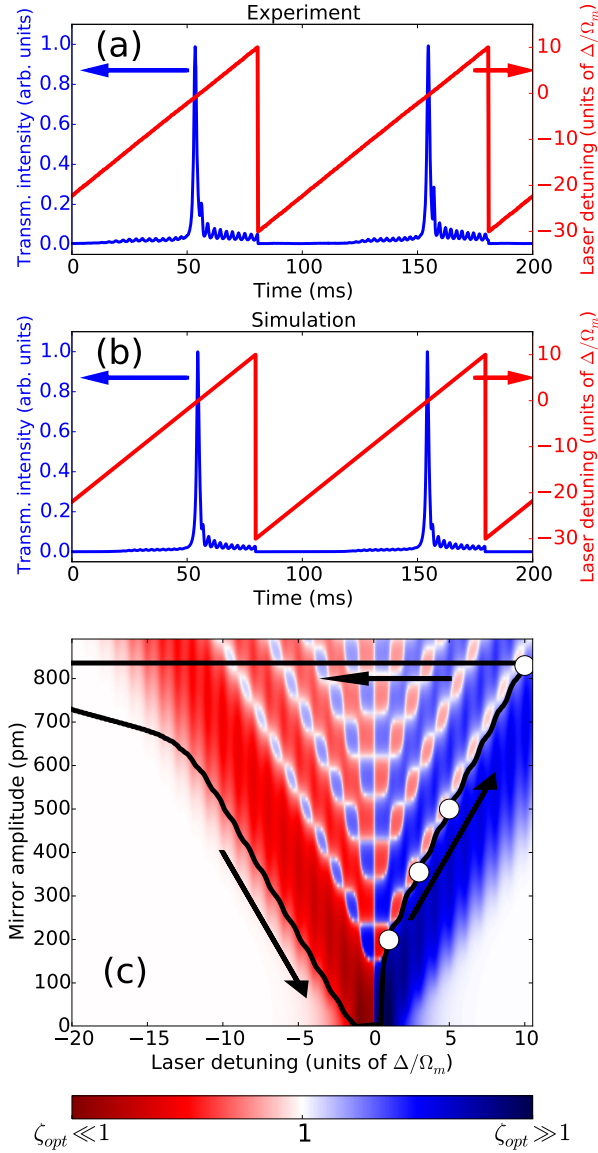


Figure 3.2: (Color) A closed cycle across the attractor diagram. (a) Intensity transmitted by the cavity for two consecutive periods of a controlled laser detuning sweep. (b) Simulation based on Eqs. (3.1)-(3.2). (c) Attractor diagram corresponding to our experimental parameters. The path followed in the experiment is indicated by the arrows.

parametric process.

The results of the simulation, depicted in Fig. 3.2(b), are in good agreement with the experimental results of Fig. 3.2(a). This indicates that our earlier assumption not to include thermal and mechanical noise in Eqs. (3.1) and (3.2) is justified. Furthermore, we do not need to include any second order effects such as heating of the mirror substrates due to absorption. Although from the experimental data the mirror amplitude is not obtained directly, the numerical simulations do contain the mirror amplitude. By plotting the attractor diagram according to Eq. (7.4) together with the mirror amplitude obtained from the simulations, we can visualize the traversed path across the attractor diagram.

In Fig. 3.2(c) the attractor diagram is displayed together with the evolution of the mirror amplitude (indicated by the arrows). The amplitude follows a deterministic path through the diagram. Along this path the optomechanical gain varies. When the gain is large, the path closely follows the $\zeta_{opt} = 1$ contour, whereas in the regions with moderate gain the changing laser detuning prevents the mirror amplitude from reaching the $\zeta_{opt} = 1$ contour as closely. Specifically, for positive laser detunings $\zeta_{opt} \geq 1$ and for negative laser detunings $\zeta_{opt} \leq 1$. It is also worthwhile to emphasize that the mirror amplitude changes on the time scale of the laser scan speed, much slower than the oscillation frequency of the mirror or the cavity lifetime. So far we have thus been discussing the dynamics of a driven, quasi-static, system. However, also interesting dynamics occur on the time scale of the mechanical resonator.

Theoretically the increase in the mirror amplitude, as shown in Fig. 3.2(c), should be visible as an increase in the number of harmonics present in the output field [49]. This is verified by analyzing the fast modulation present in the reflected intensity for several different detunings corresponding to the white dots in Fig. 3.2(c). We have analyzed the reflected intensity as it is picked up by a faster photodetector in our experimental configuration. However the same features should also be visible in the transmitted intensity.

In Fig. 3.3 we compare experimental and numerical results for these fast modulations. For clarity an offset is removed, and the figures are rescaled. The excellent agreement between theory and experiment confirms once more that we have explored in detail the boundary (lowest branch where $\zeta_{opt} = 1$) of the attractor diagram and that this method is suited for further exploration of the attractor diagram. Furthermore, we have significantly amplified the motion of our mechanical resonator, using large intracavity power, without any sign of unstable or chaotic behavior.

To demonstrate that we have full control over our system, we change the starting conditions of our laser frequency sweep after performing a cycle similar to the one displayed in Fig. 3.2. When the mirror amplitude is large, changing the laser detuning slightly makes it possible to skip from the boundary branch to another branch. In this way different branches in the attractor diagram can be explored.

Figure 3.4(a) shows the results of two cycles across the attractor diagram along a different branch. The scale for the transmitted intensity is the same as in Fig. 3.2(a). Although the experimental conditions have only changed a little, the result is quite different from Fig. 3.2(a). Still multiple peaks at Δ/Ω_m are visible, but the main cavity resonance at $\Delta/\Omega_m = 0$ is reduced significantly compared to these sidebands. Also a distinctive dip is visible, indicated with "x". To verify that the features of Fig.

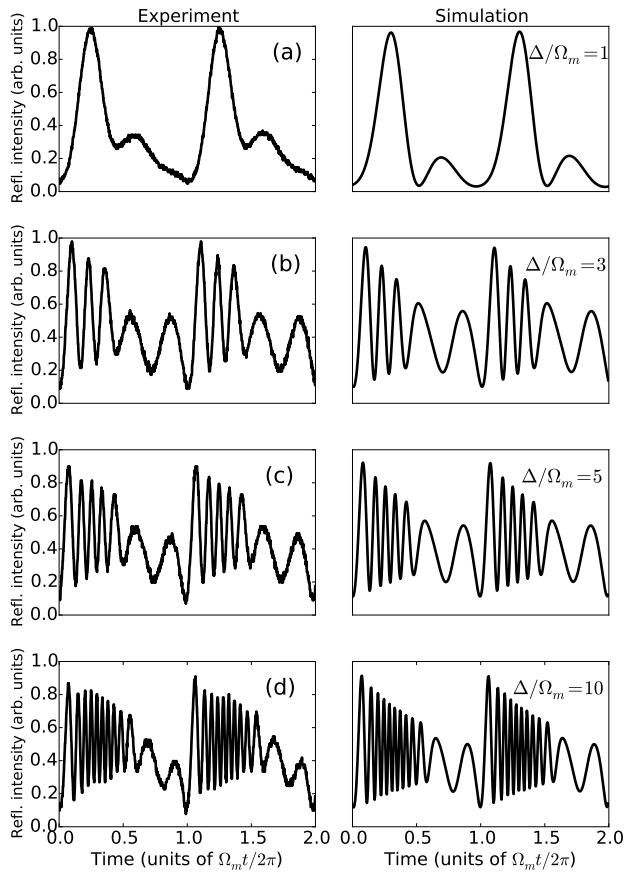


Figure 3.3: Detailed time traces of the reflected cavity intensity for different laser detunings. The left column shows the measurements and the right column shows numerical solutions to Eqs. (3.1) and (3.2). (a)-(d) correspond to specific detunings indicated with white dots in Fig. 3.2(c).

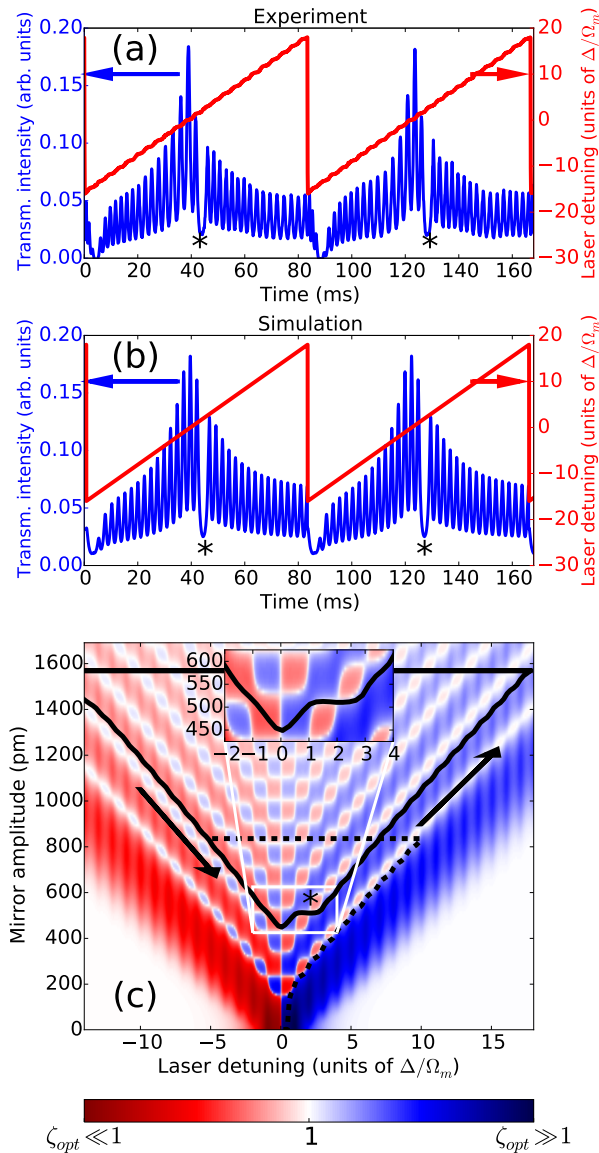


Figure 3.4: (Color) Exploring a higher branch in the attractor diagram. (a) Intensity transmitted by the cavity for two consecutive periods of a controlled laser detuning sweep. The scale for the transmitted intensity is the same as in Fig. 3.2(a) (b) Simulation based on Eqs. (3.1) and (3.2). (c) Attractor diagram together with the path followed in the experiment. Before switching to a higher branch, the system is initialized (dashed line) using a similar detuning sweep as in Fig. 3.2(c). Inset: Zoom of region around zero detuning.

3.4(a) are captured by the theoretical model of Eqs. (3.1)-(3.2), a numerical simulation is performed with the same experimental parameters. The qualitative agreement between experiment and simulation shows that the model is still valid for our system. Furthermore, from the simulation we can again extract the mirror amplitude and use this together with the attractor diagram to explain the features of Fig. 3.4(a).

Figure 3.4(c) shows this attractor diagram. The black dashed line shows the initialization, which is similar to the cycle performed in Fig. 3.2, but now the laser detuning is set back to just $\Delta/\Omega_m = -5$ to reach a different branch. Note that the initialization is not shown in Figs. 3.4(a) and 3.4(b). The solid black line shows the evolution of the mirror amplitude during one cycle. The largest mirror amplitude achieved in this experiment is roughly 1600 pm, more than 500 times the amplitude at 300K without any sign of chaotic or unstable behavior.

For the steady state cycles of Fig. 3.4(a) the reduction in the transmitted intensity at the cavity resonance ($\Delta/\Omega_m = 0$) is now readily explained: The large mirror amplitude reduces the time the cavity is resonant with the input field, therefore less intracavity field is built-up, resulting in a reduction in transmitted intensity.

The inset of Fig. 3.4(c) shows the region where a change from one stable branch to another occurs. This transition occurs at $\{\Delta/\Omega_m = 1.5, A \approx 510 \text{ pm}\}$. At this point the mirror amplitude stays constant along a contour where $\zeta_{opt} = 1$. This point coincides with the distinctive dip in Fig. 3.4(a). When the mirror amplitude does not change, no optical driving force occurs and no sideband is visible in the optical output. Even more interesting is the surrounding area of the attractor diagram. At $\{\Delta/\Omega_m = 1.5, A \approx 510 \text{ pm}\}$ any small change in mirror amplitude is significantly amplified: if the mirror amplitude increases slightly, $\zeta_{opt} \gg 1$ and the mirror amplitude will increase significantly. Similarly, if the mirror amplitude decreases slightly, $\zeta_{opt} \ll 1$ and the mirror amplitude will decrease significantly. The inset therefore highlights a bistability: A small perturbation of the mirror motion will result in a large change in the mirror amplitude. However, our results show that in a clean system such as ours, we can "walk" through such unstable regions on a well-defined path.

3.5 Conclusion

With the absence of any chaotic or unstable behavior our optomechanical system is only described by two equations (Eqs. (3.1) and (3.2)). This has allowed us to explore in detail the optomechanical attractor diagram and the dynamics of self-induced oscillations. By performing a laser frequency sweep, multiple stable branches in the attractor diagram are explored. Furthermore, we have demonstrated non-trivial dynamics, such as driven oscillations for negative laser detunings and the presence of a bistability.

Threshold behavior of self-induced oscillations

In early stages of this work, the threshold behavior of self-induced oscillations was investigated. In particular, the influence of laser input power and mechanical decay

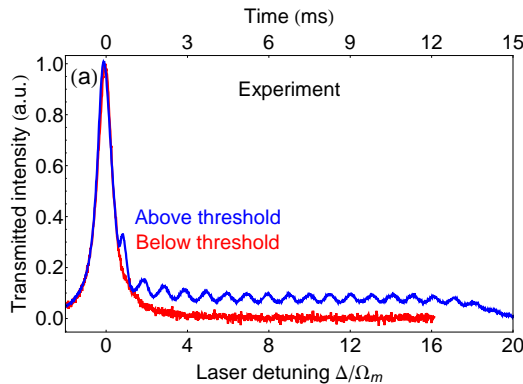


Figure 3.5: Resulting transmitted intensity for a linear laser frequency sweep at 400 MHz/s. Additional side-band are only visible with sufficient laser power.

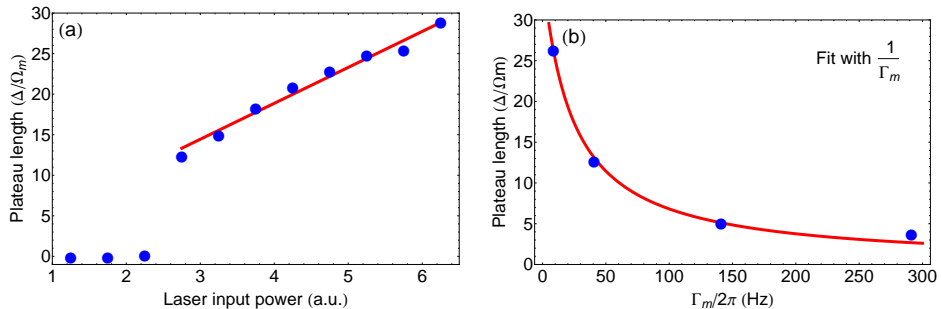


Figure 3.6: Verification of optomechanical gain. (a) Influence of laser input power on plateau length for fixed mechanical damping rate Γ_m ($Q_m = 34000$). (b) Influence of mechanical damping rate Γ_m on plateau length for fixed laser input power.

rate Γ_m . A set-up with the following parameters was used: $\kappa = 300 \times 10^3 \times 2\pi$ rad/s, $\kappa_{ex} = 50 \times 10^3 \times 2\pi$ rad/s, $\Omega_m = 300 \times 10^3 \times 2\pi$ rad/s, $\Gamma_m = 8.8 \times 2\pi$ rad/s (or $Q_m = 34000$) at 10^{-6} mbar and $m = 110 \times 10^{-12}$ kg.

In Fig. 3.5 the transmitted intensity is shown when a linear laser frequency sweep is performed for low (red) and high (blue) laser power. Side-bands are only visible above a minimum laser power and the length of this plateau of side-bands is a measure for the condition $\zeta_{opt}(\Delta, A) > 1$. This length can be used to show the threshold behavior, as is shown in Fig. 3.6(a). Only with a certain minimal laser power do the self-induced oscillations start. In accordance with Eq. (3.3), the number of side-bands visible scales linearly with power.

Besides laser power, the influence of the mechanical damping rate Γ_m was also investigated by changing the pressure in the vacuum chamber and thereby altering Γ_m . The results, shown in Fig. 3.6(b), demonstrate the correct $1/\Gamma_m$ dependency as predicted by Eq. (3.3). Therefore, the number of side-bands visible in Fig. 3.5 are a correct measure to investigate the condition $\zeta_{opt}(\Delta, A) > 1$ in an optomechanical system.

Acknowledgments

The authors would like to thank H. van der Meer for technical assistance and support. The authors are also grateful for useful discussions with M.P. van Exter, W. Loeffler, and G. Welker. This work is part of the research program of the Foundation for Fundamental Research on Matter (FOM) and of the NWO VICI research program, which are both part of the Netherlands Organisation for Scientific Research (NWO). This work is also supported by National Science Foundation Grant No. PHY-1212483.

A simple method to measure optomechanically induced transparency

Driving an optomechanical system with a single laser leads already to interesting dynamics, as is shown in the previous chapter. In this chapter, we demonstrate a simple method to measure optomechanically induced transparency (OMIT) in a Fabry-Perot based system using a trampoline resonator. In OMIT, the transmitted intensity of a weak probe beam in the presence of a strong control beam is modified via the optomechanical interaction, leading to an ultra-narrow optical resonance. To retrieve both the magnitude and the phase of the probe beam, a homodyne detection technique is typically used. We have greatly simplified this method by using a single acousto optical modulator to create a control and two probe beams. The beat signal between the transmitted control and probe beams shows directly the typical OMIT characteristics. This method therefore demonstrates an elegant solution when a homodyne field is needed but experimentally not accessible.

4.1 Introduction

Cavity optomechanics has attracted much attention recently, see Ref. [16] for an overview. This attention is partly due to the prospect of performing experiments involving non-classical states of a macroscopically sized object. Such experiments typically overcome the thermal mechanical motion by preparing the system in the quantum mechanical ground state. For applications such as light storage [56], optical wavelength conversion [57] and delay lines [58], ground state cooling is not a strict requirement. For example, an optomechanical delay line can be constructed around the effect of optomechanically induced transparency or OMIT, the optomechanical equivalent to electromagnetically induced transparency (EIT) [59, 60] in atomic systems. This effect is achieved by driving the system with two tones, a control and probe beam, and has been demonstrated by several groups [61, 62, 63, 64, 65], showing that OMIT has become a powerful tool to characterize optomechanical systems. Consequently, different measurement schemes have been used to perform these measurements. Here we demonstrate a straightforward, easy to implement method to perform OMIT, together with a detailed model to analyze the data. Our method is not restricted to a particular optomechanical system, nor does it require to be in the side-band resolved regime.

Using a membrane-in-the-middle set-up, Karuza et al. have shown how the transmitted control beam can be used as a phase reference to perform a modified heterodyne detection technique [63]. Here we expand on this idea by measuring the beat signal from the control and probe beam, but instead of using multiple acoustic-optical modulators (AOMs), we use a single AOM to create a control and two probe beams via double side-band generation. Although a similar experiment has been performed using a single electro-optical modulator (EOM) [65], we provide significantly more theoretical and experimental details. For example, the presence of two probes instead of one requires modification of the OMIT theory as we will show below.

This method is especially advantageous with low mechanical frequency systems. The typical frequency difference between pump and probe beam is between 100 kHz and 1 MHz for such systems. The OMIT feature itself however, is of the order of the mechanical linewidth [66]. Therefore the laser frequencies involved, need to be set with high precision. This can best be accomplished using a lock-in amplifier. The reference frequency output of the lock-in amplifier modulates the RF drive to the AOM to generate the pump and two probes, while the transmitted intensity is recorded with the same lock-in amplifier. In this way the change in probe detuning can not only be monitored with sub-Hz precision, but the common path of both control and probe beams greatly increases the stability of the experiment.

First, we briefly describe the OMIT theory and show the modifications needed for the two probe measurements. After the experimental details, we show how the typical OMIT features, namely an ultra-narrow optical resonance, are recorded by independently controlling both control and probe beam, something which was not possible in the work of Karuza et al. Finally, the results are compared with theory. We find a good agreement and are able to reduce the transmitted intensity of the probe beam by more than 4 orders of magnitude, resulting in a final optomechanical

cooperativity of 144 ± 5.2

4.2 Theory

A detailed theory for OMIT can be found in the work by Agarwal et al. [66]. A short summary is given by Aspelmeyer et al. [16] of which we will repeat the key points.

The principle of OMIT is the following: a strong control beam is placed on the lower side-band at a laser detuning of $\Delta = -\Omega_m$, where Ω_m is the frequency of the mechanical resonator. A second, weak, probe beam is placed at the cavity resonance, such that the mechanical resonator is driven by the two photon interaction with both probe and control beam. This is schematically depicted in Fig. 4.1(a). The strongly driven mechanical resonator modulates the control beam and creates Stokes and anti-Stokes side-bands, indicated in blue in Fig. 4.1(a). The interference between side-band and probe beam reduces the amplitude and changes the phase of the transmitted probe beam. The dispersive behavior of the transmitted probe beam results in a change in group velocity and can be viewed as a delay of the propagating beam.

For a Fabry-Perot based system, the field of a single transmitted probe in the presence of a strong control beam is given by the following expression:

$$t_p = \eta \kappa \frac{\chi_{aa}(\Omega)}{1 + g^2 \chi_{mech}(\Omega) \chi_{aa}(\Omega)} \quad (4.1)$$

with the following parameters: $\eta = \frac{\kappa_{ex}}{\kappa}$ is the coupling efficiency, κ is the cavity linewidth, κ_{ex} is the input coupling rate, Γ_m is the mechanical linewidth, g is the optomechanical multi-photon coupling rate, $\chi_{aa}(\Omega)$ is the optical susceptibility defined as $\chi_{aa}^{-1}(\Omega) = -i(\Omega + \Delta) + \kappa/2$ and $\chi_{mech}(\Omega)$ is the mechanical susceptibility defined as $\chi_{mech}^{-1}(\Omega) = -i(\Omega - \Omega_m) + \Gamma_m/2$. We have introduced the detuning of the control beam as $\Delta = \omega_{control} - \omega_{cavity}$ and the detuning of the probe beam as $\Omega = \omega_{probe} - \omega_{control}$. Note that compared to some previous work [61, 58], we use a Fabry-Perot based system. When measuring the transmitted probe, instead of a transparency window a dark window will appear. Effectively the transmission and reflection signals are exchanged when comparing a Fabry-Perot system with a waveguide coupled cavity. We will however still refer to an OMIT feature to be consistent with existing literature.

In our experiment the transmitted intensity of two probes spaced symmetrically around the control beam is measured, see Fig. 4.1(b). In the side-band resolved regime, where $\kappa \ll \Omega_m$, probe 1 can be ignored. The experiment presented here operates in the regime where $\kappa \approx \Omega_m$, so a portion of probe 1 is still transmitted and the presence of this probe beam cannot be ignored. To accurately describe the experiment, Eq. (4.1) is modified in the following way (see appendix):

$$t_p = \eta \kappa \frac{2\chi_{aa}(\Omega) [-i + \chi_{aa}(\Omega)\Omega]}{-i + 2\chi_{aa}(\Omega)\Omega [1 + g^2 \chi_{mech}(\Omega) \chi_{aa}(\Omega)]}. \quad (4.2)$$

The transmitted intensity is obtained via $|t_p|^2$.

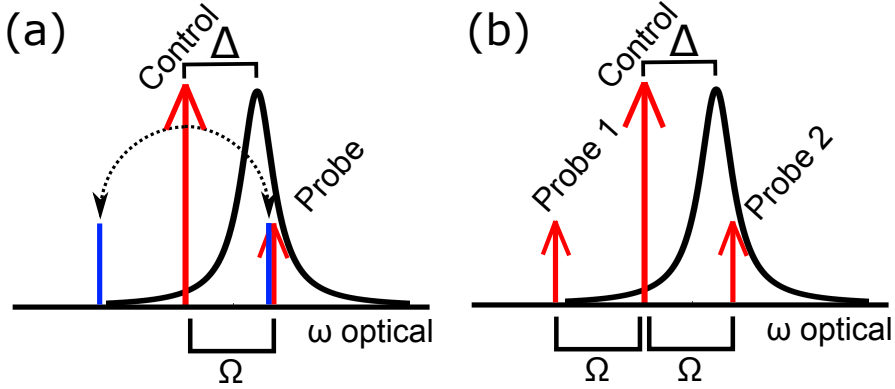


Figure 4.1: Schematic overview of the placement and relative location for the control and probe beam. Δ indicates the detuning of the control beam with respect to the cavity resonance, and Ω is the probe detuning with respect to the control beam. (a) The case with only a single probe. The two blue lines indicate the Stokes and anti-Stokes side-bands generated via the optomechanical interaction. (b) The case presented in this work, where two probes are used.

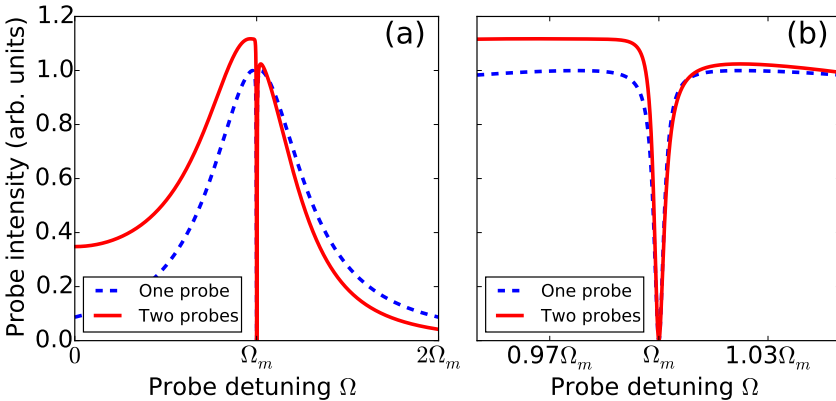


Figure 4.2: (a) Comparison of OMIT feature for one transmitted probe (blue) and two transmitted probes (red) with $\Omega_m = 1.6\kappa$. The control beam is placed at $\Delta = -\Omega_m$ and the probe detuning Ω is varied. (b) Close-up of the OMIT feature.

The transmitted intensity for both the single probe (blue) and two probes (red) are shown in Fig. 2, for $\Delta = -\Omega_m$ and $\Omega_m = 1.6 \kappa$ while varying the probe detuning Ω . The presence of the two probes modifies the OMIT feature slightly, but this effect becomes smaller when the ratio Ω_m/κ increases. Note that the typical OMIT dip is still nicely visible when using two probes. This is important because from this dip both the total effective damping rate Γ_{eff} and the multi-photon cooperativity $C = 4g^2/\kappa\Gamma_m$ can be extracted. A convenient way to do this, is to measure the transmitted intensity on resonance, i.e. with $\Delta = -\Omega_m$ and $\Omega = \Omega_m$, which is given by

$$|t_p|^2 = \left(\frac{2\eta}{1+C} \right)^2 \left| 1 + \frac{1+2C}{1+i4(1+C)\Omega_m/\kappa} \right|^2. \quad (4.3)$$

In the sideband resolved limit, $\kappa \ll \Omega_m$, this reduces to the familiar expression [61, 58]:

$$|t_p|^2 = \left(\frac{2\eta}{1+C} \right)^2. \quad (4.4)$$

Finally, not only the magnitude of the transmitted probe but also the phase of the probe changes when varying the probe detuning. The dispersive behavior of the transmitted probe beam leads to a group delay. The argument of Eq. (2) gives the phase of the probe and the group delay is obtained by taking the derivative of the phase:

$$\tau_g = \frac{d\phi}{d\Omega} \quad (4.5)$$

For $\Delta = -\Omega_m$, $\Omega = \Omega_m$ and assuming $\kappa \gg \Gamma_m$ the group delay is given by

$$\tau_g = -\frac{2}{\Gamma_m} \left(\frac{C}{C+1} \right) \left(1 + \frac{1}{1+16(1+C)^2\Omega_m^2/\kappa^2} \right). \quad (4.6)$$

which in the limit for $C \gg 1$ results in $\tau_g = -\frac{2}{\Gamma_m}$. Both the magnitude and the phase of the OMIT feature can therefore be used to derive the system parameter C .

4.3 Experimental details

Our optomechanical system consist of a 5 cm long Fabry-Perot cavity with a transpoline resonator as one of the end mirrors. As mentioned before we use a single AOM to generate a control and two probe beams. To eliminate cavity or laser drift we use the scheme outlined in Eerkens et al. [67]. One laser (Laser 1 in Fig. 4.3) is locked to the cavity resonance via the Pound-Drever-Hall (PDH) technique [38]. This laser serves purely as a reference and is not used to read out the motion of the resonator. A second laser (Laser 2 in Fig. 4.3) is, with a variable frequency offset, locked to the first laser one free spectral range away using an optical phase locked loop. From this second laser the control and probe beams are derived. An overview of the experimental set-up is presented in Fig. 4.3. To be able to measure OMIT, our existing set-up is expanded to include an AOM and lock-in amplifier. These components are highlighted with the blue dashed line. The lock-in amplifier is used to

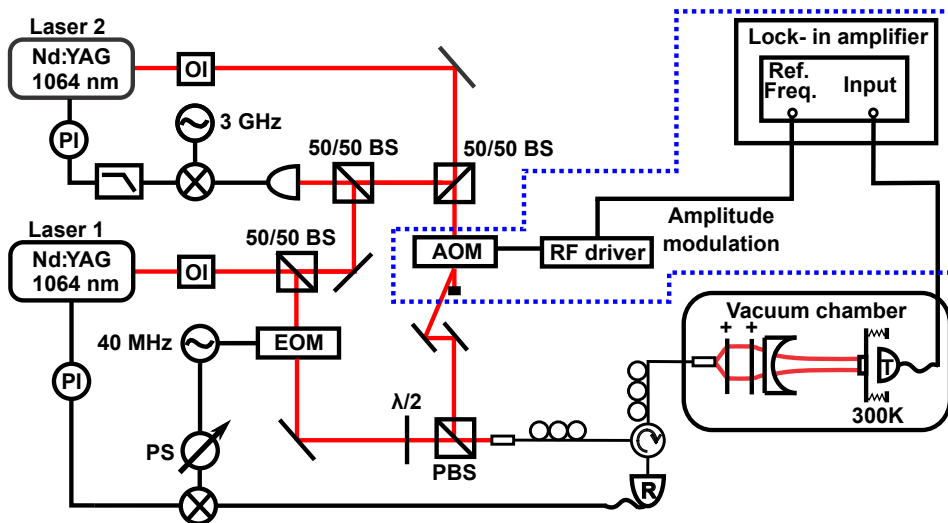


Figure 4.3: Experimental set-up. This is a modified version of the set-up presented by Eerkens et al. [67]. The additional components needed to measure OMIT are highlighted with the dashed blue line. The RF drive signal to the AOM is modulated at the reference frequency of the lock-in amplifier to create a control and two probe beams. The transmitted intensity of the control and probe beams is analyzed using the lock-in amplifier. The components displayed are: LO: local oscillator, BS: beam splitter, PBS: polarizing beam splitter, EOM: electro-optical modulator, OI: optical isolator and PI: proportional-integral feedback controller

modulate the RF drive to the AOM, generating two probes via double sideband generation. By adjusting the modulation frequency, the detuning of the probe beams is set. The power of the control beam is adjusted by changing the magnitude of the RF drive to the AOM, while the power of the probe beams is adjusted by changing the amplitude of the modulation. Typically only a few μW of optical power is used for the probe beams, while the power of the control beam can be varied separately. The transmitted intensity is recorded using a photodetector and analyzed using the same lock-in amplifier to obtain both phase and amplitude of the transmitted probes.

The measurements are performed using a nested trampoline resonator [35]. The optical and mechanical properties of the system are characterized separately. Via an optical cooling experiment (see Ref. [67]) the optical linewidth is determined to be 185 ± 4 kHz. Based on the reflected and transmitted intensity, the coupling efficiency η is estimated to be 0.3. The mechanical resonator is characterized by measuring its mechanical thermal noise spectrum with a side-of-fringe lock to a low finesse cavity. An intrinsic mechanical linewidth of $\Gamma_m = 30 \pm 0.1$ Hz and a mechanical frequency of 291.8 kHz was obtained. The mode-mass of the resonator is, via COMSOL, estimated to be 180 ng. Although these parameters are relatively modest compared to our previous work (see Ref. [35]), they suffice for demonstrating optomechanically induced transparency.

4.4 Results

To demonstrate optomechanically induced transparency, the probe intensity and phase are recorded while the probe detuning Ω is varied. In Fig. 4.4 the results are shown for five different pump detunings Δ . Regardless of the pump detuning, a significant dip in probe intensity always occurs for a probe detuning $\Omega = \Omega_m$. This is a key feature of OMIT. Experiment and theory are in good agreement, as evidenced by the fitted red line using Eq. (4.2). For the fit three free parameters are used: pump detuning Δ , optical linewidth κ and pump laser power. The value for the optical linewidth, 193 ± 4 kHz, is in agreement with the separate characterization of the set-up.

To investigate the OMIT feature in more detail, the control beam is set at $\Delta = -\Omega_m$ and the probe detuning is varied around $\Omega \approx \Omega_m$. The effect of pump power is shown in Fig. 4.5. The top two panels show the intensity of the transmitted probe and the intensity of the transmitted probe on resonance. The transmitted probe intensity can be changed more than four orders of magnitude by varying the power of the control beam. The bottom panels show the phase of the transmitted probe and the group delay derived from the derivative of the phase, see Eq. (4.5). The dashed line is the theoretical minimum set by $-2/\Gamma_m$. Note that a negative group delay suggests a superluminal group velocity, an effect which has been studied extensively in the past (see Ref. [68] for an overview). Both the transmission on resonance and group delay can be fitted using Eqs. (4.3) and (4.6) to obtain the optomechanical cooperativity for each control beam power. For the highest laser power a maximum cooperativity of 144 ± 5 is achieved.

We can also achieve optomechanically induced amplification by setting the de-

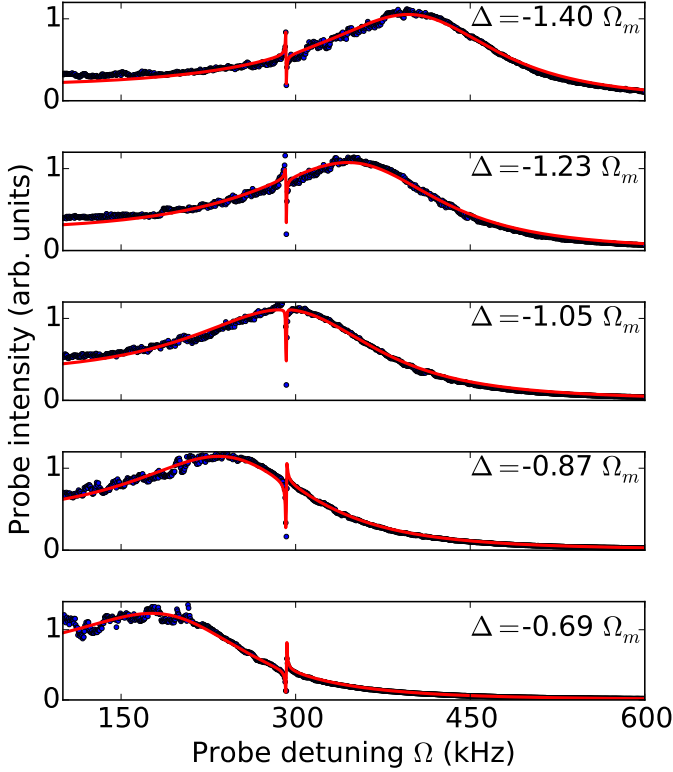


Figure 4.4: Demonstration of optomechanical induced transparency. The probe detuning Ω is varied for different values of the pump detuning Δ .

tuning of the control beam to $\Delta = +\Omega_m$. Note that the system is only stable when the effective mechanical damping is still positive, which requires $C < 0.5$ when critical coupling is assumed. Increasing the control beam power further leads to parametric amplification of the mechanical mode. The result of a blue detuned control beam is shown in Fig. 4.6. Now an increase in transmitted probe together with a positive group delay of 5.9 ms is achieved. Comparing this delay to the cavity lifetime shows that the delay has increased with a factor of 3700. As before, the maximum delay is limited to $2/\Gamma_m = 10.6$ ms. Increasing the mechanical quality factor will create a longer delay, but this requires also careful adjustment of the control beam power to stay below the threshold for parametric amplification. However, a delay of 5.9 ms is already significant; more than 1000 km of fiber is needed to achieve the same effect.

As demonstrated above, all the typical OMIT features are reproduced using the method with two probe beams. Furthermore, the increased stability of the common path of both local oscillator and signal is beneficial for a wide variety of experiments. Finally, for some experimental configurations the implementation of a homodyne/heterodyne detection scheme is technically not possible. The method presented in this work is an elegant solution to this problem.

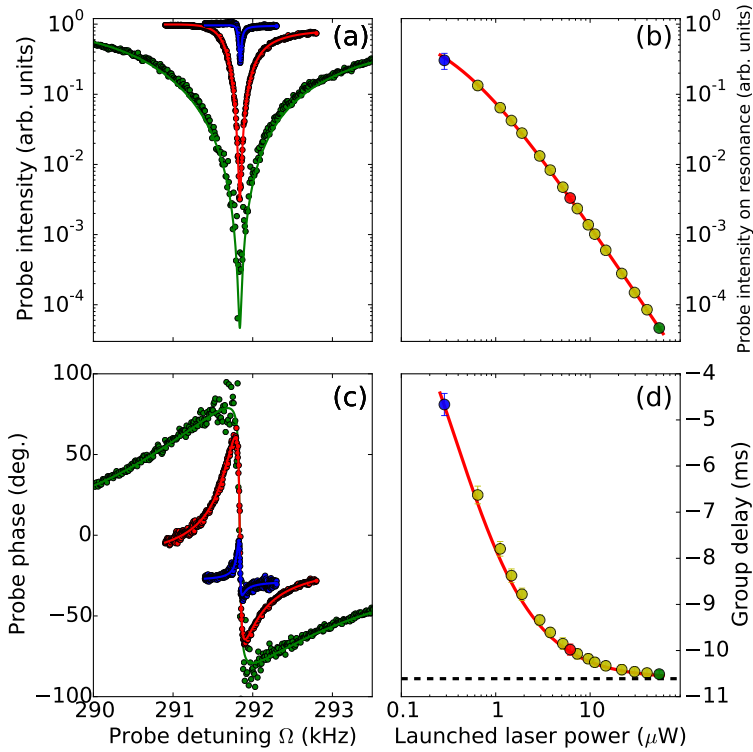


Figure 4.5: For a fixed control detuning of $\Delta = -\Omega_m$ the control beam power is varied. (a) The transparency window increases with laser power. (b) Transmitted probe intensity on resonance. (c) Phase of the transmitted probe. (d) Group delay obtained via the derivative of the phase.

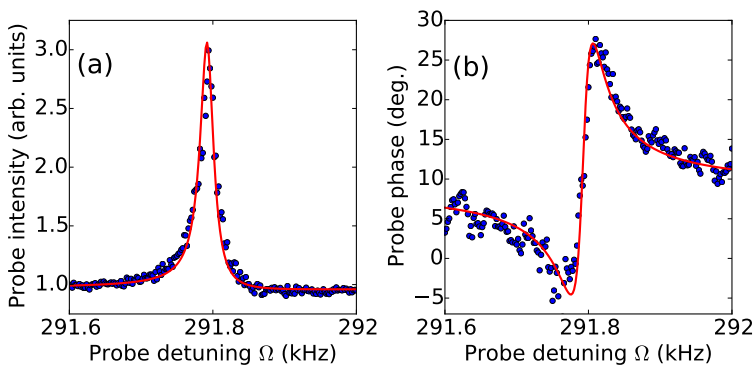


Figure 4.6: Demonstration of optomechanically induced amplification by placing the pump at $\Delta = +\Omega_m$. (a) Transmitted probe intensity (b) Phase of transmitted probe.

4.5 Conclusion

In conclusion, we have presented a simple and straightforward method to measure optomechanically induced transparency. Using a single AOM and lock-in amplifier, OMIT can easily be measured with full control and high precision of both control and probe detuning. The working principle is demonstrated using a relatively modest optomechanical system in terms of system parameters, making this method applicable to a wide variety of systems. Furthermore, the modified heterodyne technique demonstrated here as well as the generation of multiple tones via a single AOM can be applied to a variety of experiments within the field of optomechanics.

Derivation of the transmission with two probes

Here we briefly show how Eq. (4.2) is derived using an approach similar to Weis et al. [61]. The classical optomechanical equations (in the rotating frame) are the following:

$$\frac{da(t)}{dt} = (i(\Delta + Gx(t)) - \frac{\kappa}{2})a(t) + \sqrt{\eta\kappa}s_{in}(t) \quad (4.7)$$

$$\frac{d^2x(t)}{dt^2} = -\Gamma_m \frac{dx(t)}{dt} - \Omega_m^2 x(t) + \frac{\hbar G}{m} |a(t)|^2 \quad (4.8)$$

in which $a(t)$ is the optical field inside the cavity, G the optical frequency shift per displacement, $x(t)$ the mechanical displacement and $s_{in}(t)$ the input field.

The motion of the harmonic oscillator can be treated as a small perturbation around some mean displacement: $x(t) = \bar{x} + \delta x(t)$. Similarly the effect of this motion on the cavity field can be treated as a perturbation: $a(t) = \bar{a} + \delta a(t)$. Substituting these assumptions in Eqs. (4.7) and (4.8) yields:

$$\frac{d\delta a(t)}{dt} = (i[\Delta + G(\bar{x} + \delta x(t))] - \frac{\kappa}{2})(\bar{a} + \delta a(t)) + \sqrt{\eta\kappa}(\bar{s}_{in} + \delta s_{in}(t)) \quad (4.9)$$

$$\begin{aligned} \frac{d^2\delta x(t)}{dt^2} = & -\Gamma_m \frac{d\delta x(t)}{dt} - \Omega_m^2(\bar{x} + \delta x(t)) + \\ & \frac{\hbar G}{m} [(\bar{a} + \delta a(t))(\bar{a}^* + \delta a^*(t))] \end{aligned} \quad (4.10)$$

Setting $\delta a(t) = 0$ and $\delta x(t) = 0$ results in the following steady state solution:

$$\bar{a} = \frac{\sqrt{\eta\kappa}\bar{s}_{in}}{i(\Delta + G\bar{x}) - \kappa/2} \quad (4.11)$$

$$\bar{x} = \frac{\hbar G}{m\Omega_m^2} |\bar{a}|^2. \quad (4.12)$$

Inserting the steady state solution back in Eqs. (4.9) and (4.10) leads to the following equations for $\delta x(t)$ and $\delta a(t)$:

$$\frac{d\delta a(t)}{dt} = (i\Delta - \frac{\kappa}{2})\delta a(t) + iG\bar{a}\delta x(t) + \delta s_{in}(t) \quad (4.13)$$

$$\frac{d^2\delta x(t)}{dt^2} = -\Gamma_m \frac{d\delta x(t)}{dt} - \Omega_m^2 \delta x(t) + \frac{\hbar G\bar{a}}{m} [\delta a(t) + \delta a^*(t)] \quad (4.14)$$

Note that we have dropped second-order terms and assumed that the static radiation pressure is negligible.

Instead of a single probe as the input, we now have two probes at frequencies $\pm\Omega$, therefore $\delta s_{in}(t) = s_p (e^{-i\Omega t} + e^{+i\Omega t})$. As an ansatz to solve Eqs. (4.13) and (4.14) we use the following:

$$\delta a(t) = A^- e^{-i\Omega t} + A^+ e^{+i\Omega t} \quad (4.15)$$

$$\delta a^*(t) = (A^+)^* e^{-i\Omega t} + (A^-)^* e^{+i\Omega t} \quad (4.16)$$

$$\delta x(t) = X e^{-i\Omega t} + X^* e^{+i\Omega t}. \quad (4.17)$$

Inserting the drive $\delta s_{in}(t)$ and the ansatz back in Eqs. (4.13 - 4.14), and solving for A^- and A^+ results in:

$$A^+ = s_p \sqrt{\eta\kappa} \frac{\chi_{aa}(\Omega) [i - 2\chi_{aa}(\Omega)\Omega]}{-i + 2\chi_{aa}(\Omega)\Omega [1 + g^2\chi_{mech}(\Omega)\chi_{aa}(\Omega)]} \quad (4.18)$$

$$A^- = s_p \sqrt{\eta\kappa} \frac{i\chi_{aa}(\Omega)}{-i + 2\chi_{aa}(\Omega)\Omega [1 + g^2\chi_{mech}(\Omega)\chi_{aa}(\Omega)]}. \quad (4.19)$$

This is the resulting field for each probe inside the cavity. In the end we measure, via the beat with the control beam, the coherent sum of the two transmitted probes, therefore:

$$t_p = \frac{\sqrt{\eta\kappa}}{s_p} [A^+ + A^-] \quad (4.20)$$

which after some manipulation leads to Eq. (4.2).

In the presence of additional optical losses, defined as κ_{loss} , the transmitted probe of Eq. 4.20 becomes:

$$t_p = \frac{\eta\kappa}{s_p(\sqrt{\eta\kappa} + \sqrt{\kappa_{loss}})} [A^+ + A^-] \quad (4.21)$$

Acknowledgments

The authors would like to thank H. van der Meer for technical assistance. The authors are also grateful for useful discussions with W. Loeffler. This work is part of the research program of the Foundation for Fundamental Research (FOM) and of the NWO VICI research program, which are both part of the Netherlands Organisation for Scientific Research (NWO).

Optical side-band cooling of a low frequency optomechanical system

Having discussed in the previous chapters ways to optical drive the mechanical resonator, in this chapter we will show how optical side-band cooling can be used to significantly reduce the effective mechanical mode temperature.

In particular, we report optical side-band cooling from room temperature for a 1.5×10^{-10} kg (mode mass), low frequency side-band resolved optomechanical system based on a 5 cm long Fabry-Perot cavity. By using high-quality Bragg mirrors for both the stationary and the micromechanical mirror we are able to construct an optomechanical cavity with an optical linewidth of 23 kHz. This, together with a resonator frequency of 315 kHz, makes the system operate firmly in the side-band resolved regime. With the presented optomechanical system parameters cooling close to the ground state is possible. This brings us one step closer to creating and verifying macroscopic quantum superpositions.

The work presented in this chapter is based on: H.J. Eerkens, F.M. Buters, M.J. Weaver, B. Pepper, G. Welker, K. Heeck, P. Sonin, S. de Man and D. Bouwmeester, "Optical side-band cooling of a low frequency optomechanical system", *Optics Express* 23.6 (2015): 8014-8020

5.1 Introduction

In optomechanics, interesting phenomena occur when the photon-phonon coupling is sufficiently large. Amongst other things side-band cooling to the quantum mechanical ground state [39, 40], electromagnetically induced transparency (EIT) [61, 58] and coherent state transfer [44, 46] have been demonstrated. For all these experiments good optical and mechanical quality of the setup is required.

To use side-band cooling to reach the quantum mechanical ground state of a mechanical resonator, the cavity linewidth κ needs to be smaller than the mechanical resonator frequency Ω_m (side-band resolved regime) [21, 20]. This condition is not sufficient, since it does not specify the number of photons required, the maximum environmental temperature and the requirements for the mechanical damping rate Γ_m . A more suitable parameter is the multi-photon cooperativity: $C = 4g_0^2\bar{n}_{cav}/(\kappa\Gamma_m)$ with $g_0 = (\omega_{cav}/L)\sqrt{\hbar/2m\Omega_m}$ the optomechanical coupling rate, ω_{cav} the cavity resonance frequency, L the cavity length, m the mode mass and \bar{n}_{cav} the mean cavity photon number. When $C + 1 \gg \bar{n}_{th}$, with \bar{n}_{th} the mean phonon number of the environment, optical cooling to the ground state is possible [16].

From the cooperativity it is clear that indeed a good mechanical (small Γ_m) and optical quality factor (small κ) are needed. It also follows that when the mode mass of the mechanical resonator becomes larger, the requirements on the other parameters become more strict. Therefore most of the optomechanical devices investigated so far operate in the small mass (below $\sim 1 \times 10^{-12}$ kg), high frequency (above 1 MHz) range [69, 70, 71, 40, 39, 72, 73]. However, to investigate the possible involvement of gravity in the quantum to classical transition of macroscopic superpositions, large mass resonators are essential [8, 9, 14, 43]. Another difficulty in using large mass resonators for these purposes is the low mechanical frequency, which makes reaching the side-band resolved regime difficult.

Here we present a 315 kHz optomechanical system that is sufficiently side-band resolved for ground state cooling. We have constructed an optomechanical system based on a Fabry-Perot cavity with a trampoline resonator as moving end mirror [33]. The trampoline resonator consists of a circular mirror (diameter 70 μm) hanging from four 200 μm long Si_3N_4 arms. High-quality Bragg mirrors (alternating $\text{Ta}_2\text{O}_5/\text{SiO}_2$ layers with 22 ppm transmission loss and order ppm absorption) on both the stationary and the micromechanical mirror allow us to construct a side-band resolved cavity with $\Omega_m/\kappa \approx 13.5$.

To demonstrate the capabilities of our system, we perform a side-band cooling experiment where we have \sim kHz resolution of the pump laser frequency with respect to the cavity resonance. We match the experimental results to theory and find excellent agreement. The system parameters found with the side-band cooling experiment are in good agreement with parameters found from characterization measurements. These results show that with a lower base temperature, ground state cooling should be achievable. This brings investigation of the quantum to classical transition with large mass resonators one step closer.

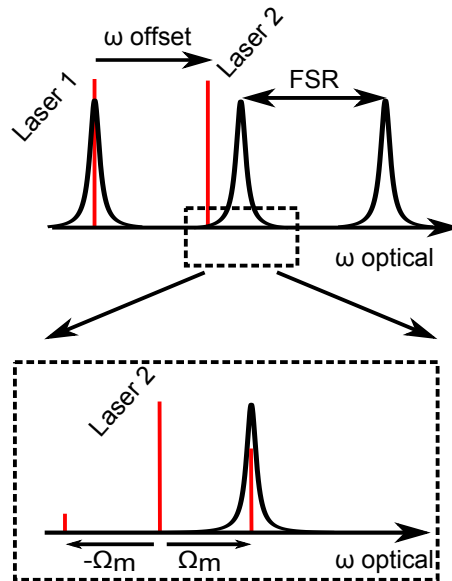


Figure 5.1: The laser scheme used for side-band cooling. Laser 1 is locked to a cavity resonance and laser 2 is locked to the first laser with a variable offset. Inset: Laser 2 is placed precisely one mechanical frequency below a cavity resonance for optimal cooling.

5.2 Experiment

Our system consists of a 5 cm long Fabry-Perot cavity, operating around 1064 nm, with a trampoline resonator as the moving end mirror [33]. The trampoline resonator used in the experiments presented here has a mirror diameter of 70 μm , a resonance frequency of 315 kHz, and a mode mass of 1.5×10^{-10} kg (determined using COMSOL). The optical quality of the cavity is obtained by measuring an optical cavity ring-down. For this, a resonant laser beam is quickly shut down with an acousto-optical modulator (AOM) and the decaying intensity of the transmitted light is recorded. Characterization of the mechanical resonator is done by measuring its mechanical thermal noise spectrum with a laser locked to a cavity resonance using the Pound-Drever-Hall (PDH) technique [38]. The laser power is kept sufficiently low to avoid optomechanical effects on the mechanical linewidth.

Optical side-band cooling occurs when a laser is placed precisely one mechanical frequency below a cavity resonance (see inset in Fig. 1). Interaction of the laser with the mechanical resonator leads to up- and down-conversion of the laser frequency, creating an upper and lower side band. The upper side band is resonant with the cavity and the up-conversion process is therefore enhanced compared to the down-conversion process. The net effect is the extraction of energy (phonons) from the mechanical mode of the resonator.

Since the experiment is carried out at room temperature, thermal drift and low frequency mechanical noise can potentially limit the measurement time. To compen-

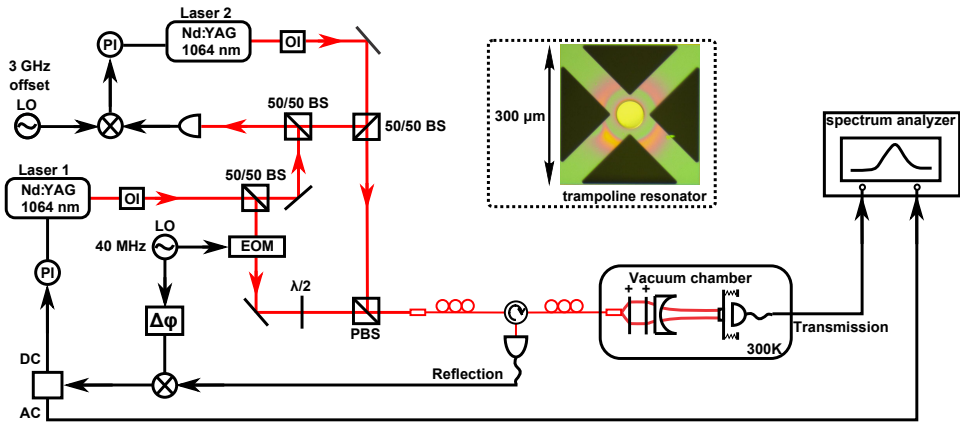


Figure 5.2: Simplified schematic of the optical setup. The frequency of laser 1 is locked to the optomechanical cavity using Pound-Drever-Hall (PDH) technique. Laser 2 is locked to laser 1 via an optical phase-locked loop (OPLL). Laser 2 is tuned one free spectral range (FSR) apart from laser 1 to avoid interference at frequencies relevant to the experiment. The components displayed are: LO: local oscillator, BS: beam splitter, PBS: polarizing beam splitter, EOM: electro-optical modulator, OI: optical isolator and PI: proportional-integral feedback controller. Inset: optical image of the trampoline resonator.

satte for these, a measurement scheme containing two lasers is used. The frequency of one laser, laser 1 in Fig. 1, is locked to a cavity resonance using the PDH technique. This laser follows slow changes in the cavity length and provides a frequency reference for the second laser, laser 2 in Fig. 1. This second laser is locked with a tunable frequency difference to the first laser with an optical phase-locked loop (OPLL) operating around 3 GHz. The frequency offset is chosen such that the second laser is close to the next cavity resonance, one free spectral range (FSR) away, to avoid unwanted interference of the two lasers at frequencies relevant to the experiment.

Figure 2 shows a simplified schematic of the optical setup. For clarity, the optical components needed for the optical cavity ring-down measurement are omitted. The optomechanical cavity is placed inside a vacuum chamber ($p < 10^{-5}$ mbar) with several eddy current dampers and springs. Two \sim kHz linewidth piezo-tunable Nd:YAG lasers operating at 1064 nm are used. To realize the PDH locking scheme, laser 1 is sent through an electro-optical modulator (EOM) [38]. The light reflected from the cavity is, via a fiber circulator, picked up with an avalanche photodiode (APD). The electrical signal is mixed with the local oscillator (LO) at 40 MHz that also drives the EOM. The low-frequency part is routed to a PI controller (\sim 30 kHz bandwidth) to lock the frequency of laser 1 to a cavity resonance. The high-frequency part is sent to a spectrum analyzer to record the mechanical thermal noise spectrum of the mechanical resonator, both for the mechanical characterization and for the side-band cooling experiment.

To lock laser 2 with a variable frequency difference to laser 1 via an OPLL, the beat signal of laser 1 and 2 is continuously monitored using a fast PIN diode. This signal is mixed with a local oscillator around 3 GHz to provide the error signal for

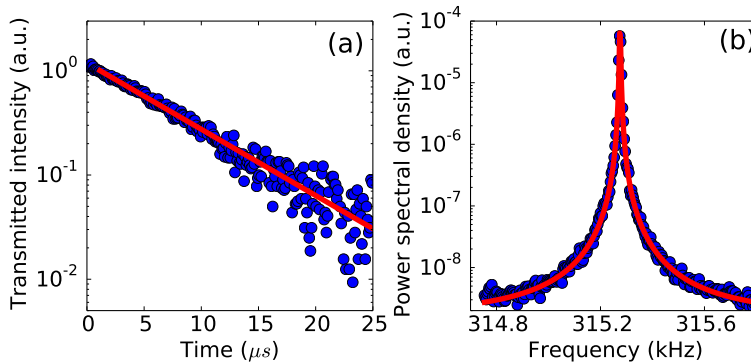


Figure 5.3: Characterization of the optomechanical system. (a) Optical cavity ring-down measurement with an exponential fit. (b) Mechanical thermal noise spectrum at 300K with a Lorentzian fit.

the OPLL, which is directed to a fast PI-controller. By adjusting the frequency of the OPLL LO, laser 2 can be set to a specific cavity detuning.

By using a cavity resonance as frequency reference, any thermal drift is compensated for. The frequency tunable range of the lasers via the piezos is limited to approximately 10 MHz. However, both lasers are also temperature tunable over a broader frequency range (~ 1 GHz), although with < 1 Hz bandwidth. We have therefore implemented a slow temperature feedback loop for each laser that enables us to measure for many hours with a fully automated measurement protocol.

5.3 Results and discussion

First we show the results of the optical and mechanical characterization. This provides information about the mechanical frequency Ω_m , mechanical linewidth Γ_m and optical linewidth κ . From the optical cavity ring-down measurement in Fig. 3(a) we obtain a cavity linewidth κ of $2\pi \times 23.2 \pm 0.1$ kHz, which corresponds to a finesse of 129000. Given the small diameter of the mirror and the multiple clean room fabrication steps it went through, it is remarkable that the optical finesse almost reaches the theoretical maximum of 140000 set by the coating of our Bragg mirrors. For the mechanical characterization, the mechanical thermal noise spectrum is recorded and a Lorentzian is fitted to it, as is shown in Fig. 3(b). From the fit we find $\Gamma_m = 2\pi \times 3.3 \pm 0.14$ Hz, corresponding to a mechanical quality factor of 95000. From the optical and mechanical characterization alone it is clear that our optomechanical system is in the side-band resolved regime with $\Omega_m/\kappa \approx 13.5$. The small linewidth of the optical cavity allows for a large intracavity laser power with only modest input. Since the light is circulating in vacuum, rather than for example silica, secondary effects due to absorption do not play a role, as in [71]. These two ingredients contribute to a large intracavity photon number and therefore also to a large multi-photon cooperativity. We estimate, using the current system parameters, that

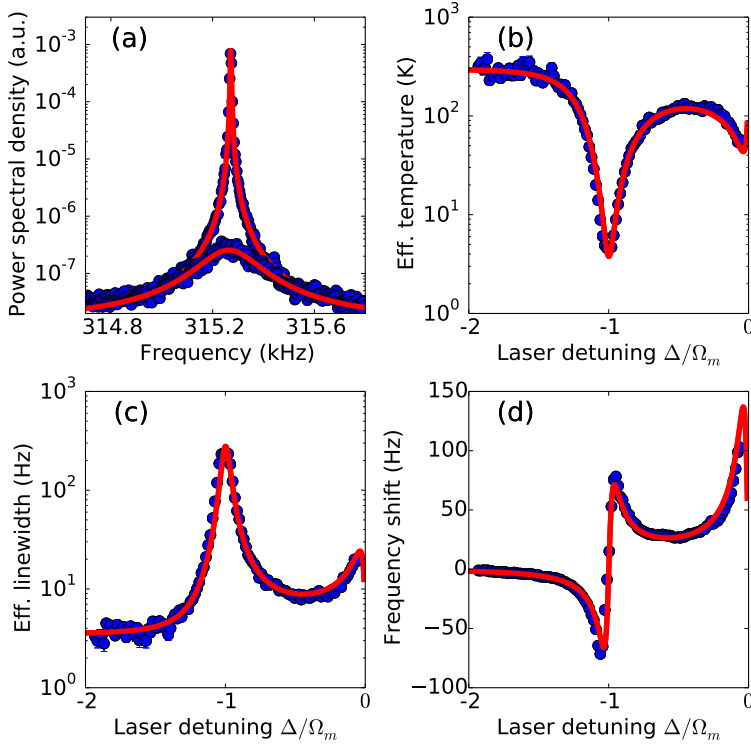


Figure 5.4: Optical side-band cooling. (a) Thermal mechanical noise spectra for $\Delta = \omega_{laser} - \omega_{cav} = -2\Omega_m$ (top curve) and $\Delta = -\Omega_m$ (bottom curve). (b) Effective temperature. (c) Effective linewidth as a result of optical damping. (d) Mechanical frequency shift due to the optical spring effect.

a cooperativity of $10^5 - 10^6$ is possible depending on laser input power.

To demonstrate the “side-band resolvedness” of our system, we perform a side-band cooling experiment. We change the laser detuning of the strong pump beam (laser 2) in small steps of 5 kHz by varying the OPLL LO and measure the mechanical thermal noise spectrum. The laser power of the pump beam is about 50 times higher than the power of the read-out laser. In Fig. 4(a) the mechanical thermal noise spectrum together with a Lorentzian fit is shown for two specific detunings. The top curve shows the spectrum for $\Delta = \omega_{laser} - \omega_{cav} = -2\Omega_m$ and the bottom curve shows the spectrum for $\Delta = -\Omega_m$.

Clearly the linewidth is larger and the integrated area smaller for the bottom mechanical thermal noise spectrum, indicating both damping and cooling. The integrated area can be related to an effective temperature via the equipartition theorem since $\langle x^2 \rangle = \frac{k_B T}{m\Omega_m^2}$. When the pump laser is off, the mechanical resonator is not cooled, so its effective temperature is equal to the environmental temperature of 300 K, assuming good thermalization with the environment. Therefore we set the related integrated area to correspond to an effective temperature of 300 K. When the

pump laser is on, the effective temperature for each specific detuning is obtained by comparing the integrated area of each mechanical thermal noise spectrum to the integrated area of the mechanical thermal noise spectrum at 300 K. The effective optomechanical linewidth Γ_{eff} , which is broadened due to optical damping according to $\Gamma_{eff} = \Gamma_m + \Gamma_{opt}$, and the frequency shift due to the optical spring effect are also obtained from the Lorentzian fit. The results are shown in Fig. 4(b)–4(d) together with a fit according to the equations (see for example [16]):

$$T_{eff} = \frac{\hbar\Omega_m}{k_B} \frac{\bar{n}_{th}\Gamma_m + \bar{n}_{min}\Gamma_{opt}}{\Gamma_m + \Gamma_{opt}}, \quad (5.1)$$

$$\Gamma_{eff} = \Gamma_m + \frac{P_{in}\kappa_{ex}\omega_{cav}}{2L^2m\Omega_m(\Delta^2 + \kappa^2/4)} \left[\frac{\kappa}{(\Delta + \Omega_m)^2 + \kappa^2/4} - \frac{\kappa}{(\Delta - \Omega_m)^2 + \kappa^2/4} \right], \quad (5.2)$$

$$\delta\Omega_m = \frac{P_{in}\kappa_{ex}\omega_{cav}}{2L^2m\Omega_m(\Delta^2 + \kappa^2/4)} \left[\frac{\Delta + \Omega_m}{(\Delta + \Omega_m)^2 + \kappa^2/4} + \frac{\Delta - \Omega_m}{(\Delta - \Omega_m)^2 + \kappa^2/4} \right], \quad (5.3)$$

with $\bar{n}_{min} = \left(\frac{\kappa}{4\Omega_m}\right)^2$ the theoretical minimum phonon number in the side-band resolved regime, P_{in} the input power and κ_{ex} the input coupling loss rate. The fit is done simultaneously for all three curves with only the input power and cavity linewidth as free parameters. The parameters obtained from the fit are $3.07 \pm 0.04 \mu\text{W}$ for the input power of the cooling laser and $2\pi \times 23.7 \pm 2 \text{ kHz}$ for the cavity linewidth.

This value for the cavity linewidth is consistent with the value obtained from the optical cavity ring-down measurement. The excellent agreement between experiment and theory, as indicated by Fig. 4(b)–4(d), and the good match between the two different methods for obtaining the cavity linewidth, shows the level of precision and control we have over the system.

We would like to stress that the sharp features resulting from the optical spring effect in Fig. 4(d) around $\Delta = -\Omega_m$ can only be visible with a high-finesse cavity and a narrow-linewidth laser, in combination with optimal performance of the entire setup and locking schemes. Although two narrow-linewidth lasers are used, excess laser phase noise could easily be introduced by e.g. an improper laser lock, which would blur out any sharp features such as in Fig. 4(d) [74] and could potentially prevent ground state cooling. Observing these sharp features therefore demonstrates the cleanliness of the whole measurement chain consisting of lasers, photodetectors and feedback loops.

Although the goal of this paper is not to demonstrate large optical cooling factors, we are able to cool from room temperature to 4 K using modest laser power, as indicated in Fig. 4(b). By increasing the laser power further, lower effective temperatures are achieved (not shown here). However, to reach the quantum mechanical ground state, the environmental temperature should be lowered significantly by placing the optomechanical cavity in a cryostat. Note that even in a cryogenic environment we can still use relatively high laser powers due to the low absorption of the mirrors. From the experimental parameters presented in this letter, we estimate that a multi-photon cooperativity of more than 10^5 is possible, indicating that a base temperature of 1 K is sufficient for ground state cooling. This is easily achievable in a variety

of cryostats, bringing investigation of quantum to classical transition with low frequency resonators one step closer.

5.4 Conclusion

In this paper we have reported experiments with a high-finesse optomechanical Fabry-Perot cavity. By using high-quality Bragg mirrors for both cavity mirrors, we are able to demonstrate optical side-band cooling of a large mass, low frequency side-band resolved system ($\Omega_m/\kappa \approx 13.5$). By locking a pump laser via an optical phase-locked loop to a probe laser, we are able to achieve \sim kHz resolution laser detuning. Not only do we find a good agreement between the experiment and theory, the obtained value for the cavity linewidth from the optical cooling experiment also matches the value obtained by a separate cavity ring-down measurement. With this we demonstrate the precision of our experiment. By lowering the environmental temperature significantly, optical cooling to the quantum ground state should be possible.

Acknowledgments

The authors would like to thank H. van der Meer for technical assistance. The authors are also grateful for useful discussions with W. Loeffler. This work is part of the research program of the Foundation for Fundamental Research (FOM) and of the NWO VICI research program, which are both part of the Netherlands Organisation for Scientific Research (NWO). This work is also supported by the National Science Foundation Grant No. PHY-1212483.

Optomechanics with a polarization nondegenerate cavity

In the previous chapters, the polarization degree of light was only used to separate different laser frequencies. In this chapter, we show that a polarization nondegenerate cavity can be used to gain access to the polarization degree of freedom in optomechanical experiments. Furthermore, we propose how to use this additional degree of freedom to perform accurate side-band thermometry and to create novel forms of photon-phonon entanglement. The experimental system in this chapter utilizes the compressive force in the mirror attached to a mechanical resonator to create a micromirror with two radii of curvature which leads, when combined with a second mirror, to a significant polarization splitting of the cavity modes.

6.1 Introduction

Coupling mechanical motion to electromagnetic radiation lies at the heart of cavity optomechanics. Because the coupling is so general, a wide variety of experiments exists. For example the scale on which the mechanical motion takes place can range from suspended macroscopic mirrors [75, 76, 77] to cold atoms coupled to an optical cavity [78], see Ref. [16] for a review. Also the source of electromagnetic radiation varies greatly, ranging from the microwave [39, 79] to the optical domain [40, 61, 44, 80]. Each device and set-up has its own advantages. In the optical domain, the availability of the polarization degree of freedom adds an additional knob for controlling and tuning the optomechanical devices. This means that techniques and methods from several landmark experiments demonstrating photon-photon [81, 82] or photon-matter [83, 84] entanglement can be implemented in existing optomechanical set-ups. However, so far, polarization has mostly been used to experimentally separate different optical signals and is not yet considered as a degree of freedom in, e.g., proposals [8, 85, 86, 87, 88] and experiments [89, 90] on photon-phonon entanglement.

This is understandable since the mechanical mode in an optomechanical system is not sensitive to the polarization of the incoming photon. However, the optical mode can be engineered to be polarization sensitive. Birefringence or astigmatism can cause a polarization splitting of the (fundamental) mode of an optical cavity. Although such birefringence has been observed before in optomechanical set-ups, it has been regarded as a parasitic effect [91, 92]. In this article we show an optomechanical system in which a significant polarization splitting of the fundamental mode is present. After a brief characterization of the set-up we show how for a single laser frequency, the interaction can be changed from cooling to driving simply by varying the polarization. Finally, some advantages of a polarization nondegenerate optomechanical system are discussed.

6.2 Experimental details

In a Fabry-Perot-based system birefringence, occurs when one cavity mirror, either the stationary or the movable mirror, has two radii of curvature. We chose to use the curvature already present in the mirror attached to a trampoline resonator. The trampoline resonator consists of multiple DBR layers on top of a patterned silicon nitride membrane (see inset Fig. 6.1a). Finite element analysis using COMSOL shows that the compressive force in the DBR mirror is much larger than the tensile force in the silicon nitride causing the mirror to buckle slightly. This is schematically depicted in Fig. 6.1a. We have confirmed the mirror curvature with an optical profiler. Fig. 6.1b shows a concave mirror surface. Such small high quality curved mirrors are already interesting on their own to make small micro cavities for cavity QED experiments. For a polarization nondegenerate cavity however, an astigmatic mirror is needed.

Closer inspection of the mirror surface reveals a four-fold symmetry for the curvature in the center of the mirror, as expected from the geometry of the trampoline resonator. Because the DBR mirror is over-sized, 110 μm diameter, compared with

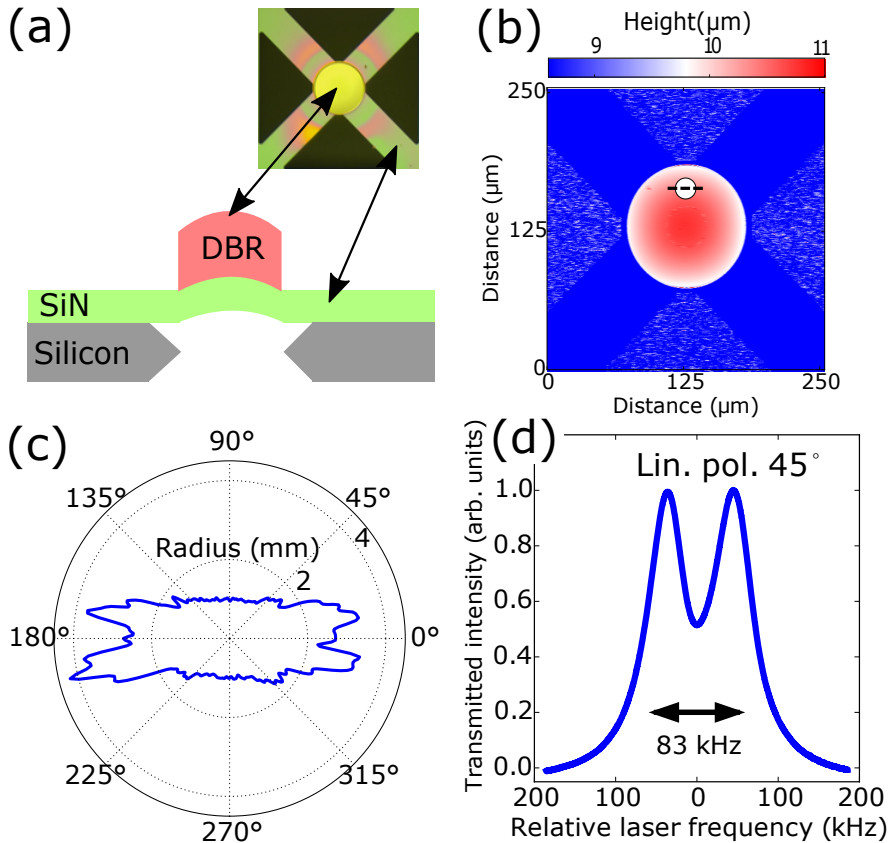


Figure 6.1: (a) Compressive stress in the DBR layers causes the mirror to buckle. Inset shows optical image of the trampoline resonator (b) Optical profiling with a confocal microscope reveals a concave mirror surface. (c) Local radius of curvature as function of angle obtained for the off center location indicated with the white dot in panel (b). (d) Demonstration of mode splitting for an off axis aligned cavity by monitoring the transmitted intensity when the laser frequency is varied.

the beam size, typically 12 μm diameter, a high-quality cavity can still be constructed by placing the beam off axis. It is therefore interesting to look at the local curvature away from the middle. For the white dot in 6.1b we determine the local radius of curvature (ROC) by fitting a parabola to a line-cut straight through the center of the white dot (see dashed line 6.1b). From the derivative of the parabola the ROC is obtained [93]. If we repeat this procedure for linecuts at different angles we obtain Fig. 6.1c. A clear two-fold symmetry is present, with a minimum ROC of about 1 mm and a maximum ROC of about 4 mm. Using these numbers together with the recently published work by Uphoff et al. [94], a polarization splitting of about 60 kHz for the fundamental mode is expected, based on the parameters of the set up.

To demonstrate such a splitting, a 5-cm-long Fabry-Perot cavity operating around 1064 nm is placed in a vibration isolated vacuum chamber. In this configuration the convex side of the trampoline resonator faces the stationary mirror. The fundamental mode of the cavity is aligned such that the cavity mode is located on the side of the small curved mirror. The optical quality factor is constant with respect to beam placement, only near the very edge of the mirror does the optical quality degrade due to clipping of the beam. Both beam placement and optical quality factor are actively monitored during alignment to prevent this clipping of the beam. Via a cavity ringdown [67] the optical linewidth is determined to be 51 ± 1 kHz and the mechanical resonator is characterized by measuring its mechanical thermal noise spectrum with a laser locked to a cavity resonance by using the Pound-Drever-Hall (PDH) technique [38]. With this technique an intrinsic mechanical linewidth Γ_m of 19 Hz and a mechanical frequency Ω_m of 222 kHz is measured.

6.3 Results

To see if any polarization splitting is present, a laser is scanned across the cavity resonance and the input polarization is adjusted to address both polarization modes equally. A polarization splitting of 83 ± 1.0 kHz is observed, as shown in Fig. 6.1d. This is of the same order as the expected polarization splitting of 60 kHz. Furthermore, the splitting is large enough to already show some interesting optomechanical effects. For this the measurement scheme outlined in ref. [67] is used. A probe laser at the cavity resonance is used to monitor the mechanical motion while the detuning of a second pump laser is varied.

For each specific laser detuning we measure the mechanical noise spectrum, fit a Lorentzian and extract the mechanical linewidth and frequency. The results are shown in Fig. 6.2. Note that the laser detuning is indicated for one of the two optical modes. The detuning for the other mode is shifted by 83 kHz, the polarization splitting. Since our optomechanical system operates in the linearized regime, the frequency shift and effective damping can be understood by adding the contributions of both modes:

$$\delta\Omega_{m,total} = \delta\Omega_{m,1} + \delta\Omega_{m,2} \quad (6.1)$$

$$\Gamma_{eff,total} = \Gamma_{opt,1} + \Gamma_{opt,2} + \Gamma_m \quad (6.2)$$

where $\delta\Omega_{m,i}$ and $\Gamma_{opt,i}$ are the optically induced frequency shift and damping (see

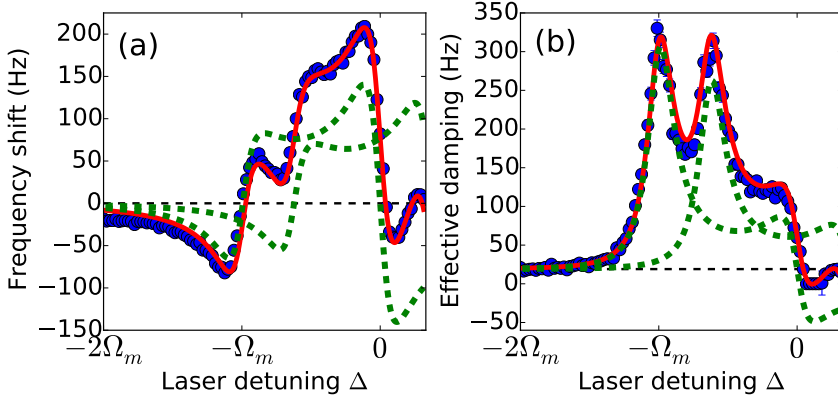


Figure 6.2: (color online) Optomechanical interaction for a polarization nondegenerate cavity. Blue points are extracted from the Lorentzian fit to the mechanical resonance. Red is a simultaneous fit of the data with four free parameters: optical linewidth, optical splitting, and input laser power for both modes. Green shows the contribution of the individual modes. Panel(a) shows the mechanical frequency shift and panel (b) shows effective mechanical damping.

for example ref. [16] for detailed expressions). In green is shown the individual contribution from each mode and in red is shown the result of a fit for the combined effect of both modes. Note that the red curve in Fig. 6.2 and Fig. 6.3 is obtained from a single simultaneous fit to all data with only four free parameters: the optical linewidth, the mode splitting and the input power of both the horizontal and vertical polarization modes. From Fig. 6.2 we see that the experimental results are nicely described by the addition of the two separate contributions. Furthermore we obtain an optical linewidth κ of 52 ± 0.9 kHz, a mode splitting of 82.4 ± 1.2 kHz and an input laser power of 2.19 ± 0.04 μ W and 1.85 ± 0.04 μ W for both optical modes. These results are in good agreement with the optical characterization. It is also clear that at $\Delta = 41.5$ kHz, precisely in between both optical modes, their contributions cancel.

This is even more clear when looking at the effective temperature of the mechanical mode, which is obtained from the area of the Lorentzian fit to the mechanical resonance. The theory curve for Fig. 6.3 is given by

$$T_{eff} = \frac{\hbar\Omega_m \bar{n}_{th}\Gamma_m + \bar{n}_{min}\Gamma_{opt}}{k_B (\Gamma_m + \Gamma_{opt})} \quad (6.3)$$

with $\bar{n}_{min} = (\kappa/4\Omega_m)^2$ the theoretical minimum phonon number in the side-band resolved regime and \bar{n}_{th} the thermal phonon occupation number. For the optical damping Γ_{opt} we use the sum of the contributions from both modes (see Eq. 6.2). From the resulting graph of Fig. 6.3 we see again that the experimental results follow the theory nicely. Furthermore, at laser detuning $\Delta = 41.5$ kHz indicated by the arrow, the effective mode temperature is just the environmental temperature, showing once more that the contribution from both polarization modes cancel out. However, if the laser is kept at $\Delta = 41.5$ kHz and the input polarization is changed,

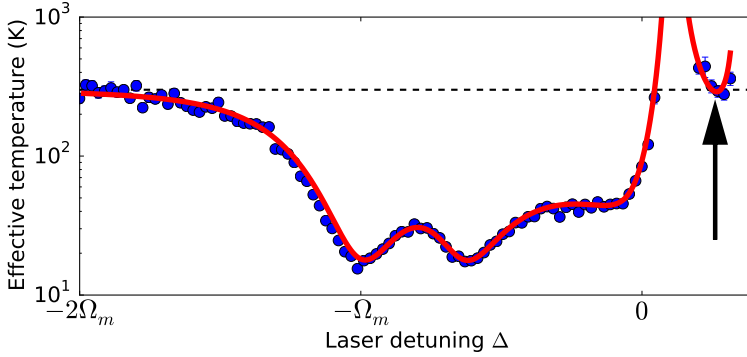


Figure 6.3: (color online) Effective temperature as a function of laser detuning. The arrow indicates the point where the contribution from both modes precisely cancel each other, leading to an effective temperature equal to the bath temperature.

one mode will dominate leading to either heating or cooling.

Of course the same effect can be obtained by using two lasers placed at either side of the cavity resonance, or perhaps even by using higher-order optical modes, but using the polarization degree of freedom as described above has several advantages. Because only a single frequency is used, the whole set-up has one common path, which improves the stability of the experiment. Second, one single narrow linewidth laser frequency is needed. Furthermore, only the fundamental Gaussian transverse mode is required, which has the same optical quality for both polarization modes. Finally, the power ratio between the two modes is easily adjusted simply by rotating the incident polarization.

In principle these advantages are only technical. There are however interesting opportunities when the polarization splitting is precisely two times the mechanical frequency. For example an alternative method for side-band thermometry [71, 73, 95, 96, 97], which is the optomechanical equivalent to Raman-ratio thermometry in cold atoms [98] and solids [99], is possible. In Fig. 6.4 a laser, 45° linearly polarized, is placed precisely in the middle of the two polarization modes. Interaction with the horizontal mode leads to Stokes scattering, while interaction with the vertical mode leads to anti-Stokes scattering. For a large average phonon number $\langle n \rangle$ both the horizontal mode (Stokes sideband) and vertical mode (anti-Stokes sideband) will exit the cavity with equal intensity. However, when the phonon occupation number is lowered, Stokes scattering becomes dominant and the light exiting the cavity will be mainly in the horizontal mode. Therefore the phonon number can be accurately obtained by measuring the ratio of transmitted light in the horizontal and vertical mode, since this will scale as $1 + 1/\langle n \rangle$.

Another interesting opportunity arises when a polarization nondegenerate system is prepared in the quantum-mechanical ground state, a prerequisite for photon-phonon entanglement. Often a beamsplitter is used to create photon-photon entanglement [8, 85, 86, 87, 88]. For a polarization sensitive cavity this is no longer needed. If we again consider the situation of Fig. 6.4, but replace the laser with a

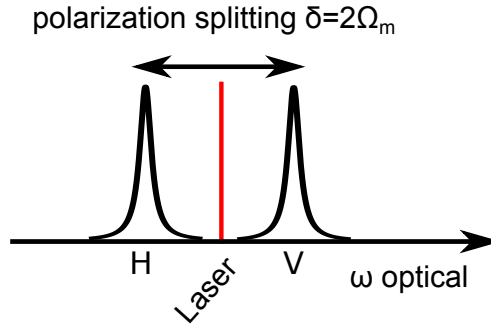


Figure 6.4: A polarization nondegenerate cavity with a splitting $\delta = 2\Omega_m$. H and V denote the different polarization and corresponding cavity mode.

single photon source, we see that entanglement arises when the incoming photon, 45° linearly polarized, is projected onto either basis state. By projecting onto the horizontal basis state, a phonon will be added to the mechanical resonator, while projecting onto the vertical basis state will extract a phonon. When, for example, starting from the $\langle n \rangle = 1$ state, the mechanical resonator is put into a superposition between the ground state and the second-excited state. This is not possible when a beamsplitter is used together with multiple laser frequencies. The addition of the polarization degree of freedom has created a new possibility to manipulate the state of the mechanical resonator. Furthermore, additional tools from the polarization-quantum optics toolbox can now be used. The input photon can be replaced with polarization entangled photon pairs, where one photon interacts with the resonator while the state of the other photon is monitored. We must however remark that for such single photon experiments either single photon strong coupling is required or a postselection method has to be implemented [14].

To access this new and interesting regime, a system with a polarization splitting of two times the mechanical frequency is needed. This requires only a small modification to the system presented here. Fabry-Perot-based optomechanical systems are available with an optical linewidth smaller than 17 kHz, a mechanical frequency of 250 kHz, and a mechanical quality factor approaching 5×10^5 [35]. Taking this as a starting point, a cavity with a mode splitting of 500 kHz is needed. With some small modifications to the trampoline resonator design the mode splitting can be pushed from 83 to about 100 kHz. Since the mode splitting scales inversely with cavity length [94], reducing the cavity length by a factor of five results in the desired mode-splitting. This will also increase the optomechanical coupling strength g_0 to about $2\pi \times 8$ rad/s. A downside to this method is that the cavity linewidth increases by a factor of five, but an optical linewidth of 85 kHz is still sufficient to be side-band resolved. More importantly, to achieve ground-state cooling, the multiphoton cooperativity should be much larger than the thermal occupation number. In this case a base temperature of 1 K together with a laser power of $50 \mu\text{W}$ is needed, which is experimentally feasible.

6.4 Conclusion

In conclusion, we have shown how a polarization nondegenerate optomechanical system can be a valuable addition to the existing optomechanical toolbox. We have created a system where optomechanical interaction with a single frequency laser can be tuned from cooling to heating simply by varying the incident polarization. On its own this offers some technical advantages but, combined with an optomechanical system close to the quantum ground state, this leads to new possibilities for photon - phonon entanglement. We have demonstrated how such a system can be fabricated and showed that the last remaining step is to decrease the length to bring the presented system into the target regime.

Acknowledgments

The authors acknowledge useful discussions with W. Loeffler. The authors would also like to thank H. van der Meer for technical assistance and support.

Intermezzo: picking up not-so-good vibrations

7.1 The issue of vibrations

In the previous chapters, optical side-band cooling was successfully used to cool the mechanical motion of a trampoline resonator. For example, in chapter 5 an effective temperature of 4 K is reached. Of course an even lower temperature is possible when more laser power is used. In Fig. 7.1 the mechanical power spectrum of a single trampoline resonator optically cooled to 300 mK is shown. It is clear that only with some imagination a Lorentzian (red line) is present in the data. Because our detection method relies on a clean Lorentzian signal, this clearly poses a problem. This chapter is devoted to finding the origin of the vibrations seen in Fig. 7.1. Two major candidates are discussed: up-conversion of low frequency vibrations and vibrations coming from the sample itself. The low frequency vibrations are investigated using a full numerical simulation, while the sample itself is investigated by measuring resonators with different frequencies and varying the clamping method.

7.2 Low frequency vibrations

7.2.1 Introduction

It might seem strange that low frequency (0-5 kHz) vibrations can have an effect at frequencies above 300 kHz. The optomechanical interaction, however, is parametric in nature, as is shown in chapter 3. Low frequency cavity displacements mix with the motion of the trampoline resonator to create new frequency components at sum and difference frequencies. This becomes quite involved when multiple frequency components are present, as we will show later.

In principle low frequency motion of the cavity length (or laser frequency) should not be an issue, since the laser is locked directly to the cavity resonance. If, however, the feedback is not done properly or the signals to compensate are simply too big, this could cause the vibrations visible in Fig. 7.1. To fully understand the experimen-

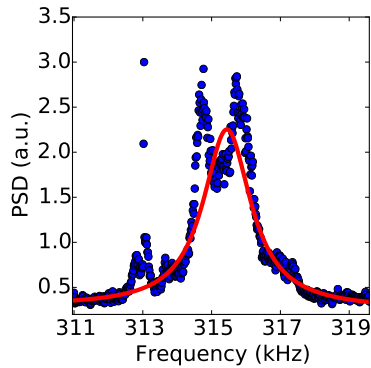


Figure 7.1: Mechanical power spectrum of a single trampoline resonator optically cooled to 300 mK.

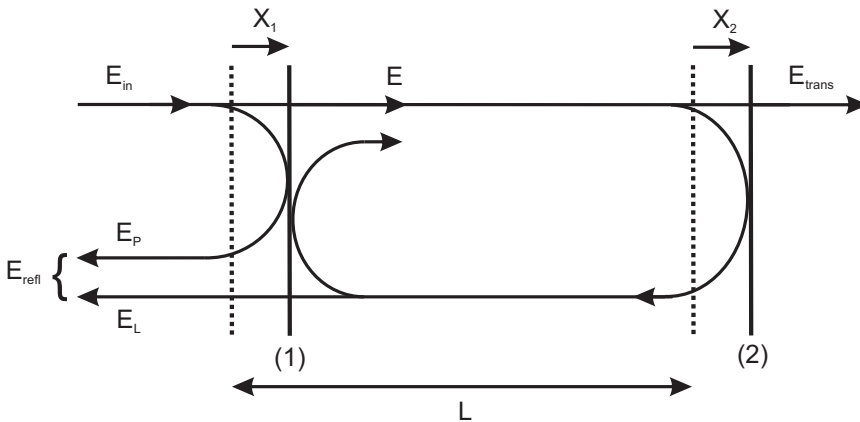


Figure 7.2: The field inside a Fabry-Perot cavity.

tal set-up, a computational platform where the laser detuning or cavity length can be varied together with a read-out of the mirror motion in accordance with experiment is needed. The next sections outline the computational steps required to fully model the experiment.

7.2.2 Theory

Definitions

The field inside a Fabry-Perot cavity at any time is given by the fields already present inside the cavity ¹, the input field and the output field. The magnitude of the fields and the corresponding phase evolution of the fields can best be solved by discretizing the time in units of the round trip time $2T$, where T is the time it takes for the

¹When referring to the field, the electrical field E is meant

field to travel the length L of the cavity.

To find the equations for all the relevant fields, we consider the situation as depicted in Fig. 7.2. The incoming field E_{in} is partially transmitted through mirror 1 and added to the already existing field to form the intracavity field E . The transmitted field is then a fraction of this intracavity field E , while the reflected field consists of two components, the promptly reflected field E_p and the leakage field from the cavity E_L . Finally, the cavity length can vary due to the displacements of mirrors 1 and 2. The distance between the two mirrors is defined using the length of the cavity and the displacement of both mirrors:

$$d(t) = L + X_2(t - T) - X_1(t) = L + \chi(t) \quad (7.1)$$

where we have taken into account the time delay of the field for traveling a distance L . Note that this time delay is negligible for short cavities, while for long cavities, such as LIGO, this time delay is significant.

With these ingredients, equations for the reflected and transmitted fields as well as the fields at mirrors 1 and 2 can be derived. The field inside the cavity at mirror 1 is given by²

$$E_1(t) = t_1 E_{in}(t) + r_1 r_2 \exp[-2ikd(t)] E(t - 2T) \quad (7.2)$$

with t_1 the transmission coefficient of the first mirror, r_1 (r_2) the reflection coefficient of mirror 1 (2) and k the wave-vector, $\frac{2\pi}{\lambda}$, with λ the wavelength. The field at mirror 2 can now be expressed as follows:

$$E_2(t) = \exp[-ikd(t)] E_1(t - T). \quad (7.3)$$

The transmitted and reflected fields can be expressed similarly. This does require a reference plane to define the phase of the propagating field. Suppose the reference plane of the transmitted field is located a distance x after mirror 2. Similarly, the reference plane for the reflected field is located a distance x in front of mirror 1. It is now convenient to choose this distance x such that the phase factor $\exp(ikx)$ for traveling to the reference plane is 1. If this is assumed, the transmitted and reflected fields are the following:

$$E_{trans}(t) = t_2 \exp[-ikd(t)] E_1(t - T) \quad (7.4)$$

and

$$E_{refl} = \exp[-2ikX_1(t)] [r_1 E_{in}(t) - t_1 r_2 \exp[-2ikd(t)] E_1(t - 2T)]. \quad (7.5)$$

Note that the component of the promptly reflected field, the first term in Eq. (7.5), has a positive sign, because the reflection occurs within the substrate of the mirror. Finally the input field $E_{in}(t)$ itself can have a certain phase ϕ . To account for this, the input field can be written as

$$E_{in}(t) = A \exp(i\phi) = A \exp(i\omega_L t) \quad (7.6)$$

with ω_L the laser frequency.

²Via the reflection coefficients r_1 in r_2 we account for the field leaving the cavity via mirror 1 and mirror 2.

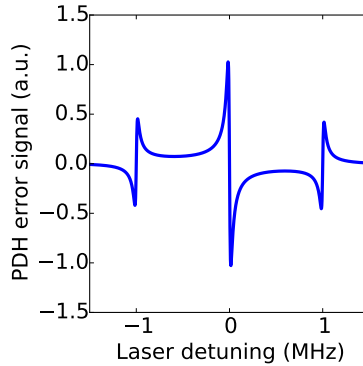


Figure 7.3: PDH error signal generated with the sum-over-round trips method.

Equations (7.1)-(7.5) have a recursive relationship between them, making them numerically solvable. To aid the computation, the cavity length and input laser frequency are chosen such that the phase factor $\exp[-ikd(t)]$ reduces to $\exp[-ik\chi(t)]$. In other words, we choose a frame rotating with the unperturbed cavity resonance frequency ω_{cav} . In this way, the earlier introduced laser frequency ω_L is relative to this unperturbed cavity resonance frequency.

Although the recursive Eqs.(7.1)-(7.5) can be solved for each consecutive round trip, this is not practical for short cavities. For example, for a 5 cm cavity, the round trip time is about 0.32 ns. If no processes occur on these timescales, lumping several round trips together will not significantly alter the end result. As we will see later, for our optomechanical setup the fastest process is the motion of the mechanical resonator, typically on the μs time scale, which makes this approximation justified.

Example: generating a Pound-Drever-Hall error signal

As an example, we can generate a PDH error signal and use this signal to detect the motion of one of the mirrors. The PDH method relies on a phase modulated beam reflecting off the cavity which is subsequently detected, demodulated and low-pass filtered (for details see Ref. [38]). From Eq. (7.6) it is clear that phase modulation of the input field is easy, by choosing ϕ as the following, $\phi = A_0 \cos \omega_M t + \omega_L t$, where we have introduced a modulation frequency ω_M and modulation depth A_0 . By varying the laser detuning ω_L , the typical PDH error signal can be retrieved, as is shown in Fig. 7.3. This error signal is generated for a cavity with a linewidth of 28 kHz, a modulation frequency of 1 MHz and a time-step of $416 \times 2T$ to speed up the calculation.

Now that the PDH method is verified, we can make the end mirror oscillate and detect this motion. A periodic oscillation with an amplitude of 3 pm and a frequency of 75 kHz is applied to the end mirror. Fig. 7.4 shows the results of the PDH error signal as well as an FFT of the same error signal. The small oscillations visible in the PDH error signal are due to the remaining 2 MHz component, twice the modulation frequency, still present after filtering.

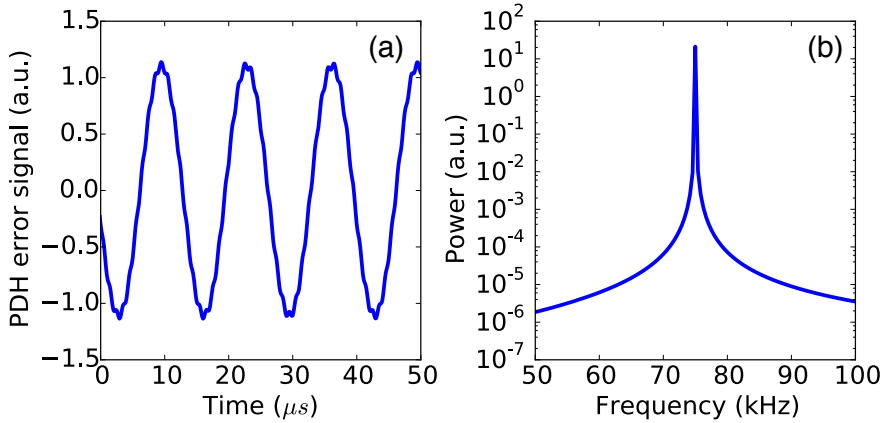


Figure 7.4: Detection of small mirror oscillations via the PDH method. (a) PDH error signal as function of time. (b) FFT of the error signal.

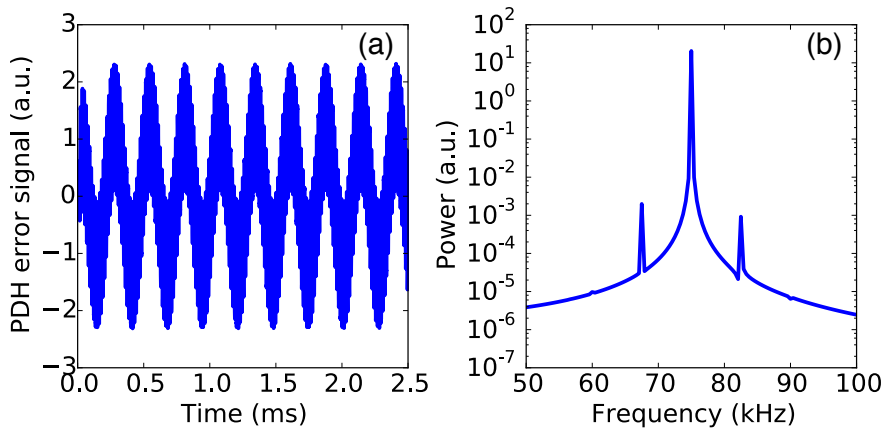


Figure 7.5: Detection of small mirror oscillations via PDH method. Compared to Fig. 7.4 a second component at 3.75 kHz is added. (a) PDH error signal as function of time. (b) FFT of the error signal.

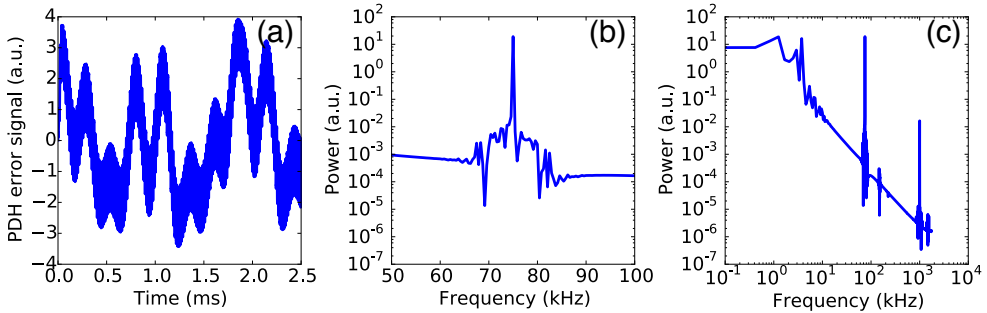


Figure 7.6: The effect of multiple unwanted oscillations in cavity length on the read-out of a movable mirror. (a) PDH error signal as function of time. (b) FFT of the error signal around the simulated mechanical resonance. (c) Same as (b) but showing the entire frequency scale.

Finally, the effect of mechanical vibrations can be simulated by adding an additional oscillation of the cavity length, in this case a displacement of 500 fm at a frequency of 3.75 kHz. The results are shown in Fig. 7.5. Although a low frequency oscillation is added, it also shows up as sidebands of the 75 kHz resonance in the FFT. Since a moving mirror in a cavity applies a phase modulation to the cavity field, for all frequency components present, the frequency component of 75 kHz in the optical field will have a 3.75 kHz modulation, resulting in the two sidebands.

When more low frequency components are present, this is no longer clear. In Fig. 7.6 three more unwanted oscillations of similar magnitude and frequency are added. Compared to Fig. 7.5 the noise floor has risen drastically due to the tails of the low frequency oscillations as can be seen in Fig. 7.6(c). Furthermore, a noise band around the frequency of interest starts to appear, making the individual sidebands no longer distinguishable.

7.2.3 Combining with optomechanical interaction

Until now only the read-out of a forced driven oscillation is considered, while in an optomechanical set-up the motion of the mirror is generated via thermal excitation and, depending on the laser detuning, the interaction with the cavity field. This interaction might be influenced when additional phase modulation of the cavity field occurs. To investigate this effect, the interaction with the movable mirror is taken into account as well. The mirror can be modeled as a harmonic oscillator with an additional force due to the radiation pressure:

$$\frac{d^2x(t)}{dt^2} = -\Gamma_m \frac{dx(t)}{dt} - \Omega_m^2 x(t) + \frac{2}{\pi mc} |E_2(t)|^2 + \eta(t) \quad (7.7)$$

with $x(t)$ the position of the mirror, Γ_m the mechanical damping rate in rad/s, Ω_m the mechanical frequency in rad/s, m the mass of the resonator in kg, c the speed of light and $\eta(t)$ the noise term that generates the mirror's thermal state, with $\langle \eta_i(t) \eta_j(t') \rangle = \frac{2}{m} \Gamma_m k_b T \delta_{i,j} \delta(t - t')$.

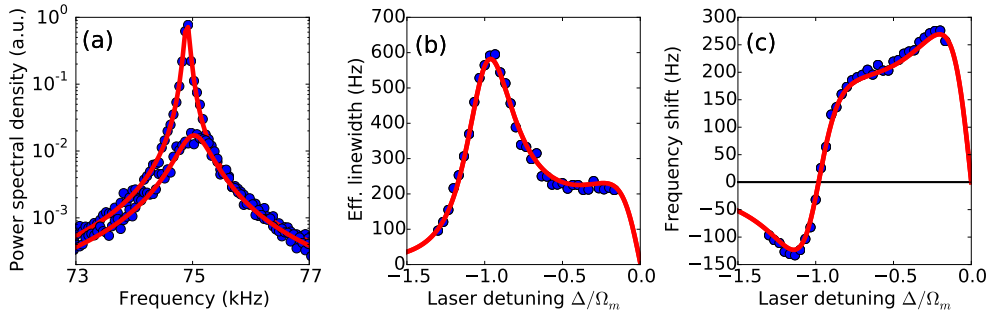


Figure 7.7: Full simulation of the optomechanical interaction. (a) Power spectra recorded via the PDH method for two different detunings. Red line is Lorentzian fit to extract the effective linewidth and center frequency. (b) and (c) show the effective linewidth and frequency shift for different laser detunings. The red lines is the expected trend from theory, based on the input parameters of the simulation.

To solve Eq. (7.7) together with the solution for the cavity field given by Eqs. (7.1) - (7.6), a modified 4th-5th order Runge-Kutta method is implemented. In this approach, the value of the cavity field and mirror position one time-step, h , further is calculated using approximated midpoint solutions and weighting them appropriately. For the approximate solution of $x(t)$ we can compute the resulting cavity field $E_2(t)$ and use this to calculate the effect on the mirror in the next approximated solution. After one round of calculations, when the next point of $x(t)$ is known, the final cavity field $E_2(t)$ is calculated.

To demonstrate the validity of this approach, we can simulate the read-out of the mirror motion with a weak probe laser via the PDH method introduced in the previous section, while the laser detuning of a second laser is varied. This model describes the experiment performed in chapter 5. The effect of the probe laser on the mirror is neglected for now, since the power of the probe laser is weak (50 nW compared to $1.3 \mu\text{W}$ for the cooling laser) and the probe laser is set at zero detuning, where the net optomechanical interaction is zero. Fig. 7.7 shows the result for a system at 300K with a mechanical frequency of 75 kHz, a mechanical Q-factor of 1×10^5 and an optical linewidth of 28.8 kHz. In Fig. 7.7(a) two power spectra are shown for different detunings, together with a Lorentzian fit. From this fit critical parameters such as effective linewidth and resonator frequency are extracted. Fig. 7.7(b) and 7.7(c) show the effective linewidth and resonator frequency shift for different laser detunings. The red line is the theory based on the input parameters of the simulation. An excellent agreement between simulation and theory validates our approach. Furthermore, the agreement between theory and simulation justifies the assumptions and simplifications made, such as the combination of multiple round trips into a single step.

We can now repeat the investigation of low frequency cavity vibrations on the read-out of the mechanical resonator. For this we introduce four low frequency cavity length oscillations, precisely the same as in Fig. 7.6, to generate vibrations in the

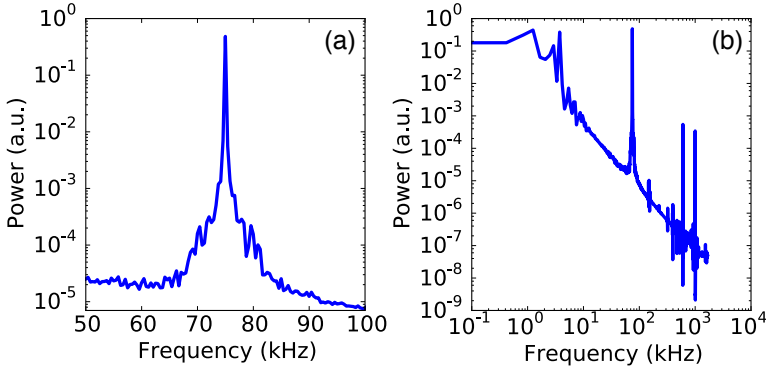


Figure 7.8: The effect of low frequency vibrations on the read-out of a moving mirror in an optomechanical system. (a) Power spectrum of simulated mechanical resonance. (b) Power spectrum showing the entire window.

cavity field. Figure 7.8(a) shows the mechanical resonance at 75 kHz, accompanied by additional features. Clearly the mechanical power spectrum can no longer be described by a Lorentzian. Figure 7.8(b) shows that the vibrations are also present in the low frequency part of the FFT of the PDH error signal. As with Fig. 7.6, the presence of the low frequency vibrations will also raise the noise floor in region of the mechanical resonance of interest.

7.2.4 Comparison with experiment

Fig. 7.8 shows that low frequency vibrations, via upconversion, can definitely cause the features visible in Fig. 7.1. However, any change in cavity length can be compensated for by adjusting the laser frequency to maintain the resonance condition:

$$\frac{\omega_L}{\omega_{cav}} = -\frac{\chi(t)}{L}. \quad (7.8)$$

Even partial compensation via the laser frequency should reduce the effect of low frequency vibrations, which in turn should change the vibrations visible around the mechanical resonance. In practice however, varying the PID settings of the laser lock does not change the observed mechanical displacement spectrum at all. Therefore low frequency vibrations are ruled out as the origin of the additional peaks seen in Fig 7.1. The important thing to remember, however, is that the system is extremely sensitive to low frequency lengths changes.

7.2.5 High-Q metals at low temperatures

Varying of the PID settings did not change the observed mechanical displacement spectrum, suggesting that low frequency vibrations are currently not an issue. Looking ahead, the entire optical set-up will operate at cryogenic temperatures inside a

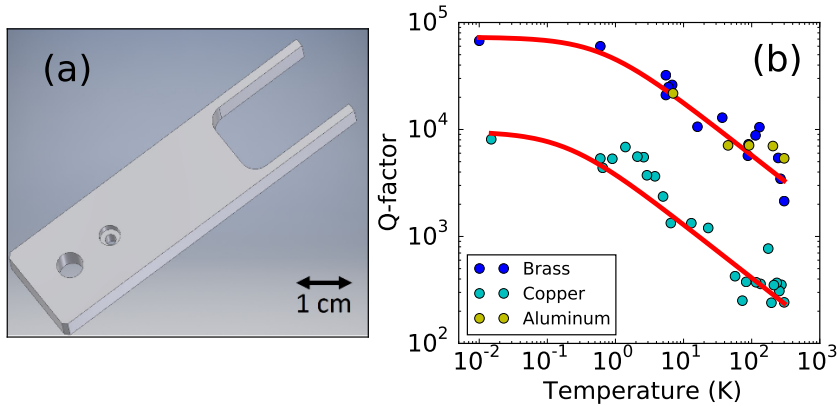


Figure 7.9: (a) Design of the metal tuning fork. (b) Q-factor as function of temperature for different metal tuning forks. The red line shows a fit of $Q \sim 1/\sqrt{T}$

cryostat cooled by a pulse tube cryocooler. Such cryocoolers are a source of low frequency vibrations which can easily excite mechanical modes of the optical set-up itself. Furthermore, at low temperatures the Q-factor of these mechanical modes can be drastically higher than at room temperature, leading to a larger amplitude of the mechanical modes.

To get a feel for this increase in Q-factor, several metal tuning forks are made with a frequency around 2 kHz, see Fig. 7.9(a). The Q-factor is obtained by driving the fundamental mode of the tuning fork with a piezoelectric element attached to the tuning fork and monitoring its motion via a fiber interferometer [100]. Alternatively, a mechanical ringdown is performed when the Q-factor is high (above 10000). Different metal tuning forks are mounted on the mixing chamber of a dilution refrigerator to measure the Q-factor as function of temperature. The results are shown in Fig. 7.9(b), together with a fit using $Q \sim 1/\sqrt{T}$.

Not surprisingly does the Q-factor increases when the temperature is lowered. What is interesting is that all three tuning forks seem to follow the same trend: $Q \sim 1/\sqrt{T}$. The only tentative explanation we have so far for this relation is the following: the displacement of a harmonic oscillator, such as lattice vibrations in metals, scales with \sqrt{T} . If the mechanical dissipation in metals depend on the amplitude of the lattice vibrations, this would explain the relationship $Q \sim 1/\sqrt{T}$. Of course, this hypothesis does require more measurements.

On a more practical note: the Q-factor of the brass tuning fork increased from 5000 at room temperature to 75000 at cryogenic temperatures. This suggests it is not unlikely that when the optical set-up, made of brass, functions perfectly at room temperature, at low temperatures vibrations can become an issue. Therefore, performing measurements at low temperatures does require a cryogenic compatible vibration isolation preferably together with a low-Q set-up. In chapter 10 we will discuss the vibration isolation in more detail.

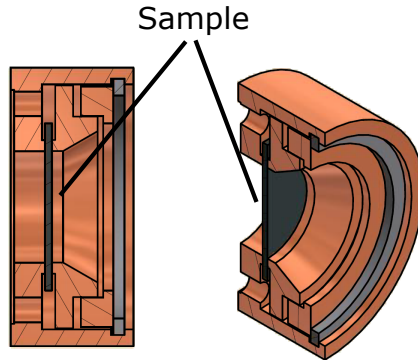


Figure 7.10: The sample holder. The sample, a silicon chip, is clamped down by two gold coated copper rings held in place by a wave spring washer.

7.3 Noise from sample

Another candidate for the mechanical vibration peaks visible in Fig. 7.1 are modes of the sample itself. Sixteen trampoline resonators reside on a single silicon chip approximately 15×15 mm. The chip itself is clamped down by two gold coated copper rings held in place by a wave spring washer, see Fig. 7.10. A back-of-the-envelope calculation shows that a clamped silicon wafer of this size has modes between 100 and 500 kHz [101]. Because the wafer also contains square holes with trampoline resonators, the number of modes can become more complex. It is therefore likely we should pick-up some of these modes.

As a first step to investigate this, a single sample was remounted several times leading to a change in resonance frequency, as well as mechanical quality factor (Q-factor). This already is a good indicator that the clamping of the wafer is an issue. However, the mechanical spectrum remains noisy. As a next step, the method of clamping was varied. The clamping force was increased and one copper rings was interchanged for a ring made of Vespel. Again, changes in resonance frequency and Q-factor were observed, but no reduction in the number of peaks.

To potentially reduce the number of modes present on the wafer, single trampoline resonators on a chip were fabricated. Because silicon nitride with a lower stress was used, the mechanical frequency was reduced from ~ 300 kHz to around ~ 80 kHz. Both the change in geometry and frequency did not resolve the issue of the additional mechanical peaks.

The wafers used to fabricate the samples are super polished silicon wafers. Therefore, the surface is truly flat. The rings used to clamp down the sample can never be made flat with the same precision. To ensure a good contact between the rings and sample, two sheets of indium foil, $30 \mu\text{m}$ thick, were placed on either side of the sample. When clamping down the sample, the indium will yield, ensuring a good mechanical contact. The resulting mechanical power spectra are shown in Fig. 7.11.

In the left panel of Fig. 7.11 the mechanical power spectra are shown for the sam-

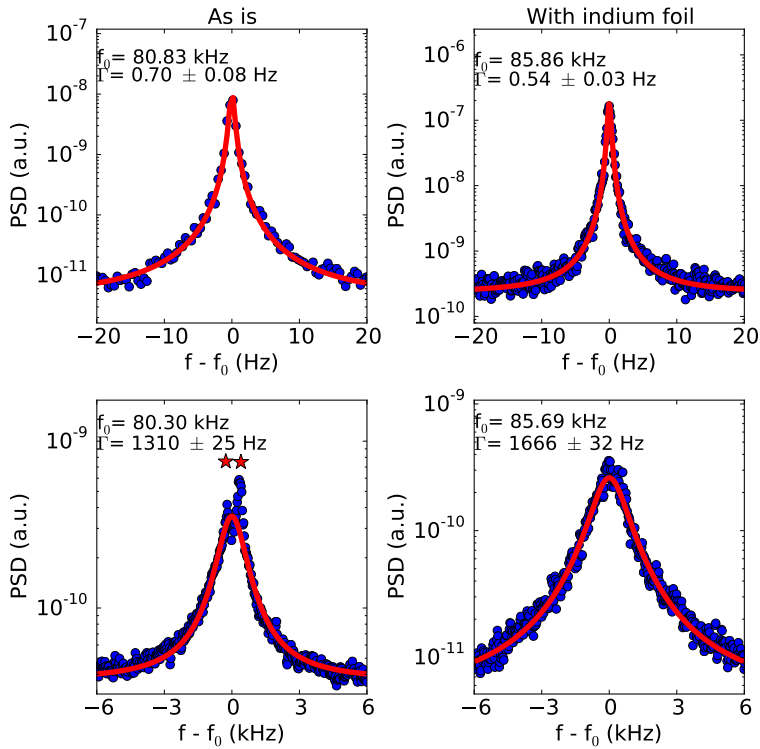


Figure 7.11: Mechanical power spectra of the same sample before and after clamping down using indium foil. The bottom panels compares the two cases with strong optical cooling. The sample without indium shows two additional peaks indicated with red stars.

ple clamped without indium. The bottom left panel shows the Lorentzian resonance and two additional mechanical peaks, when a strong cooling beam is present. If the same sample is clamped down between indium foil, several things happen. Not only has the resonance frequency increased significantly, but also the Q-factor has increased.³ Furthermore, when now a strong cooling beam is applied, the spectrum remains completely clean, as can be seen in the bottom right panel of Fig. 7.11.

Indium is of course not the best choice to use, because it becomes superconducting below 3.4 K resulting in poor thermal conductivity. Also, the process of placing the indium is prone to errors. A better alternative would be to isolate the trampoline resonator from the remaining part of the chip. One way would be to place a phononic bandgap shield around the resonator [102, 103]. For our type of resonators, with a frequency between 100 - 300 kHz, this leads to a significantly larger chip size and is therefore not ideal. Instead, we have chosen to surround the resonator with a second, larger trampoline resonator. This outer resonator with a frequency of 2 - 4 kHz, acts as a mechanical low-pass filter.

We have demonstrated (see Weaver et al. [35]) that such a system provides at least 60 dB of isolation. But more importantly, the mechanical properties are now independent of the method of mounting. In the next chapter we will show that the mechanical power spectrum is clean, consisting only of the Lorentzian resonance of interest.

³Remember: $Q = f_0/\Gamma$

Optomechanical cooling with a nested resonator

In this chapter we show that the nested resonator design can successfully be used for optical side-band cooling. Starting from room temperature we reach an effective mode temperature of 23 ± 5 mK for a 240 kHz resonator. Careful analysis shows that the cooling limit is set by the intrinsic instability of optomechanics using a nested resonator. Although the inner and outer resonator frequencies are far apart, 240 kHz and 2.4 kHz respectively, they remain coupled as they are physically attached to each other. Therefore, the interaction of the inner resonator with the cavity field causes a large optical spring effect for the mechanical motion of the outer resonator. This can lead to a negative effective spring constant, resulting in an anti-stable mechanical system. We analyze the parameter regime where this effect occurs and discuss the consequences and possibilities for future experiments.

8.1 Introduction

Preparing a macroscopic harmonic oscillator close to its quantum mechanical ground state by means of radiation pressure cooling is one of the first steps required to perform new and interesting experiments in the field of cavity optomechanics [69, 71, 104, 41, 58]. Recently, several groups have demonstrated ground state cooling for a variety of systems [40, 39]. Furthermore, several experiments have been performed in which a mechanical oscillator was prepared in a non-classical state [90, 105, 106, 89, 46]. Another interesting prospect is the use of an optomechanical set-up to investigate the possibility of gravitational decoherence [43, 107, 8]. For this particular purpose a relatively large mass, low frequency resonator is needed together with a high quality optical cavity. These requirements make both active feedback cooling and sideband cooling have their challenges, as we will discuss below.

Active feedback cooling uses the real-time displacement of the mechanical resonator to apply a suitable feedback signal to an actuator (mechanical, optical or electrical) [108, 109, 110, 111, 112, 113]. Increasing the gain of the feedback loop results in more feedback cooling up to the point where the amplified read-out noise causes the mechanical motion to increase. This can lead to noise squashing when the mechanical displacement is monitored inside the feedback loop (in-loop measurement) [114]. To reach the quantum mechanical ground state, the initial intrinsic mechanical quality factor must be sufficiently high and the read-out sensitivity must be able to resolve the mechanical zero-point motion [30]. Recently, active feedback cooling close to the mechanical ground state has been realized in a system with read-out sensitivity significantly lower than the zero-point motion [115, 116]. Since the zero-point motion scales inversely with mass and frequency, active feedback cooling with a large mass, low frequency resonator is challenging.

We therefore opt to use optical side-band cooling instead, although this method also has its demanding requirements [117, 20]. The quality of the optical cavity must be such that the cavity linewidth κ is significantly smaller than the mechanical frequency (side-band resolved). For a free-space Fabry-Perot cavity this requires a high quality coating on both the stationary mirror and the moving end-mirror. Furthermore, the mechanical damping rate Γ_m must be small as well. This is summarized as follows: when the multi-photon cooperativity C is significantly larger than the mean phonon number of the environment, n_{th} , ground state cooling is possible. The multi-photon cooperativity C is related to experimental parameters by $C = 4g_0^2\bar{n}_{cav}/(\kappa\Gamma_m)$ with $g_0 = (\omega_{cav}/L)\sqrt{\hbar/2m\Omega_m}$ the optomechanical single-photon coupling rate, ω_{cav} the cavity resonance frequency, Ω_m the mechanical resonance frequency, L the cavity length, m the mode mass and \bar{n}_{cav} the mean cavity photon number.

Recently we have shown that achieving both a small cavity linewidth and small mechanical linewidth (high Q-factor) is possible using a high quality distributed Bragg reflector (DBR) mirror together with a nested trampoline resonator design [35]. In this chapter we will demonstrate the possibilities and features of such a system. First, we demonstrate optical side-band cooling, reaching an effective temperature of 23 ± 5 mK starting from room temperature (cooling factor of 12700). Next,

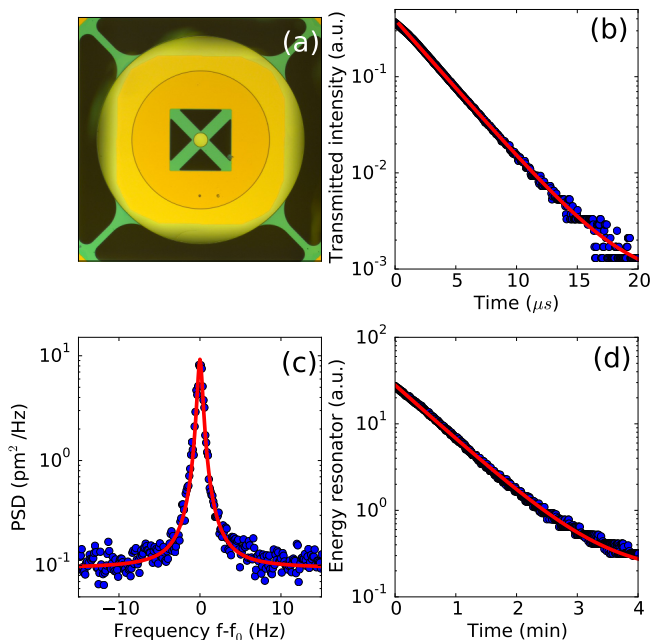


Figure 8.1: (a) Optical microscope image of the nested resonator. (b) An optical ringdown is used to obtain the cavity linewidth κ . (c) Mechanical thermal noise spectrum of the inner resonator. A mechanical quality factor of 387000 is derived from the Lorentzian fit. (d) Mechanical ringdown of the outer resonator. A quality factor of 630000 is derived from the exponential fit.

we present and discuss a model of the nested trampoline resonator to complement the results of the optical cooling experiment. Finally, we discuss the possibilities for future experiments using this design.

8.2 Optical cooling

To demonstrate optical side-band cooling with a nested resonator, we constructed a 5 cm long Fabry-Perot cavity operating around 1064 nm. The whole set-up is placed in a vibration isolated vacuum chamber and kept at a pressure below 1×10^{-5} mbar to eliminate the effect of gas damping on the mechanical properties of the resonator. Fig. 8.1(a) shows an optical microscope image of the nested resonator. An 80 micrometer diameter DBR mirror is suspended from four silicon nitride arms. This structure is surrounded by a large silicon mass suspended again from silicon nitride arms. The outer resonator acts as a mechanical low-pass filter, providing at least 60 dB of isolation for the mechanical motion of the inner resonator around its resonance frequency [35]. The inner resonator has a resonance frequency of 240 kHz and a mode mass of approximately 170×10^{-12} kg (determined via COMSOL). The outer

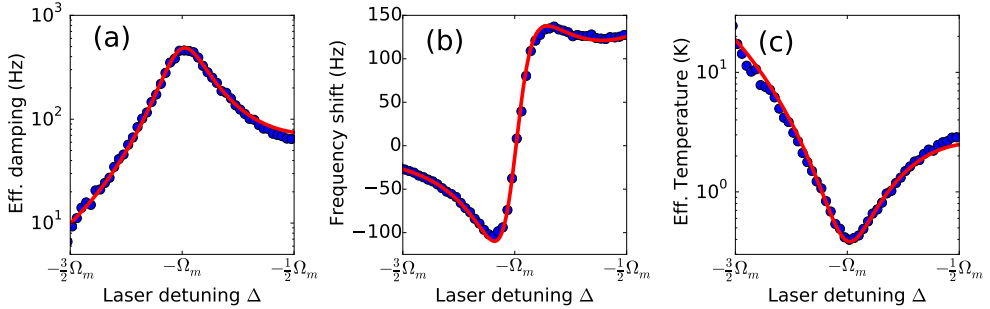


Figure 8.2: The blue datapoints are obtained via a Lorentzian fit to the mechanical power spectra obtained from the PDH probe signal. The effective temperature is obtained from the integrated displacement power spectral density. The red curves are the result of a simultaneous fit to all three data-sets with only the optical linewidth and input power as free parameters.

resonator has a resonance frequency of 2.4 kHz with a mode mass of approximately 1×10^{-7} kg (determined via COMSOL).

For characterization, important optical and mechanical properties are determined via independent measurements. The optical quality of the cavity is determined via a cavity ringdown, as shown in Fig. 8.1(b). We find a cavity linewidth of 53 ± 1 kHz. To determine the mechanical linewidth of both the inner and outer resonator, we use a laser frequency for which the DBR reflection is low (980 nm) and use a side-of-fringe lock (see Section 2.1.3) to measure the thermal motion of the mirror. Fig. 8.1(c) shows a measurement of the mechanical thermal noise spectrum of the inner resonator. From the Lorentzian fit a mechanical linewidth Γ_m of 0.62 ± 0.03 Hz (Q-factor of 387000) is obtained. Note how clean this spectrum is by virtue of the nested system [35]. To determine the linewidth of the outer resonator a mechanical ringdown is used. The result is shown in Fig. 8.1(d). The lifetime obtained from an exponential fit gives a mechanical linewidth of 3.8 ± 0.05 mHz (Q-factor of 630000).

The sideband-cooling experiment is carried out as follows (see chapter 5 for a more detailed description): a probe laser is kept close to the cavity resonance¹ via the Pound-Drever-Hall method [38]. The low power of the probe beam and the fact that at zero detuning no optomechanical effects occur ensures that the effects of the probe beam on the mechanical properties are minimal. A second pump laser is linked to the probe laser one free spectral range away via an optical phase locked loop. With this, the frequency difference between pump and probe laser can be set. For each specific laser detuning we measure the mechanical noise spectrum via the PDH error signal, fit a Lorentzian and extract the mechanical linewidth and frequency. The effective temperature is proportional to the total integrated area of the Lorentzian fit via the equipartition theorem since $\langle x^2 \rangle = \frac{k_B T}{m \Omega_m^2}$.

Via a relative calibration an absolute value for the effective temperature is obtained. When the pump laser is off, the resonator is assumed to be in thermal equi-

¹To keep the system stable, the probe laser is slightly blue detuned as we will explain in the next section.

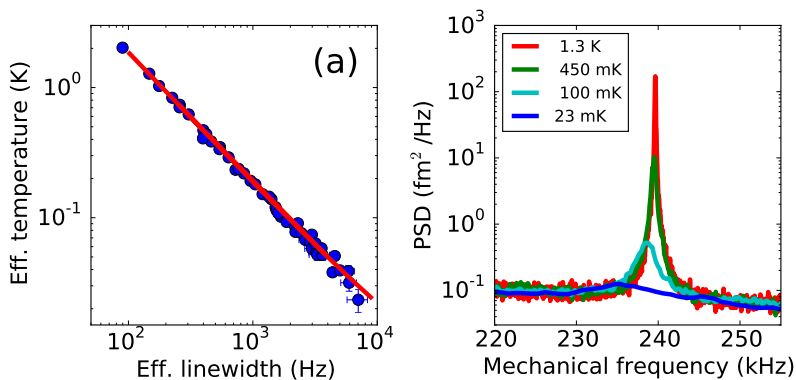


Figure 8.3: At a fixed laser detuning of $\Delta = -\Omega_m$ the intensity of the pump laser is varied. (a) The effective linewidth and effective temperature show the expected behavior. (b) Selection of mechanical noise spectra are shown to demonstrate the quality of the data.

librium with the environment at 293 K. Therefore the total integrated area of the mechanical thermal noise spectrum is set to correspond to an effective temperature of 293 K. Subsequently, when the pump laser is on, the integrated area of the measured spectrum is compared to the integrated area of the mechanical thermal noise spectrum at 293 K.

The results are shown in Fig. 8.2. The laser detuning is given in units of the inner resonator frequency Ω_m . The data, blue points in Fig. 8.2(a-c), are fitted according to the standard optomechanical theory for a single resonator (see chapters 2 and 5). The red curves show the results of a simultaneous fit to all three data-sets with only the cavity linewidth and input laser power as free parameters. An optical linewidth of $\kappa=52.2\pm 0.9$ kHz is in agreement with the value found from the optical ringdown. The fitted value of 3.00 ± 0.05 μ W for the input laser power can be used to relate the optical power launched at the cavity to the actual power coupled to the cavity mode. This is important in the next part, where we fix the laser detuning and increase the laser power.

Fig. 8.3(a) shows the results of the side-band cooling when the cooling laser is fixed at $\Delta = -\Omega_m$ and the power is varied. The results follow nicely the expected relationship indicated by the red line. In Fig. 8.3(b) some of the mechanical noise spectra are shown. Note again that, because of the nested design, the spectra are particularly clean and free of any additional mechanical modes. For the largest pump laser power, an effective temperature of 23 ± 5 mK is reached, starting from room temperature (cooling factor of 12700). When we try to increase the laser power even further, we observe that the system becomes highly unstable.

Although the radiation pressure only exerts a force on the small mirror, the inner and outer resonator are coupled because they are physically connected to each other. Therefore, the cavity field can still influence the motion of the low frequency outer resonator. In the next section a mechanical model of the nested resonator is discussed and we investigate if the design of a nested resonator can lead to an unstable

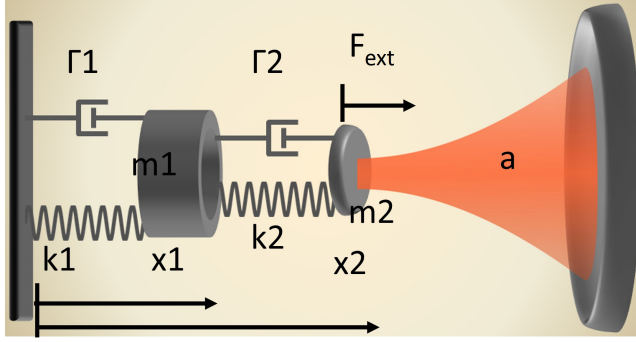


Figure 8.4: Schematic of the double resonator including relevant parameters

mechanical system for certain system parameters.

8.3 Model of a nested resonator

In Fig. 8.4 a schematic of the double resonator is shown, including relevant terms. The equations of motion for the the system are the following:

$$m_1 \ddot{x}_1 + (\Gamma_1 + \Gamma_2) \dot{x}_1 - \Gamma_2 \dot{x}_2 + (k_1 + k_2)x_1 - k_2 x_2 = 0 \quad (8.1)$$

$$m_2 \ddot{x}_2 + \Gamma_2 (\dot{x}_2 - \dot{x}_1) + k_2 (x_2 - x_1) - \hbar G |\alpha|^2 = F_{ext} \quad (8.2)$$

$$\dot{a} = -\frac{\kappa}{2} a + i(\Delta + Gx_2)a + \sqrt{\kappa_{ex}} s_{in} \quad (8.3)$$

in which m_i , Γ_i and k_i are the mass, damping rate and spring constant of each resonator, a denotes the cavity field amplitude, Δ the laser detuning, G the cavity frequency shift per displacement and κ_{ex} the coupling rate of the incoming field s_{in} . To find the mechanical response of the system for some applied external force F_{ext} , the cavity field equation can be linearized using $a = \bar{a} + \delta a$ (similar to the approach in chapter 2). By taking the Fourier transform, collecting terms and rewriting using $k_i = \Omega_i^2 m$ the following three equations are obtained:

$$x_1[\omega](m_1(\Omega_1^2 - \omega^2) + m_2\Omega_2^2 - i\omega(m_1\Gamma_1 + m_2\Gamma_2)) - x_2[\omega](\Omega_2^2 m_2 - i\omega m_2 \Gamma_2) = 0 \quad (8.4)$$

$$x_2[\omega](m_2(\Omega_1^2 - \omega^2) - i\omega m_2 \Gamma_2) - x_1[\omega](m_2\Omega_2^2 - i\omega m_2 \Gamma_2) - \hbar G (\bar{a}^* \delta a[\omega] + \bar{a} \delta a[\omega]^*) = F_{ext}[\omega] \quad (8.5)$$

$$-i\omega \delta a[\omega] = (i\Delta - \kappa/2) \delta a[\omega] + iG \bar{a} x_2[\omega] \quad (8.6)$$

Now Eqs. (8.4) and (8.6) can be used to rewrite Eq. (8.5) in the following form: $x_2[\omega] \chi_2^{-1} = F_{ext}[\omega]$ with χ_2 the mechanical susceptibility of mass 2, the inner resonator. The result is the following:

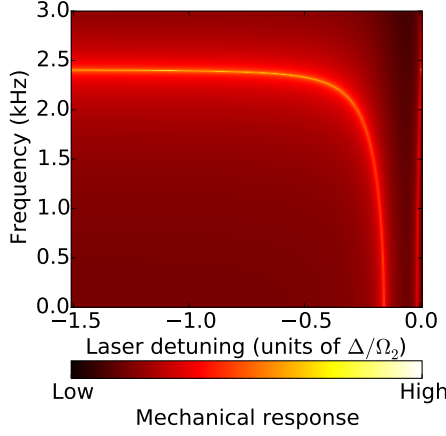


Figure 8.5: Mechanical response of the outer resonator as function of laser detuning.

$$x_2[\omega] \left(m_2((\Omega_2^2 - \omega^2) - i\omega\Gamma_2) + \frac{2m_2\Omega_2g^2}{\Delta + \omega + i\kappa/2} + \frac{1}{\Delta - \omega - i\kappa/2} - \frac{m_2(\Omega_2^2 - i\omega\Gamma_2)}{m_1(\Omega_1^2 - \omega^2) + m_2\Omega_2^2 - i\omega(m_1\Gamma_1 + m_2\Gamma_2)} \right) = F_{ext}[\omega] \quad (8.7)$$

The multi-photon coupling rate $g^2 = \hbar G^2 |a|^2 / (2m_2\Omega_2)$ is introduced to simplify the equation. The inverse susceptibility χ_2^{-1} contains three terms (note the linear nature of the mechanics). The first term is the response of a damped harmonic oscillator. The second term is the optomechanical interaction. This term is identical to the case of a single mechanical resonator (see chapter 2). The real part results in the familiar optical spring effect and the imaginary part gives the optical damping. The final term is the coupling with the outer resonator. From χ_2 the amplitude response of the inner resonator is extracted by $|\chi_2|$ and the phase response by $\arg(\chi_2)$.

We are however interested in the mechanical response of the outer resonator. Combining the result of Eq. (8.7) with Eq. (8.4) we find the following:

$$\chi_1 = \chi_2 \frac{m_2(\Omega_2^2 - i\omega\Gamma_2)}{m_1(\Omega_1^2 - \omega^2) + m_2\Omega_2^2 - i\omega(m_1\Gamma_1 + m_2\Gamma_2)} \quad (8.8)$$

As before the amplitude and phase response of the outer resonator are found via the magnitude and argument of χ_1 .

Now the response of the nested resonator can be investigated. Fig. 8.5 shows the mechanical response of the outer resonator as a function of laser detuning. The same values are used as for the measurements of Fig. 8.2. For a laser detuning of $\Delta = -1.5\Omega_2$, the resonance frequency of the outer resonator is still unaffected by the

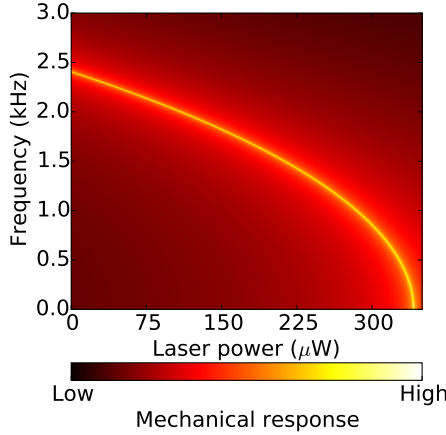


Figure 8.6: Mechanical response of the outer resonator as function of laser power for a fixed detuning of $\Delta = -\Omega_2$.

optical field. In the region between $\Delta = -0.5\Omega_2$ and $\Delta = 0$, the mechanical resonance frequency slowly decreases to zero, as indicated by the yellow line in Fig. 8.5. For the outer resonator, the optomechanical system is highly non side-band resolved, therefore a large optical spring effect is not surprising. The outer resonator experiences this optical spring effect via the coupling to the mirror of the inner resonator. Therefore the nested resonator can be considered a single mechanical oscillator at low frequencies.

In the region between $\Delta = -0.2\Omega_2$ and $\Delta = 0$, the optical spring effect has reduced the mechanical frequency to zero. Furthermore, the optical spring effect is so large that the system has a negative spring constant. This leads to an anti-stable system, as has been demonstrated by Corbitt et al. [75]. We have verified this behavior experimentally. Placing the pump laser between $\Delta = -0.2\Omega_2$ and $\Delta = 0$ results in an unstable mechanical system.

A similar instability is observed when the laser power is increased. This was the main limitation in the experiment of Fig. 8.3. We can therefore also investigate the mechanical response when the laser detuning is fixed at $\Delta = -\Omega_2$ while varying the laser power. The results are shown in Fig. 8.6. The same values are used as for the measurements of Fig. 8.3. For a single resonator the optical spring effect increases with power. It is therefore not surprising that for high laser powers at $\Delta = -\Omega_2$ a significant optical spring effect occurs for the outer resonator.

It is not uncommon for undesired effects, such as heating of the mechanical system due to optical absorption or excess laser noise, to appear at high laser powers [71, 118]. These effects typically limit the effective temperature reached with side-band cooling. In the case of a nested resonator, the mechanics of the design itself places an upper limit on the amount of laser power that can be used. This can potentially be an issue for future experiments. However, achieving a cooling factor of 13000 before the design of the nested resonator became a limiting factor suggests

that the issue is not likely to be a deal-breaker for reaching the quantum mechanical ground state. Should a solution be needed, the resonance frequency of the outer resonator can be increased. A drawback of this solution is the reduction in isolation of the inner resonator from the environment. An alternative route would be to implement additional control of the motion of the outer resonator. This can be done electrically via capacitive coupling or via the dielectric force [119] or even optically using additional laser beams [75].

Another motivation for additional control over the motion of the outer resonator is the high mechanical quality factor. The low frequency of the outer resonator, needed to provide sufficient isolation, can be easily excited by the boiling of cryogenic liquids or the presence of cryocoolers. Together with the high mechanical quality factor this can lead to a significant displacement of the outer resonator. Since the amount of isolation does not depend on the mechanical quality factor [35], additional damping can be applied via an active feedback method, to reduce the quality factor but still keep the mechanical isolation. The next chapter investigates active feedback cooling as a method to control the motion of the outer resonator.

8.4 Conclusions

With the recent introduction of the nested trampoline design, both good optical and mechanical properties are combined in a relatively low frequency high mass optomechanical device. We have demonstrated in this chapter that such a device can successfully be used for optical cooling experiments, reaching an effective temperature of 23 ± 5 mK starting from room temperature. The cooling performance turns out to be limited by a large optical spring effect acting on the outer resonator. The resonance frequency is lowered close to zero, leading to a system which is very vulnerable to low frequency noise.

An attractive solution would be to add additional control over the motion of the outer resonator. Not only can this be used to counteract the optical spring effect, but the outer resonator can also be damped to reduce the mechanical quality factor. This reduces the movement of the outer resonator due to external forces when the set-up is placed in a noisy, cryogenic environment, which is required for reaching the quantum mechanical ground state.

High-Q nested resonator in an actively stabilized optomechanical cavity

Experiments involving micro- and nanomechanical resonators need to be carefully designed to reduce mechanical environmental noise. A small scale on-chip approach is to add a resonator to the system as a mechanical low-pass filter. However, the inherent low frequency of the low-pass filter causes the system to be easily excited mechanically. In this chapter, we solve this problem by applying active feedback to the resonator, thereby minimizing the motion with respect the front mirror of an optomechanical cavity. Not only does this method actively stabilize the cavity length, but it also retains the on-chip vibration isolation.

9.1 Introduction

Micro- and nanomechanical systems are widely used for precision measurements across a variety of research topics, see Ref. [120] for an overview. In cavity optomechanics for example, electromagnetic radiation is used to perform displacement measurements that beat the standard quantum limit [104, 106]. Similarly, in atomic force microscopy (AFM) forces as small as 10^{-18} N are measurable [121].

A common challenge when using mechanical resonators is achieving a high mechanical quality factor (Q-factor) and shielding from vibrational noise. Recently, clamping losses, or coupling to external mechanical modes, has been identified as a major source of loss in mechanical systems [122, 123, 124], affecting both the mechanical Q-factor and the amount of vibrational noise entering the system. A solution to this problem is to introduce phononic crystals [102, 103] and low frequency mechanical resonators [125, 126, 35] to isolate the device from the environment.

Surrounding the resonator of interest with an additional low frequency resonator has a severe drawback. The additional low frequency resonator itself can be mechanically excited by the environment. The obvious solution would be to fixate the additional resonator, but this will remove the effect of the mechanical low-pass filter. Typically this trade-off is circumvented by reducing the motion of the additional resonator using active feedback cooling.

Active feedback cooling, also called cold damping, uses the real time displacement of the mechanical resonator to apply a suitable feedback signal to an actuator (mechanical, optical or electrical) [108, 109, 110, 111, 112, 113, 114]. Increasing the gain of the feedback signal to the actuator results in more feedback cooling up to the point where the amplified read-out noise causes the mechanical motion to increase.

In this article we will first demonstrate active feedback cooling of our nested trampoline resonator [35]. Because this resonator is part of an optomechanical cavity, a more elegant approach to solving this problem is possible. We will show how, by actively stabilizing the position of the resonator with respect to the front mirror of the cavity, all length variations of the cavity are eliminated, including the motion of the low frequency resonator while retaining the on-chip vibration isolation.

9.2 Experimental details

For the actuation we make use of the dielectric force. This is convenient as any dielectric body in the presence of an electric field gradient experiences a dielectric force [2]. Recently this method was also used to demonstrate control of micro- and nanomechanical resonators [127, 119].

The energy of a dipole in an electric field is $U = -\mathbf{p} \cdot \mathbf{E}$. The force the dipole experiences is $\mathbf{F} = -\nabla U = (\mathbf{p} \cdot \nabla)\mathbf{E}$. With the dipole moment $\mathbf{p} = \alpha\mathbf{E}$, this can be written as $\mathbf{F} = (\alpha\mathbf{E} \cdot \nabla)\mathbf{E}$. The strength of the dielectric force depends therefore on the applied electric field, its gradient and the polarizability of the medium. Although the nested resonator is largely made from silicon, which is weakly polarizable, the experiment is carried out in vacuum, so relatively large electric fields can be generated. For example, a back-of-the-envelope calculation using a charged sphere placed

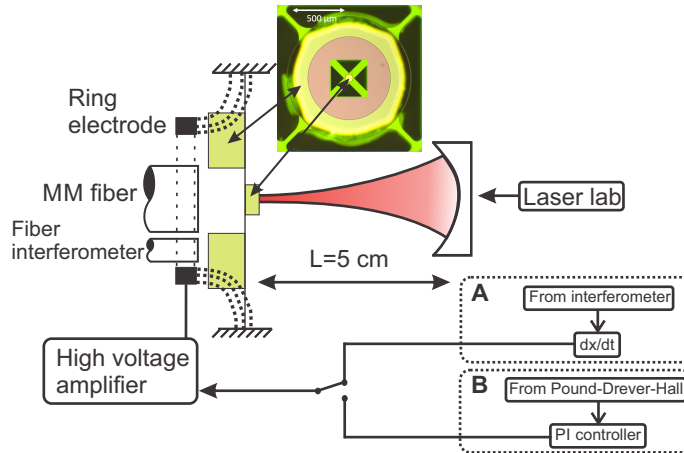


Figure 9.1: Schematic overview of the geometry for applying an electric field gradient. A ring electrode, single-mode (SM) fiber and multi-mode (MM) fiber are placed behind the resonator. The resonator itself is part of an optomechanical Fabry-Perot cavity. Either the output from the fiber interferometer or the Pound-Drever-Hall error signal is used to drive the high voltage amplifier connected to the ring electrode. More details of the optical set-up can be found in Eerkens et al. [67]. Inset: optical image of the nested resonator which consists of an inner trampoline resonator surrounded by a larger outer resonator.

$\sim \mu\text{m}$ distance behind our sample [128] shows that forces up to $\sim \mu\text{N}$ are feasible.

We realize an electric field gradient by placing a small ring electrode behind the nested resonator, as depicted in Fig. 9.1. The typical distance between electrode and resonator is $500 \mu\text{m}$. Both a bias voltage and a modulation voltage are applied. Since the electric field is linear in applied voltage, the dielectric force can be written as $F = \beta V^2 = \beta (V_{d.c.} + V_{a.c.})^2 \approx \beta V_{d.c.}^2 + 2\beta V_{d.c.} V_{a.c.}$ in the limit when the applied bias $V_{d.c.}$ is much larger than the modulation $V_{a.c.}$, with β being some constant. Note that the force is now linear in $V_{a.c.}$, therefore a modulation at frequency f_0 will result in a force at frequency f_0 .

The read-out of the mechanical motion is done in three different ways. A single-mode (SM) fiber is located approx. $500 \mu\text{m}$ behind the mass of the outer resonator to form a fiber interferometer [100], as is shown in Fig. 9.1. The interference signal created by the light reflecting off the outer resonator and the light reflected off the fiber facet allows for a sensitive read-out of the resonators motion. Our home-built fiber interferometer using a standard distributed feedback laser diode at 1550 nm reaches a read-out sensitivity of approx. $300 \text{ fm}/\sqrt{\text{Hz}}$ around 3.5 kHz .

For the second read-out method a low finesse ($F=300$) Fabry-Perot cavity, 5 cm long operating around 980 nm , is used. The transmitted cavity light is collected using a multi-mode (MM) fiber placed in the center behind the sample as is shown in Fig. 9.1.

The third method uses the same Fabry-Perot cavity together with a wavelength of 1064 nm to create a high finesse ($F \approx 17000$) cavity. The Pound-Drever-Hall method [38] is used to read out the displacement of this cavity from the light reflecting off

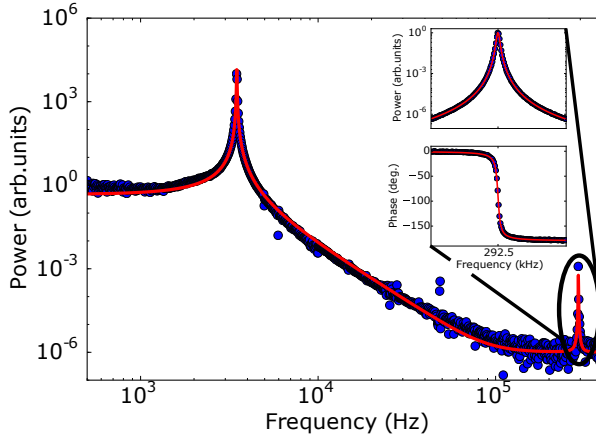


Figure 9.2: The mechanical transfer function of the nested resonator design measured by applying an electrostatic force to the outer resonator and reading out the response of the inner resonator via the cavity. Inset: Driven response of the inner resonator.

the cavity. Finally, the whole set-up resides in a vibration isolated vacuum chamber with a base pressure of 10^{-3} mbar to eliminate the effect of gas damping on the mechanical properties.

As a demonstration of the actuation via the dielectric force, the mechanical transfer function of the nested resonator is measured. The frequency of the applied force to the outer resonator is varied via the reference output of a lock-in amplifier and the response of the inner resonator is measured using the low finesse optical cavity together with the same lock-in amplifier. The data (blue points) of Fig. 9.2 follow the theory curve for two coupled harmonic oscillators. At the frequency of the inner resonator, which for this sample is 292.5 kHz, more than 60 dB of isolation is provided via the nested resonator design. This is consistent with previous findings [35]. The inset shows that the inner resonator can be driven in this way as well. Note that this measurement assumes a constant force excitation which, judging by the agreement between experiment and theory of Fig. 9.2, is valid. Therefore the bandwidth of this method of actuation is at least 100 kHz.

9.3 Results

9.3.1 Active feedback cooling

The main point of the addition of a dielectric force is not to drive the outer resonator, but to reduce its motion. To do so, we use the method of active feedback cooling [108]. The displacement signal from the fiber interferometer is sent through a differentiating circuit and is amplified with a variable gain amplifier (see Fig. 9.1). Together with a DC voltage the signal is then sent to the ring electrode to provide a damping force for the motion of the outer resonator. To avoid difficulty in interpret-

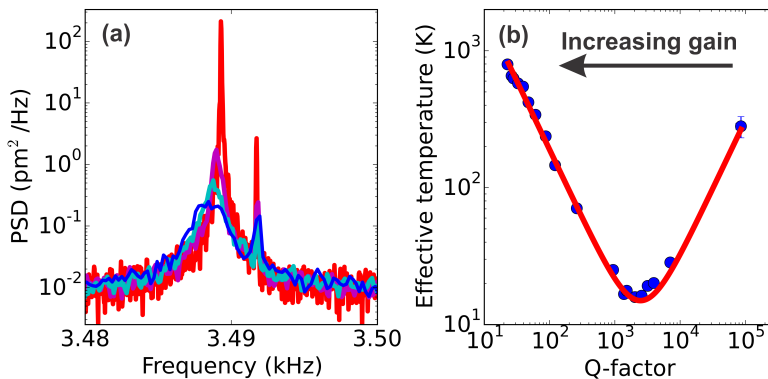


Figure 9.3: Active feedback cooling of the outer resonator. When the gain is increased, both the effective temperature and the Q-factor decreases. For large gains, the amplified read-out noise actually drives the outer resonator, increasing the effective temperature. (a) Selection of power spectra demonstrating cooling of the mechanical mode. This out-of-loop measurement uses the read-out via the low finesse cavity. Note that a small additional resonance is visible. (b) Effective mode temperature as a function of mechanical Q.

ing the data [114], we use an out-of-loop measurement provided by the low finesse cavity to read out the effect of the feedback.

From the mechanical noise spectrum obtained via the cavity read-out, the effective mechanical Q-factor of the outer resonator is determined together with the total displacement $\langle x^2 \rangle$ by fitting a Lorentzian. Via the equipartition theorem the effective temperature can be calculated using $T = \langle x^2 \rangle M \Omega_m^2 / k_b$ with k_b the Boltzmann constant, $M = 7 \times 10^{-7}$ kg, and $\Omega_m = 2\pi \times 3488$ rad/s for this particular sample.

With the feedback circuit activated, the motion of the resonator will be both damped and cooled. Increasing the gain results in more damping and cooling of the mechanical motion up to the point where the amplified detection noise becomes comparable to the thermal noise. The amplified read-out noise from the feedback is transferred to the mechanical motion of the resonator, causing the effective temperature to increase again. We have observed precisely this behavior, as is shown in Fig. 9.3. Note that this is visible because of the out-of-loop measurement. Measuring the mechanical noise spectrum via the interferometer, within the feedback loop, will result in noise squashing [114].

We are able to reduce the intrinsic Q-factor of 90000 to about 20, limited only by the gain of the amplifier. The mechanical mode temperature is reduced to about 15 K using this form of cooling. To check if the limiting factor of the mode temperature is indeed the noise floor of the interferometric read-out, the data is fitted using the theory derived by Poggio et al. [114]. For active feedback cooling the effective temperature is given by:

$$T_{\text{eff}} = \frac{T_{\text{bath}} Q}{Q_0} + \frac{k \Omega_m (Q - Q_0)^2}{4 k_b Q_0^2 Q} S_{x_n} \quad (9.1)$$

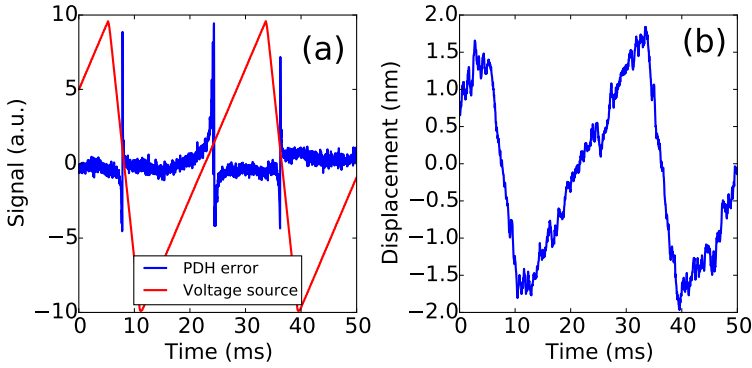


Figure 9.4: Scanning of the cavity length (a) Varying the position of the outer resonator results in the typical PDH error signal. (b) The displacement of the outer resonator is monitored using the fiber interferometer.

with T_{bath} the environmental temperature, Q the quality factor, k the spring constant, Q_0 the intrinsic quality factor and S_{x_n} the read-out noise power. In our case: $k = 340$ N/m, $T_{\text{bath}} = 293$ K, and $Q_0 = 90000$. The only free parameter is the read-out noise power S_{x_n} . From the fit (red curve Fig. 9.3(b)) we obtain a value for $\sqrt{S_{x_n}} = 380 \pm 10$ fm/ $\sqrt{\text{Hz}}$, which is close to the noise floor of our interferometric read-out.

Using active feedback the total rms displacement is reduced from 6 pm to 0.8 pm, which for most applications is sufficient. However in our case, we require further reduction of the motion. To achieve this, the interferometric read-out is replaced with a more sensitive read-out method using a high finesse optical cavity.

9.3.2 Active stabilization

The use of a high finesse optical cavity typically requires a means to keep laser and cavity resonant. Usually, the laser frequency is continuously adjusted to keep it resonant with the cavity mode. An alternative method would be to adjust the cavity length to keep the cavity resonant with the laser. For the set-up depicted in Fig. 9.1, the cavity length L can be varied by changing the position of the outer resonator using the dielectric force, while tracking the cavity resonance via the Pound-Drever-Hall (PDH) method [38]. In this way the nested resonator design not only mechanically decouples the inner resonator from the environment, but also stabilizes the cavity length with respect to the laser frequency.

In Fig. 9.4(a) the typical PDH error signal (blue) is obtained by scanning the cavity length using a high voltage amplifier (red). Note that to ensure a linear response, a DC bias voltage (not shown here) is also added. The displacement of the outer resonator is observed via the interferometer, as is shown in Fig. 9.4(b). The employed scanning voltage range provides us with a cavity length adjustment of ± 1.5 nm, which is enough for keeping the cavity resonant with the laser.

We typically require a feedback bandwidth of about 10 kHz to keep laser and cavity resonant. However, the mechanical resonance at $f = 3488$ Hz provides a very

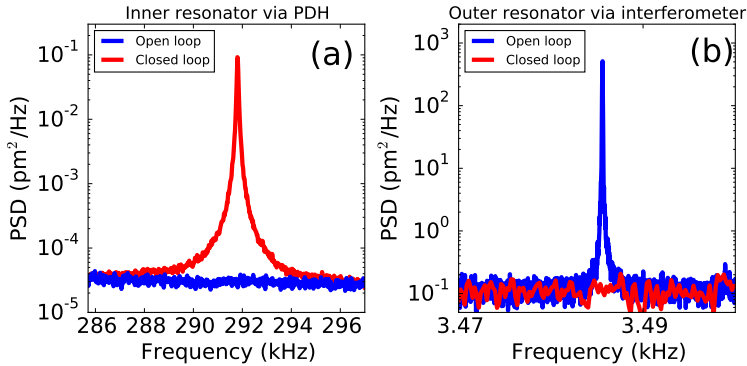


Figure 9.5: Active stabilization of the outer resonator. When the feedback loop is closed, the cavity is resonant with the laser, making the motion of the inner resonator visible as is shown in (a). On the other hand, the motion of the outer resonator is no longer visible via the interferometer, as is shown in (b).

rapid π phase shift in the transfer function. A notch filter is placed at $f = 3.4$ kHz in the feedback loop to smooth this transition. A second notch filter at $f = 10.2$ kHz is used to compensate the first higher order mechanical mode.

When the feedback loop is closed, the cavity should remain resonant with the laser. Therefore the motion of the inner resonator, which occurs at a frequency beyond the feedback bandwidth, should be visible in the PDH error signal. Fig. 9.5(a) shows the Fourier transform of this error signal and indeed, with a closed loop, the thermal motion of the inner resonator is visible. The thermal motion of the outer resonator has been mostly eliminated, and is no longer visible via the interferometric read-out, see Fig. 9.5(b).

From Fig. 9.5 it is clear that the feedback not only works, but also that the on-chip isolation still works as evidenced by the clean spectrum of Fig. 9.5(a). However, what has happened to the motion of the outer resonator? Effectively, with active stabilization, a very strong electrical spring is placed between the outer resonator and the front mirror. The only way for the outer resonator to move at a particular frequency, is if the front mirror also moves at this frequency. This stiffening of the outer resonator explains why, with a closed loop, the mechanical motion is no longer visible in Fig. 9.5(b). The additional electrical spring also helps to prevent any unwanted optical spring effects [75] present in an optomechanical cavity.

9.4 Conclusion

In conclusion, we have demonstrated how to solve the problem of fixating an on-chip mechanical low-pass filter while retaining the mechanical isolation. By making use of an optomechanical cavity, the motion of the resonator can be referenced to the front mirror. Not only does this stabilize the cavity with respect to the laser, it also stiffens the resonator, thereby significantly reducing its motion. We have made use

of an optomechanical system, but in principle the techniques presented in this work can be applied to any system as long as a suitable reference can be chosen.

Acknowledgment

The authors acknowledge the useful discussions with W. Loeffler. The authors would also like to thank H. van der Meer for technical assistance and support.

Optomechanical experiments in a cryogen free dilution refrigerator

We have shown in the previous chapters how optical cooling can greatly reduce the effective mode temperature of the mechanical resonator. In this chapter, we perform optical side-band cooling at cryogenic temperatures, since only a combination of optical and cryogenic cooling will be sufficient to reach the quantum mechanical ground state. First, we describe the mass-spring system developed to mechanically isolate the optical set-up from the vibrations generated in a cryogen free cryostat. Next we demonstrate how via optical side-band cooling an effective mechanical mode temperature of 3.09 ± 0.07 mK is achieved. This temperature corresponds to an RMS motion of 9.2 ± 0.15 fm, demonstrating femtometer read-out precision in a dry cryostat. Finally we discuss some of the limiting factors in achieving the quantum mechanical ground-state and suggest improvements for the future.

10.1 Mechanical low-pass filters

The experiments at cryogenic temperatures are performed in a cryogen free dilution refrigerator (Leiden Cryogenics CF-CS81-1400) which uses a pulse tube (PT) cryocooler instead of liquid helium to reach 4 Kelvin. The use of a cryocooler introduces additional vibrations, from which the experiment needs to be isolated. The cryostat itself is already modified to reduce vibrations. For example, the cold head of the pulse tube is connected via copper braids to the 50 Kelvin and 3 Kelvin plate instead of a rigid connection. Furthermore, the still plate is suspended via springs from the 3 Kelvin plate to form a mass spring system with a cut-off frequency of approximately 2 Hz of which the motion is damped by Eddy current dampers. A more detailed overview is presented in the work of den Haan et al. [129]. Although these modifications are a major improvement, additional isolation between the mixing chamber plate and the experimental set-up is needed. Based on the work of K. Heck [130], we will discuss in this section the design of a mechanical low-pass filter.

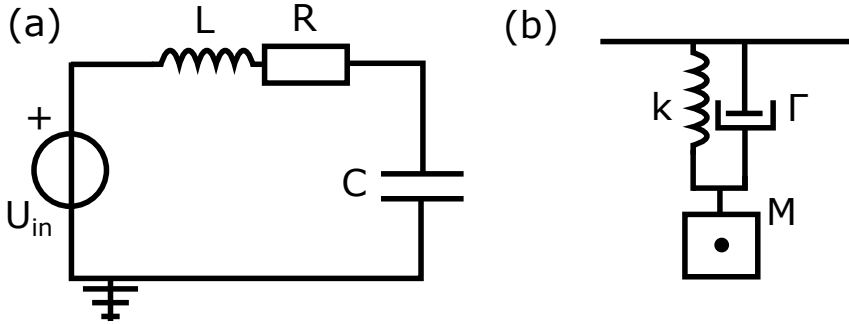


Figure 10.1: The response of the LCR circuit in (a) and the damped harmonic oscillator in (b) can both be described by a differential equation of the same form.

10.1.1 Correspondence between electrical and mechanical networks

Filters are common in electrical circuits, making them a natural place to start. Additionally, there is a correspondence between electrical circuits, such as the LCR circuit shown in Fig. 10.1(a), and mechanical structures, such as the damped harmonic oscillator in Fig. 10.1(b). We will illustrate this correspondence with a simple example. Using Kirchoff's voltage law, the following differential equation is obtained for the circuit in Fig. 10.1(a):

$$L \frac{d^2 q}{dt^2} + R \frac{dq}{dt} + \frac{q}{C} = U_{in} \quad (10.1)$$

in which L is the inductance, R the resistance, C the capacitance, q the charge and U_{in} the input voltage. Using Newton's laws, the following equation of motion is obtained for the damped harmonic oscillator in Fig. 10.1(b):

$$M \frac{d^2 x}{dt^2} + M\Gamma \frac{dx}{dt} + kx = 0 \quad (10.2)$$

in which M is the mass, Γ the damping rate, k the spring constant and x the displacement. When comparing Eqs. (10.1) and (10.2) one can see that they are both second-order differential equations. Furthermore, one can link equivalent components together: mass and inductance, damping rate and resistance, and spring constant and capacitance.

Kirchoff's voltage law states that the sum of the electrical potential differences in any closed loop is zero. This is an example of a loop or maze equation. Kirchoff's current law states that the sum of all currents flowing to and from a node add up to zero. This is an example of a node equation. Equation (10.1) is derived via a maze equation, while Eq. (10.2) adds all forces at the center of mass M . Equation (10.2) is therefore a node equation. Since node equations in electrical circuits relate to currents, we can link an electrical current to a mechanical force. Finally, since both the velocity and the voltage have a gauge freedom (i.e. offsets can be added freely to them without changing the physics) we see that they are analogous and thus we can

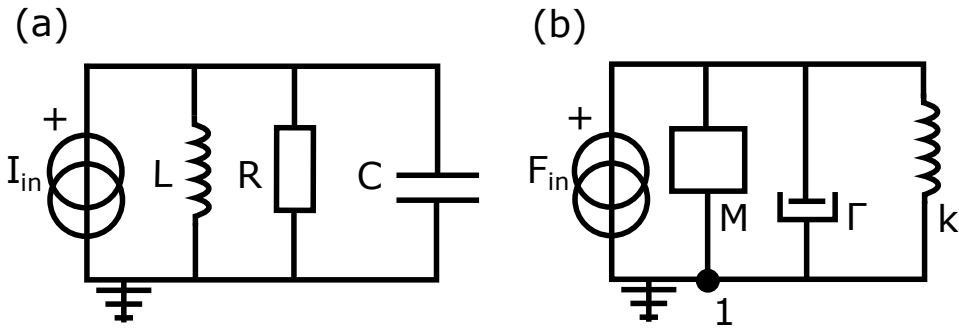


Figure 10.2: (a) The dual of the series LCR circuit is a parallel LCR circuit. (b) The mechanical circuit diagram of a damped harmonic oscillator.

connect voltage to velocity.¹

With the correspondence in place, we can ask the following question: can we find the circuit diagram of the mechanical structure in Fig. 10.1(b), using the LCR circuit in (a) as a starting point? If we take the dual network [131] of the LCR circuit, the voltage source becomes a current source and all elements in series will now be in parallel.² Figure 10.2(a) shows this dual circuit. Note that the series LCR circuit of Fig. 10.1(a) describes a band-pass filter, while the dual circuit, a parallel LCR circuit, is a band-stop filter. The dual transformation has inverted all properties of the original network. If we now replace all electrical components with their mechanical counterparts, we obtain the circuit shown in Fig. 10.2(b). Applying the node equation to the node indicated with 1 in Fig. 10.2(b), we obtain the following equation:

$$M \frac{d^2x}{dt^2} + M\Gamma \frac{dx}{dt} + kx = F_{in} \quad (10.3)$$

which is precisely the equation of motion describing a damped harmonic oscillator. Although the schematic overview shown in Fig. 10.1(b) and the mechanical circuit diagram of Fig. 10.2(b) may not look the same, they are both described by the same differential equation and are therefore equivalent representations of a damped harmonic oscillator.

The mechanical circuit diagram has some interesting properties. For example, it makes sense that a damper and spring have two connections on either side, just as their electrical counterparts. But what does it mean that the mass M has two connections as well? Velocity has now taken the role of voltage. As such, the velocity must be expressed with respect to some reference, in this case the coordinate origin. This coordinate origin is the same for all the velocities of the masses.³ The most conve-

¹Not only velocity but also position has a gauge freedom. It is, however, convenient to have velocity correspond to voltage. As we will see in the next paragraphs.

²Additionally, one writes down the conductance of each element instead of the impedance, when transforming to the dual network, see the work of Tellegen [131] for a rigorous treatment.

³If this is not the case, we have a mechanical circuit that connects different inertial reference frames together. Since the velocity of each frame does not need to be the same, the circuit can literally be pulled apart.

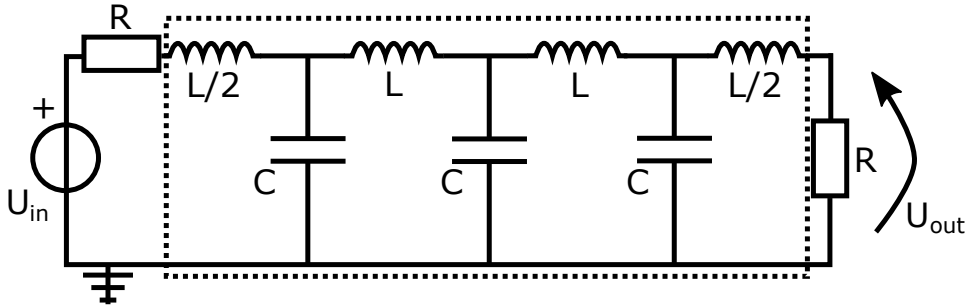


Figure 10.3: Circuit diagram of a third order electrical low-pass filter, shown in the dashed box. This is the starting point for designing the mechanical filter.

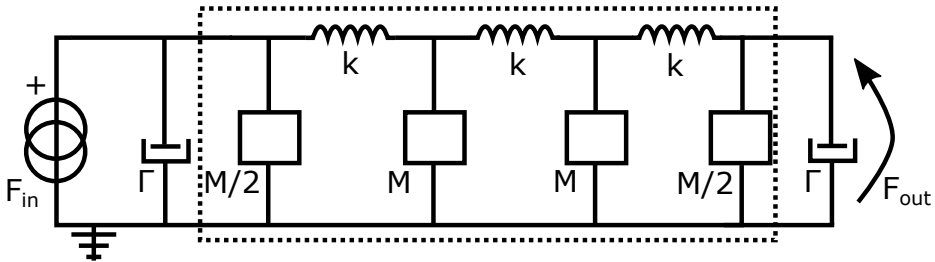


Figure 10.4: Circuit diagram of the ideal mechanical low-pass filter derived from the electrical equivalent circuit shown in Fig. 10.3.

nient reference is therefore to connect each mass to ground. Although any electrical circuit has a mechanical equivalent, only mechanical circuits with the masses connected to ground can be physically realized. Therefore the original electrical circuit must have the inductors on the outer contours of the diagram.

We have found the equivalent mechanical circuit diagram by starting with an LCR circuit, writing down the dual circuit and interchanging electrical for mechanical components. The original LCR circuit acts as an electrical band-pass filter, while the damped harmonic oscillator can be viewed as a mechanical band-pass filter. To design a mechanical low-pass filter, we can thus use an electrical low-pass filter of choice as a blue-print for the mechanical low-pass filter, as we will show in the next section.

10.1.2 Mechanical low-pass filter

The most simple example of an electrical low-pass filter is perhaps the wave filter (constant-k filter) [132], in which identical sections make up a ladder structure. A third order electrical low-pass filter, see Figure 10.3, is chosen as a starting point. Higher order filters are of course possible, at the expense of a larger structure. A third order filter is therefore a compromise between performance and size.

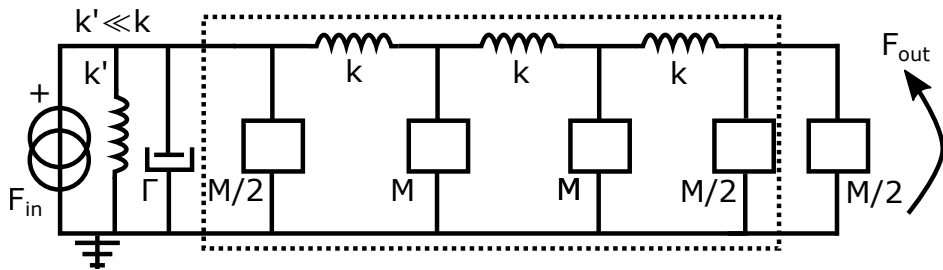


Figure 10.5: The final mechanical low-pass filter. Compared to the ideal low-pass filter in Fig. 10.4 the damper at the output is replaced with an additional mass, and the input has as an additional weak spring in parallel to carry DC forces.

If we now follow the method outlined in the previous section, we can write down the dual of the circuit in Fig. 10.3 and interchange the electrical components for their mechanical counterparts. The resulting circuit is shown in Fig. 10.4. We can already see that this mechanical filter can be physically realized, because each mass is connected to ground. With this in mind, one can also see that the damper at the output is impossible to construct, because the damper should also be referenced to the coordinate origin. This means that the damper will largely bypass the filter. No damper at the end means that reflections in the filter itself will increase the velocity at the output above the corner frequency of the filter. Numerical simulations show that this problem can be reduced by adding a mass $M/2$ to the output.

At the input a small adjustment is also needed. Suppose a DC force, for example the gravitational force acting on the optical set-up connected to the filter, is applied to the output of the filter shown in Fig. 10.4. Because this DC force is not resonant with any closed loop of the circuit, no force is generated to counteract the applied DC force. Therefore, the DC force is directly transmitted to the damper at the input. The response of the damper is to continuously expand, therefore the damper can not carry a DC force. This problem can be solved by adding a weak spring, with a spring constant much smaller than the spring constant of the interconnecting springs, parallel to the damper. The final diagram of the mechanical low-pass filter is shown in Fig. 10.5.

With the diagram of the filter explained, we turn to the characteristics of the filter. To calculate the corner frequency, we make use of the theory developed for wave filters by Campbell [132]. The corner frequency of the filter shown in Fig. 10.5 is given by $f_0 = \frac{1}{\pi} \sqrt{k/m}$. Because the optical set-up shown in chapter 2 has a mass of 3.5 kg, it makes sense to choose the masses of the filter to be of that order. Although we would like to have the corner frequency to be as small as possible and therefore have very weak springs, the filter must still be able to carry weight of the set-up. This naturally limits the spring constant of the springs. We have chosen a mass m of 2 kg and a spring constant k of 50 kN/m, resulting in a corner frequency of $f_0 = 50$ Hz.

The only thing missing is the full transfer function of the mechanical filter. Figure 10.6(a) shows a schematic overview of the filter, based on the circuit diagram of Fig.

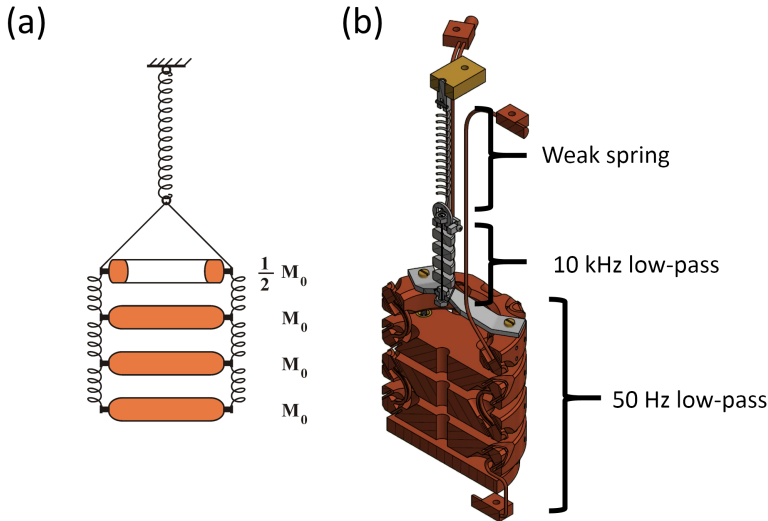


Figure 10.6: (a) Schematic overview of the third order mechanical low-pass filter based on the circuit diagram of Fig. 10.5. Note that the damper at the input is missing. (b) The final vibration isolation system, designed by K. Heeck and constructed by H. van der Meer, as used in the cryostat. Besides the mechanical filter with a corner frequency of 50 Hz, an additional low-pass filter at 10 kHz is added to reduce vibrations generated by the pulse tube's control current.

10.5. The damper at the input is not shown. The mechanical filter is nothing more than a coupled mass-spring system. Using Newton's laws, the full transfer function can be calculated. The final vibration isolation system is shown in Fig. 10.6(b). An additional low-pass filter at 10 kHz is also added to reduce mechanical noise in the cold head at 26 kHz, generated by the control current of the pulse tube. This filter is designed following the same principles as outlined above.

At the time of writing, a cryogenically compatible damper was still in development, therefore the vibration isolation system was operated without the damper. The performance of each filter was separately tested. For the 10 kHz filter as well as the 50 Hz filter, the position of each mechanical resonance was verified experimentally. Additionally, the transfer function of the 50 Hz filter was also measured at room temperature by applying a force excitation with constant amplitude via a voice coil attached to the first mass while measuring the response using a geophone attached to the final mass. Although this method of excitation only approximates a constant force excitation, it does provide a reasonable indication of the performance of the isolation stage. The results are shown in Fig. 10.7 together with the expected transfer function [130]. Although there are some discrepancies, the measurement matches the expected transfer function quite well. In particular, above 100 Hz more than 100 dB of isolation is achieved.

Four distinctive resonances are visible in Fig. 10.7, corresponding to the different

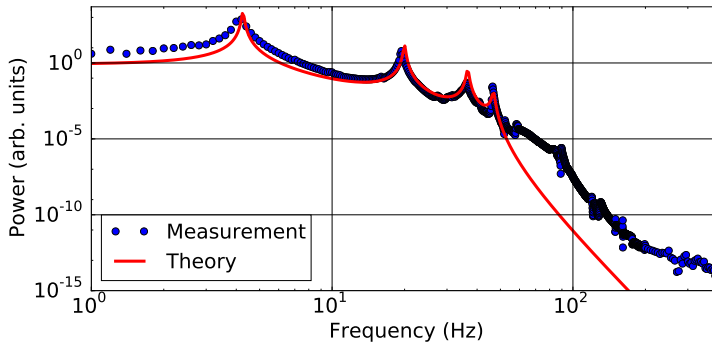


Figure 10.7: The mechanical transfer function as measured at room temperature for the 50 Hz filter, together with the theoretical prediction.

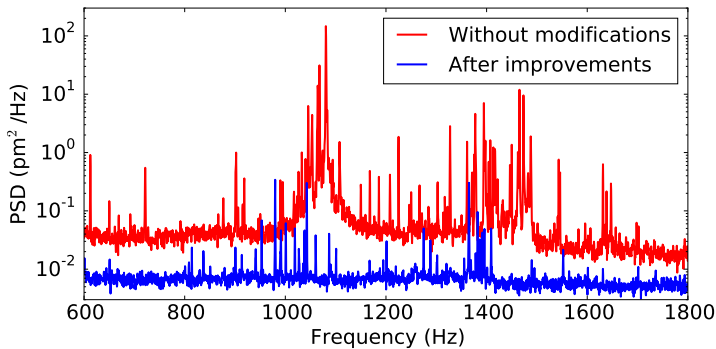


Figure 10.8: Mechanical displacement spectra as measured via the optical cavity at 100 mK. Red: the noise with a single stage mass-spring system and no modification to the cryostat. Blue: the remaining noise after lifting the pulse tube, suspending the still and using the vibration isolation system shown in Fig. 10.6(b).

modes of the mass-spring system itself. These can be suppressed by adding the mechanical damper. These additional resonances are however not an issue. Because the laser is actively locked to the cavity resonance, low frequency vibrations can be compensated for. The real problem was the internal mechanical modes of the optical set-up. These occur roughly at 1 kHz, the region in which the isolation system of Fig. 10.6 should perform optimally.

In Fig. 10.8 mechanical displacement spectra as measured via the optical cavity at 100 mK are shown. Without any modifications to the cryostat and using only a single stage mass-spring system, significant noise is visible between 1 and 1.6 kHz, as is indicated in red. After the modifications to the cryostat and using the isolation stage shown in Fig. 10.6(b), the noise has significantly reduced, as is shown in blue. The next section will show that with this isolation stage, sensitive optical experiments at cryogenic temperatures are possible.

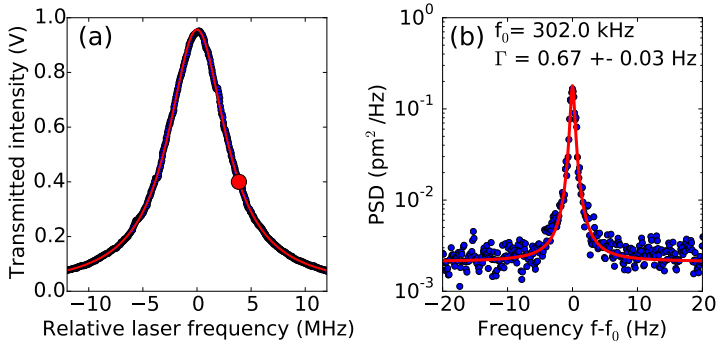


Figure 10.9: (a) Cavity resonance for the low finesse cavity created by using a 950 nm laser. (b) Power spectrum of the thermal motion measured via a side-of-fringe lock to the low finesse cavity. The red dot in (a) indicates the laser frequency that was used to measure the spectrum of (b).

10.2 Optical side-band cooling at cryogenic temperatures

Cooling down the cryostat occurs in two stages, first the cryostat cools to a base temperature of 5.7 Kelvin using the pulse tube cooler. During this stage, the active feedback demonstrated in the previous chapter is used to damp the motion of the outer resonator, while the PiezoKnob motors are used to actively keep the cavity aligned. When the base temperature is reached, all motors are shorted and the active feedback is turned off. The next step is to turn on the dilution refrigerator to reach mK temperatures. First we will report on measurements performed at 5.7 Kelvin. The cooling power of the cryostat at this temperature is significantly higher than at mK temperatures, so the lasers are not likely to heat up the set-up. After demonstrating stable operation of the optomechanical set-up at 5.7 Kelvin, the base temperature is lowered via the dilution refrigerator to see if the mechanical mode can be cooled even further.

10.2.1 Measurements at 5.7 Kelvin

First, we need verification of the mechanical mode temperature to confirm that the sample has thermalized properly. To ensure that the optical read-out does not modify the mechanical motion of the resonator via the optomechanical interaction, a laser wavelength of 950 nm is used, well outside the coating specifications of the DBR mirrors. In Fig. 10.9(a) the cavity resonance is shown together with a Lorentzian fit. The linewidth of the resonance is 6.5 MHz, resulting in a finesse of about 460. Via a side-of-fringe lock (see chapter 2) at a detuning indicated by the red dot in Fig. 10.9(a), the thermal motion of the resonator is measured. Because the finesse is low, the laser is far detuned and low laser power is used, optomechanical cooling and damping should not occur. This is verified by switching from positive to negative detunings and observing no change in the measured linewidth. Therefore this method is able

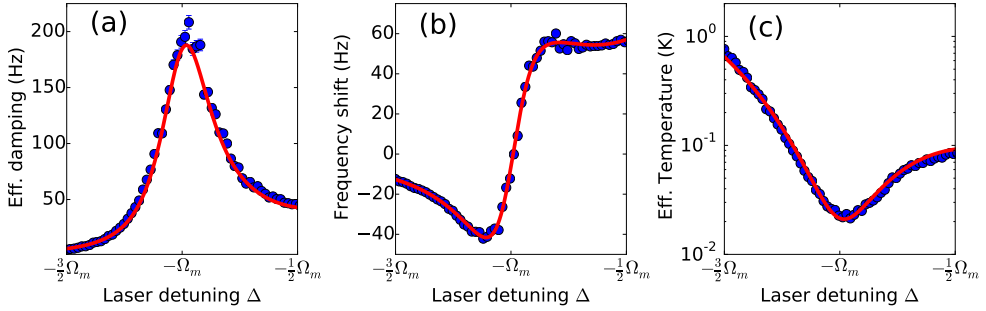


Figure 10.10: The blue data-points are obtained via a Lorentzian fit to the mechanical power spectra obtained from the PDH probe signal. The effective temperature is obtained from the integrated displacement power spectral density. The red curves are the result of a simultaneous fit to all three data-sets with only the optical linewidth and input power as free parameters.

to measure the intrinsic mechanical linewidth. Figure 10.9(b) shows the observed thermal motion. At 5.7 Kelvin we find a line-width of 0.67 ± 0.03 Hz at a frequency of 302 kHz.

Typically the power spectrum is measured in units of $V_{\text{rms}}^2/\text{Hz}$. From the optical resonance shown in Fig. 10.9(a) we can obtain the slope, in units of V/Hz at the specific detuning from the Lorentzian fit. Via the optical frequency shift per displacement $G = \frac{\omega_{\text{cav}}}{L}$, we can obtain a conversion factor in units of V/m . Via this conversion factor we can transform the scale of the measured power spectrum to m^2/Hz as is shown in Fig. 10.9(b). The area of the Lorentzian gives directly the displacement $\langle x(t)^2 \rangle$ of the mechanical resonator in the correct units. The mode temperature can be calculated via the equipartition theorem

$$T_{\text{mode}} = \frac{\langle x(t)^2 \rangle m \Omega_m^2}{k_b} \quad (10.4)$$

and using a mass of $m = 140$ ng obtained via COMSOL. We find a mode temperature of 5.7 ± 0.3 Kelvin, indicating that the mechanical mode is indeed thermalized to the base temperature of the cryostat. This method has been verified separately at room temperature as well, where the mode temperature is known.

To demonstrate the stability of the optical system at low temperatures, we use the method outlined in chapter 5 to perform optical side-band cooling. As a function of laser detuning we measure the mechanical displacement spectrum. By fitting the noise spectrum with a Lorentzian, we directly obtain the mechanical linewidth and frequency shift. The area of the Lorentzian is proportional to the effective temperature. As discussed in chapter 5, we use a relative calibration to scale this area to an effective temperature. As shown by the side-of-fringe lock in Fig. 10.9, the resonator is thermalized to the base temperature of the cryostat. Consequently, if we measure via the Pound-Drever-Hall (PDH) method the displacement of the resonator, we know that a measured linewidth of 0.67 Hz should correspond to a mode

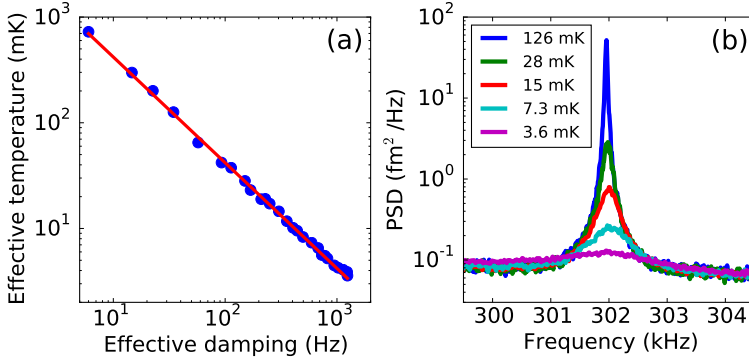


Figure 10.11: At a fixed laser detuning of $\Delta = -\Omega_m$ the intensity of the pump laser is varied. (a) The effective linewidth and effective temperature show the expected behavior indicated by the red line. (b) Selection of mechanical displacement spectra, showing that the spectra are very clean.

temperature of 5.7 Kelvin. We have, however, noticed that the mode temperature increases with read-out laser power. For typical laser powers the mode temperature has increased from 5.7 to 6.5 Kelvin. The thermalization of the resonator is investigated in more detail in the next section.

The results are shown in Fig. 10.10 for an hour long, fully automated measurement. From the fitted red line, a value of 82 ± 2 kHz is obtained for the optical linewidth, showing that our system is side-band resolved. Furthermore, the excellent agreement between theory and experiment demonstrates that we have created a stable platform for sensitive optical experiments at low temperatures.

Figure 10.11 shows the results of side-band cooling when the cooling laser is fixed at $\Delta = -\Omega_m$ and the power is varied. The results follow theory nicely, as indicated by the red line. In Fig. 10.11(b) some of the mechanical displacement spectra are shown. Note that the scale on the y-axis is obtained by comparing the measurements with the calibrated side-of-fringe method of Fig. 10.9. At the highest laser powers an effective mechanical mode temperature of 3.6 ± 0.13 mK is achieved. As can be seen from Fig. 10.11(b), the mechanical spectra are very clean, thanks to the vibration isolation system and the nested resonator. When increasing the cooling laser power even further, the mechanical spectrum can no longer be distinguished from the noise floor anymore.

At low read-out laser powers, the noise floor is limited by shot noise. Increasing the laser power decreases the noise floor, but only down to the value shown in Fig. 10.11(b). A quick calculation [38] shows we are at least two orders of magnitude away from the shot noise limit. This suggests that additional technical noise dominates at these read-out powers. Furthermore, the noise floor has a definite slope. This becomes clearer when looking at the full power spectrum of the PDH error signal, as shown in Fig. 10.12. Up to 20 kHz the effects of the laser feedback are clearly visible, after which the noise floor gradually decreases. A decrease in noise floor with frequency suggest $1/f$ type noise, however, careful investigation

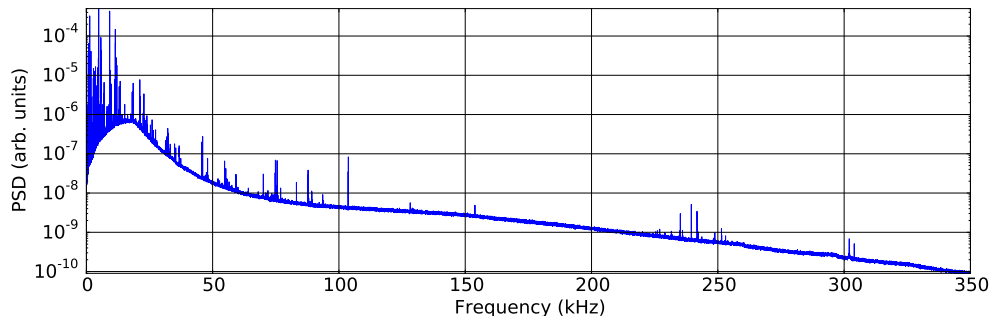


Figure 10.12: Full power spectrum of the PDH error signal. A clear downward slope is visible towards higher frequencies.

is needed. For example, the cavity itself acts as a low-pass filter, with the optical line-width κ as the corner frequency. This would, however, not explain the limit to the read-out noise.

Besides the read-out noise floor, we are also limited by the intrinsic Q-factor of the mechanical resonator. A higher Q-factor will directly result in a lower effective temperature, assuming all other parameters are fixed [97]. In the next section, the temperature of the cryostat is lowered with the dilution refrigerator. The hypothesis is that the lower base temperature together with optical cooling lead to a significantly lower effective mode temperature of the mechanical resonator than presented here for the base temperature of 5.7 K.

10.2.2 Thermalization of the trampoline resonator

Optical cooling from a base temperature of 5.7 Kelvin has resulted in an effective mode temperature of 3.6 mK. When lowering the base temperature to 100 mK, effective mode temperatures below 1 mK should be possible. Because the side-of-fringe method has limited sensitivity, the spectra measured at 5.7 Kelvin via the PDH technique, which is much more sensitive, can serve as a reference for determining the effective mode temperature at lower base temperatures. This does require a method to monitor the read-out sensitivity to be able to correct for any change in the read-out when cooling down from 5.7 K to mK temperatures. Therefore, a calibration tone at 304 kHz, generated by the same electric-optical modulator used for the Pound-Drever-Hall (PDH) technique, is added to the read-out laser.

Figure 10.13 shows the results of side-band cooling for a fixed laser detuning of $\Delta = -\Omega_m$ starting from a base temperature of 300 mK as measured with a RuO₂ thermometer. The effective linewidth increases with laser power, as is shown in Fig. 10.13(a). The effective temperature, however, does not continuously decrease with laser power. Furthermore, the lowest effective mode temperature that is achieved is 3.09 ± 0.07 mK, only slightly lower than the measurements performed at 5.7 K.

There are several possibilities why a lower base temperature does not lead to a significantly lower effective temperature. For example, the mechanical Q-factor

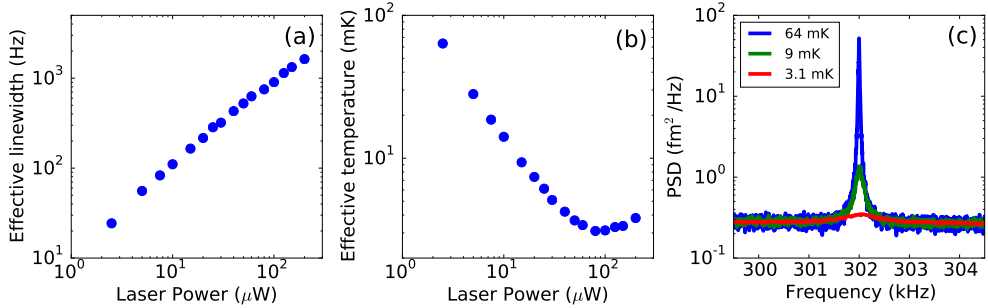


Figure 10.13: At a base temperature of 300 mK the laser detuning is fixed at $\Delta = -\Omega_m$ and the intensity of the pump laser is varied. (a) Effective line-width as function of laser power of the cooling beam. (b) Effective temperature as function of laser power of the cooling beam. (c) Selection of mechanical displacement spectra.

could have decreased when cooling down to mK temperatures. Another explanation is that the mechanical mode thermalizes poorly. Both explanations can be investigated by using the side-of-fringe technique shown in Fig. 10.9 to determine the intrinsic mechanical linewidth and the mode temperature.

The results in Fig. 10.14(a) show that the mechanical linewidth is roughly constant when the setpoint of the side-of-fringe lock is varied. The setpoint is the transmitted intensity to which the laser frequency is stabilized. The mode temperature increases significantly with increasing setpoint, as is shown in Fig 10.14(b). The temperature of the optical set-up was 200 mK during the entire measurement run and the measurements were performed from high to low setpoint. A higher setpoint means a larger transmitted intensity through the trampoline resonator, this suggests that heating of the mechanical mode due to optical absorption is the cause of the increased mode temperature. Another explanation is that the laser noise at the mechanical frequency of the resonator causes the mode temperature to increase. Laser noise can be ruled out as the cause of the increased mode temperature by repeating the experiment with a different laser at 1064 nm locked to the cavity resonance via the PDH technique. In Fig. 10.15 the mode temperature of the resonator is shown as function of read-out laser power for a base temperature of 5.7 K and 200 mK. The increase in read-out sensitivity with laser power is taken into account via the additional calibration tone. The read-out power displayed on the horizontal axis is the power in the optical fiber towards the optical set-up. At 5.7 K the read-out laser heats up the mechanical mode with approximately 1 K. The mode temperature increases even more at 200 mK, reaching a mode temperature of almost 4 K.

The increase in mode temperature with laser power is observed with two different lasers and two different measurement techniques. Also, at 200 mK the increase in temperature is larger for the same input power compared to measurements at 5.7 K. All these results can be explained by heating of the DBR mirror due to optical absorption and subsequently poor heat conduction through the silicon nitride arms. If we assume thermal equilibrium for the mechanical mode temperature when the

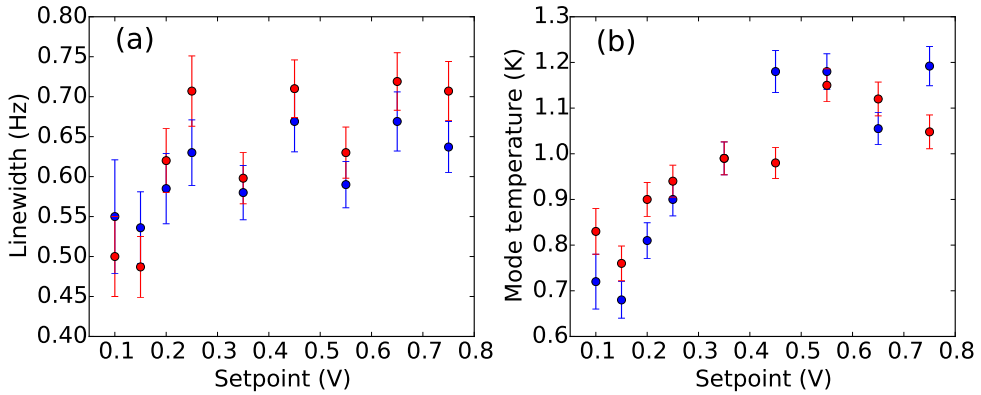


Figure 10.14: Via the side-of-fringe lock to a low finesse cavity, the mechanical linewidth shown in (a) and the mode temperature shown in (b) are obtained as a function of setpoint at a base temperature of 200 mK. Each setpoint is measured both on the blue side (blue points) and on the red side (red points) of the cavity resonance.

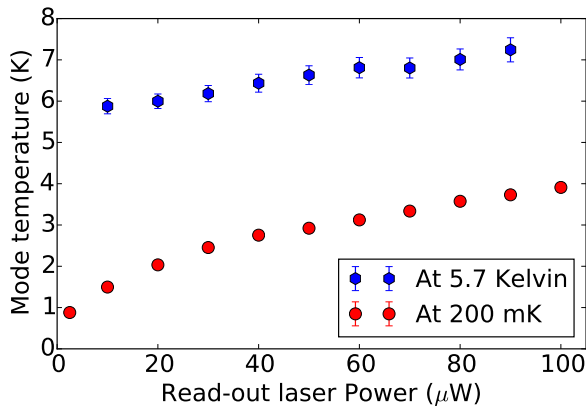


Figure 10.15: Comparison of the mode temperature as function of read-out laser power both at 5.7 K and approximately 200 mK.

laser is on, the heat conduction can be described by Fourier's law:

$$\frac{P_{abs}}{A} = -k \frac{dT}{dx} \quad (10.5)$$

where P_{abs} is the absorbed optical power, A is the cross-section perpendicular to the heat flow, k is the heat conductivity, and dT/dx the temperature gradient. Fourier's law might not be entirely valid for these small structures, but it will give a rough estimate. We can rewrite Eq. (10.5) in the following way to find the temperature difference between the DBR mirror and the support of the silicon nitride arms:

$$\Delta T = \frac{1}{4} \frac{P_{abs} \Delta x}{Ak} \quad (10.6)$$

where the factor $1/4$ accounts for the four arms of the resonator and Δx is the length of one arm. One silicon nitride arm has the following dimensions: $\Delta x = 175 \mu\text{m}$, $A = w \times t$ with a width $w = 50 \mu\text{m}$ and thickness $t = 400 \text{ nm}$. Zink and Hellman have investigated the thermal conductivity of low-stress amorphous silicon nitride membranes [133]. Although we use high stress silicon nitride, we can use their value of $k = 0.1 \text{ W}/(\text{K m})$ at 5 K as an estimate.

For $1 \mu\text{W}$ of optical read-out power in the fiber, we can estimate how much light leaks out of the cavity. With a mode-matching efficiency of 0.33 and a cavity coupling $\kappa_{ex}/\kappa = 0.15$, we estimate that 280 nW leaks out of the cavity through the trampoline resonator for $1 \mu\text{W}$ of optical power in the fiber. Suppose now that the DBR mirror on the trampoline resonator has 100 ppm transmission. The 280 nW of transmitted light corresponds to 100 ppm of the circulating power. Assuming 0.5 ppm of optical absorption in the DBR, this then corresponds to 1.4 nW of absorbed optical power. Of course, the silicon nitride layer underneath the DBR mirror can also absorb light. A quick estimate using the absorption coefficient of silicon nitride shows that this is at least an order of magnitude smaller than the absorption in the DBR mirror.

From Fig. 10.15 we see that $80 \mu\text{W}$ of read-out power at 5.7 K warms up the mode temperature with approximately 1 K. A read-out power of $80 \mu\text{W}$ corresponds to an estimated absorbed power of 112 nW. Using Eq. (10.6) this results in a temperature difference of 2.45 Kelvin. Although we have made several assumptions and guesses, (we have, for example, not taken the outer resonator into account) the fact that we find roughly the same value makes heating due to optical absorption plausible.

The thermal conductivity of silicon nitride at even lower temperatures is not well known, but generally the heat conductivity decreases when the temperature is lowered even further. This would explain the larger increase in mode temperature at 200 mK compared to the measurements at 5.7 K. Finally, heating of mechanical resonators due to optical absorption has been reported in literature as well. Experiments involving a silicon cantilever cooled to 300 mK show that the mechanical mode temperature increases significantly when only 70 nW of laser power is used for the optical read-out [134].

From Fig. 10.15 it is clear that there might be an optimal read-out power when performing an optical cooling experiment. However, this does not yet take heating due to the cooling beam into account. The measurements presented in Fig. 10.13 are performed with a read-out laser power of $20 \mu\text{W}$. As shown in Fig. 10.13, the effective

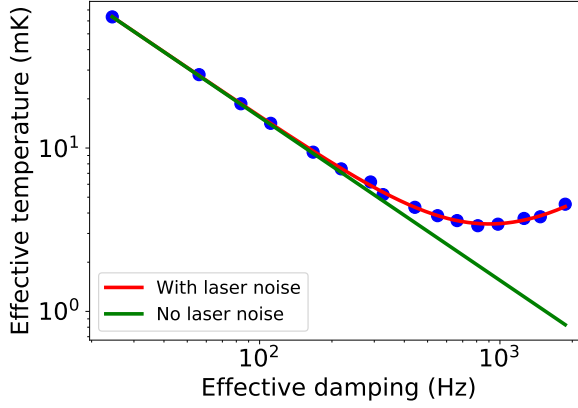


Figure 10.16: Effective mode temperature as function of effective damping. In red the fit is shown with the presence of classical laser noise, while in green the expected effective temperature is shown.

mode temperature increases again for high cooling beam powers, suggesting that also optical absorption of the pump beam occurs. The pump beam is placed at $\Delta = -\Omega_m$, so only 1.8 % of the pump beam is transmitted through the cavity compared to a detuning of $\Delta = 0$. Even with the high cooling laser powers used in 10.13, this fraction is simply too small to explain the increase in effective temperature shown in Fig. 10.13(b).

An alternative explanation is heating due to classical laser noise. As discussed in chapter 2, the effective temperature of the resonator can be written as

$$T_{\text{eff}} = \frac{T_{\text{env}}\Gamma_m + T_{\text{optical}}\Gamma_{\text{opt}}}{\Gamma_{\text{opt}} + \Gamma_m}. \quad (10.7)$$

Jayich et al. have shown how classical laser noise (amplitude and phase) affects the effective temperature [135]. We will not repeat the derivation, but using their assumption that the laser noise is proportional to the laser power, we can write Eq. (10.7) as follows:

$$T_{\text{eff}} = \frac{T_{\text{env}}\Gamma_m + T_{\text{optical}}(P_{\text{laser}})\Gamma_{\text{opt}}}{\Gamma_{\text{opt}} + \Gamma_m} \quad (10.8)$$

with $T_{\text{optical}}(P_{\text{laser}}) = \alpha P_{\text{laser}}$ this becomes

$$T_{\text{eff}} = \frac{T_{\text{env}}\Gamma_m + \alpha P_{\text{laser}}\Gamma_{\text{opt}}}{\Gamma_{\text{opt}} + \Gamma_m} \quad (10.9)$$

We can check the hypothesis of classical laser noise by using Eq. (10.9) to fit the data of Fig. 10.13(b). The results are shown in Fig.10.16. The data fit the theory well, indicating that classical laser noise is the problem. This might also explain why the noise floor of the read-out of the mechanical motion is not shot-noise limited. The solution would be to implement a filter cavity to reduce the classical laser noise [135].

The issue of optical absorption in DBR mirror of the trampoline resonator might be more difficult to solve. An alternative to trampoline resonators would be to use thin silicon nitride membranes, which can be used in a membrane-in-the-middle configuration. Because the membrane is placed at a node of the cavity field and the membrane is very thin (50 nm or less), optical absorption might not have such a big impact. Also, the mechanical Q-factor of these membranes is orders of magnitude larger. Both should help with achieving the quantum mechanical ground-state via optical side-band cooling. The next chapter discusses in more detail the advantages of membrane resonators.

Acknowledgment

We would like to thank Martin de Wit and Gesa Welker for operating the dilution refrigerator. We also thank Yasmine Sfindla for useful discussions.

Outlook: High-Q membranes, Coherent state transfer and Future directions

In the previous chapter we learned that optical absorption is one of the limiting factors in reaching the quantum mechanical ground-state. If the mechanical Q-factor of the trampoline resonator would be significantly higher, ultra low cryogenic temperatures are no longer needed which reduces the impact of optical absorption. Both issues, moderate Q-factor and optical absorption, can be addressed by replacing the trampoline resonator with a thin silicon nitride membrane. In this chapter we will give a brief introduction to silicon nitride membranes and compare them to our current trampoline resonators.

Apart from the issue of optical absorption, the optomechanical experiment in a cryogen free dilution refrigerator functioned as expected. It is therefore time to look at the generation of the superposition state needed to investigate gravitationally induced decoherence. The original idea proposed by Marshall [8] uses an optical cavity with a movable end mirror, just like our set-up. The optomechanical cavity is then combined with an additional cavity to form a Michelson interferometer to create entanglement between the path of the photon and the state of the mechanical resonator. In order to be able to measure any novel decoherence at all, the optomechanical coupling rate needs to be larger than the mechanical frequency. This requirement turns out not to be feasible. One solution would be to use a second mechanical resonator instead of an additional optical cavity. Via coherent optomechanical state transfer a superposition state between two mechanical resonators can be created. This idea, proposed by Matthew Weaver, is already explored experimentally in the classical domain, and some of the results will be discussed in this chapter.

Finally, we will briefly which optomechanical platform is the best to investigate the coherent state transfer. We take a closer look at photonic crystal nanobeam cavities. Because the mechanical frequency of the nanobeam can be in the GHz range,

Part of the work presented in this chapter is based on: M.J. Weaver, F.M. Buters, J. Luna, H. Eerrens, K. Heeck, S. de Man and D. Bouwmeester, "Coherent optomechanical state transfer between dissimilar mechanical modes", accepted for publication in Nature Communications (see arXiv:1704.02394)

cryogenic cooling suffices to prepare the system in the quantum mechanical ground-state. Combined with relatively high single-photon coupling rates, these systems are well suited to perform quantum experiments with mechanical resonators.

11.1 High-Q silicon nitride membranes

The current sample design, a trampoline resonator with a DBR mirror, has the advantage of the high quality mirror. This results in a high finesse optical cavity as is demonstrated in chapter 5. The downside however, is that the same DBR mirror introduces significant losses for the mechanical motion of the trampoline resonator. This has been investigated by M. Weaver and F. Luna at UCSB by comparing trampoline resonators with and without DBR mirror. Although the frequency increases by a factor of two for the resonator without mirror, the mechanical quality factor is also consistently higher by at least a factor of two. So far no progress has been made in reducing the mechanical losses introduced by the DBR mirror.

In addition to the cavity geometry used in this work, namely a cavity with a movable end mirror, a different geometry can also be used in which a silicon nitride membrane is placed in between two high quality mirrors. This membrane-in-the-middle approach has several advantages. For example, the coupling of the mechanical motion to the cavity field now depends on the position of the membrane with respect to a node or an anti-node of the cavity field. Positioning the membrane close to an anti-node results in a coupling that scales with the displacement squared [136]. Since the phonon number is directly proportional to the energy of the mechanical mode, which scales as x^2 , quantum non-demolition measurements [137] of the phonon number are directly possible [138], without the need for any back-action evading schemes [139]. Also, heating due to optical absorption, a big issue with the current trampoline resonators, can be minimized by placing the membrane at a node.

The most interesting aspect of these membrane-in-the-middle experiments, are the mechanical properties of the membrane itself. The mechanical frequency of these membranes is comparable to our trampoline resonators and also the mode-mass is similar. The mechanical quality factor, however, is much larger. Furthermore, these membranes are commercially available via Norcada Inc. As a demonstration of these high Q-factors, the mechanical properties of several modes of a 2×2 mm, 50 nm thick membrane (Norcada NX5200AS) are measured. The mechanical motion is monitored via a fiber interferometer, while the dielectric force is used for the excitation (see chapter 9). The experiment was conducted at a pressure of 1×10^{-5} mbar.

Figure 11.1(a) shows the mechanical ringdown of a higher order membrane mode, while in (b) the Q-factors for the fundamental and other higher order modes are shown. The Q-factor for the membrane modes is typically ten times higher than the Q-factor of our trampoline resonators. Furthermore, by optimizing the clamping of such a membrane, Q-factors as high as 50×10^6 at room temperature have been achieved using commercially available membranes [140]. Finally, several groups have fabricated custom membranes [141, 142] with Q-factors exceeding 100×10^6 . The current record is set by patterning a silicon nitride membrane with a phononic

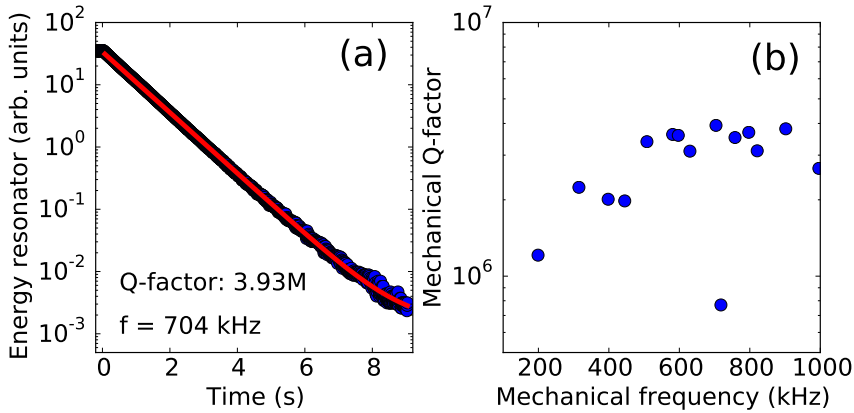


Figure 11.1: Mechanical quality factor of a commercially available silicon nitride membrane. (a) Mechanical ringdown of the (4,3) mode. (b) Mechanical quality factor for the fundamental and higher order modes.

crystal structure. A Q-factor of 214×10^6 is achieved at room temperature for a 777 kHz resonator with a mode-mass of 16 ng [143].

It is not difficult to see why a high-Q membrane will help in reaching the quantum mechanical ground-state. In the previous chapter, we achieved an effective mode temperature of 3.6 mK with optical cooling from a base temperature of 6 Kelvin. Suppose we keep all the parameters the same, including the sample design, and increase the Q-factor from 450×10^3 to 200×10^6 . The effective mode temperature will decrease from 3.6 mK to 8.1 μ K, which is cold enough for the resonator to be in the ground-state.

We can take this one step further. Suppose that we have placed a high-Q membrane at a node and therefore have reduced the optical absorption. Instead of a base temperature of 6 Kelvin, the temperature is lowered further. Typically the Q-factor increases when the temperature is lowered below 6 Kelvin [144]. As we have seen in chapter 10, the thermal conductivity of silicon nitride decreases significantly when the temperature is lowered below 6 Kelvin. This poses an interesting trade-off. The increase in Q-factor can directly be offset by the decrease in thermal conductivity even when heating due to optical absorption is negligible at 6 Kelvin.

Thermalization and optical absorption of membranes at mK temperatures has not been investigated extensively. Cryogenic and optical cooling have successfully been used by the Harris group to cool a commercial membrane to the quantum mechanical ground-state [97]. This involved a cryostat with a base temperature of 0.8 Kelvin and a commercial membrane with a Q-factor of 10×10^6 . It is, however, not beneficial for many other membrane experiments to perform measurements at temperatures below 1 Kelvin. For example, the experiment by the Harris group can also be conducted at 5 Kelvin, if the Q-factor is increased to 63×10^6 .

To summarize, because silicon nitride membranes can have such high Q-factors, dilution refrigerators are no longer required to reach the quantum mechanical ground-

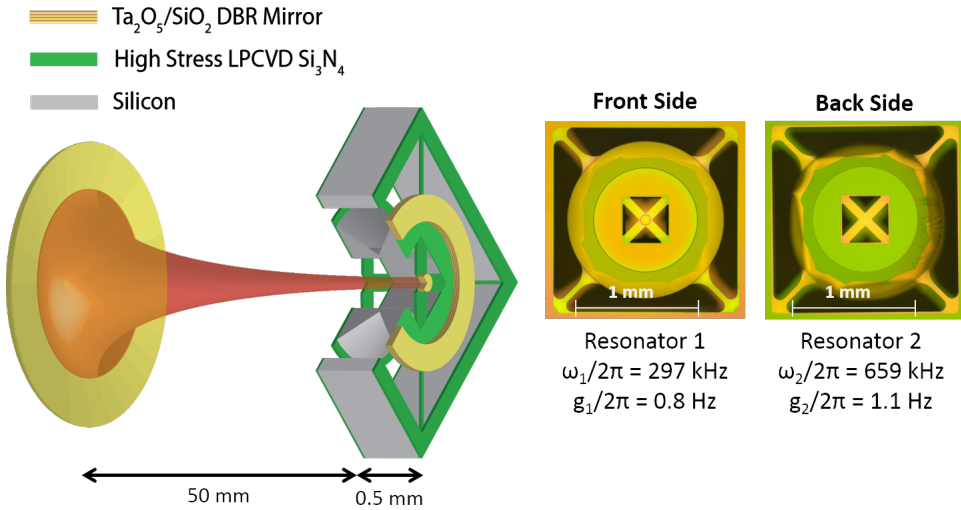


Figure 11.2: Schematic overview of the sample used to demonstrate optomechanical state transfer. The nested resonator design is modified to include a silicon nitride trampoline membrane on the back of the chip. The chip is then oriented such that the membrane sits in the middle of the cavity, and the trampoline resonator with DBR mirror acts as the end mirror of the cavity.

state. A base temperature of 6 Kelvin will suffice, which is beneficial for the heat conductivity of silicon nitride. Finally, optical absorption can be significantly reduced by placing the membrane at a node of the cavity field.

11.2 Coherent optomechanical state transfer

Let us first briefly discuss the idea of generating a superposition state with two mechanical resonators. Suppose two different mechanical resonators are both coupled to the same cavity mode. Furthermore, the two mechanical resonators are both in the quantum mechanical ground state. Via a weak coherent pulse, one resonator is excited to the first excited state. Because both resonators couple to the same optical field, it is possible to swap the excitation of one resonator to the other. If this transfer is done with a $\pi/2$ pulse, a superposition state between the resonators is created. The system can now be set to evolve for some time, after which another $\pi/2$ pulse can be used to bring back the excitation to the first resonator. Finally, a read-out pulse can be used to see if any decoherence has occurred.

The scheme described above requires two mechanical resonators coupled to the same cavity mode and the ability to optically couple the two mechanical resonators. Figure 11.2 shows a realization of two mechanical resonators coupled to the same cavity mode. The design of the nested resonator is expanded to include a silicon nitride trampoline membrane at the back of the chip. A membrane-in-the-middle cavity is created by adding this trampoline membrane. We have verified this ex-

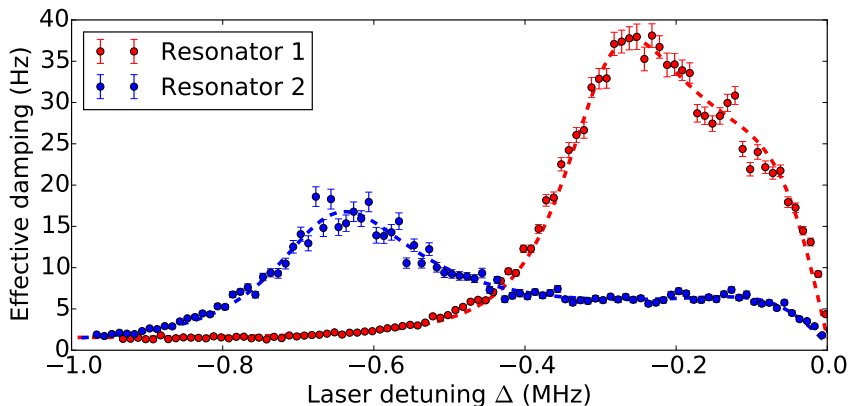


Figure 11.3: Effective damping as a function of laser detuning for a single laser drive. The optomechanical interaction of each resonator is well described by the theory presented in chapter 2.

perimentally by measuring the cavity finesse as function of wavelength, thereby changing the location of the nodes of the cavity field with respect to the trampoline membrane [138].

By measuring simultaneously the effective mechanical linewidth as a function of laser detuning for a single laser drive, see Fig. 11.3, we see that the interaction of each resonator with the optical field can be described by the theory presented in chapter 2. We also obtain an optical linewidth of 200 kHz and the optomechanical coupling g_0 for both mechanical resonators.

Although the resonators are located on the same chip, as is shown in Fig. 11.2, their frequency difference is sufficiently large for them to be mechanically decoupled. The coupling, therefore, is purely optical. Buchmann and Kurn have proposed a method to do this using two laser tones [145], of which the key points will be presented here. Figure 11.4(a) shows schematically the energy diagram for two harmonic oscillators. By choosing the laser frequencies carefully, laser 2 (ω_{L2}) can end up in a mode with the same frequency as laser 1 (ω_{L1}) after interacting with both mechanical resonators. In doing so, a phonon is exchanged from resonator 1 to resonator 2. The requirement for the laser frequencies, $\omega_{L2} + \omega_1 = \omega_{L1} + \omega_2$ can be rewritten as $\omega_{L2} - \omega_{L1} = \omega_2 - \omega_1$, which shows that the two laser tones should be separated by the difference of the mechanical frequencies. In Fig. 11.4(b) the two laser tones are shown together with the optical side-bands generated after interacting with both mechanical resonators. Two pairs of side-bands match up, precisely at the resonance condition for coherent state transfer.

Besides the state transfer, the two tones also generate the “normal” optomechanical effects, such as optical damping. To minimize these effects, both lasers are placed relatively far away from the cavity resonance at a detuning of $\Delta = (\omega_{L1} + \omega_{L2})/2 = -2.3$ MHz. These two tones are generated via an AOM using carrier suppressed side-band generation (see chapter 3). The mechanical motion of each resonator is

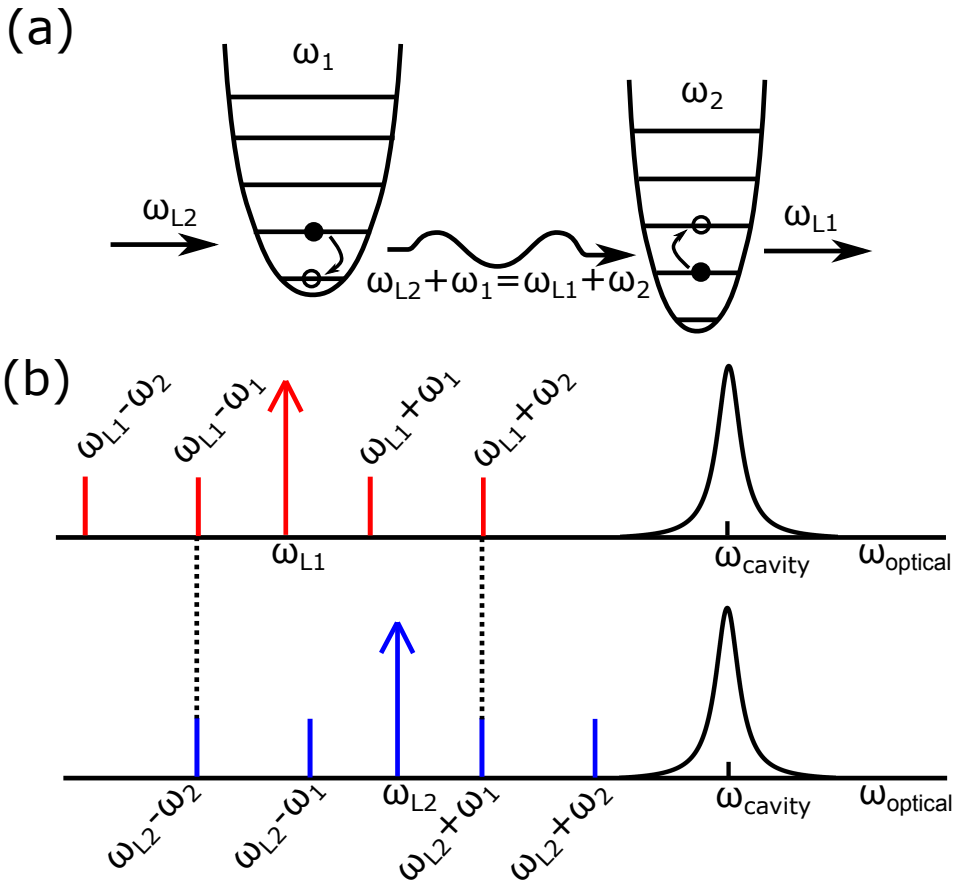


Figure 11.4: (a) Optomechanical state transfer using two laser tones occurs when the difference between the two laser frequencies is precisely the difference between the mechanical frequencies. (b) Schematic overview of the two laser tones together with optical side-bands generated after interacting with both mechanical resonators. Two pairs of side-bands match up, precisely at the resonance condition for coherent state transfer.

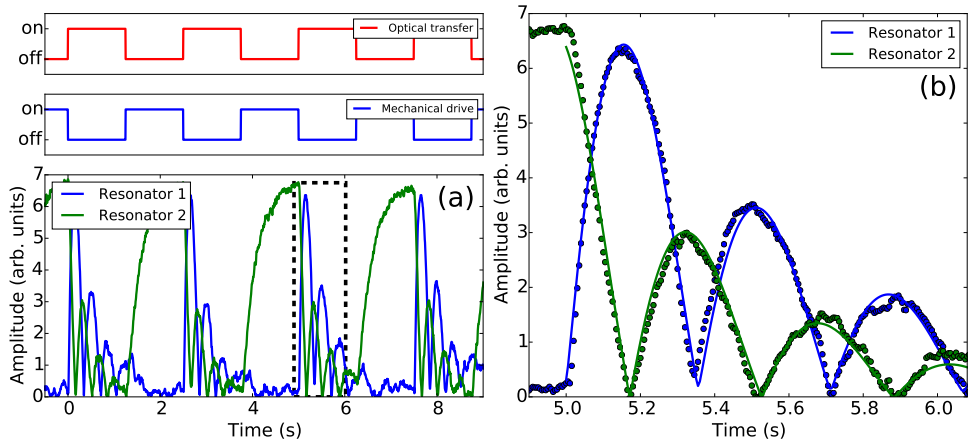


Figure 11.5: (a) Demonstration of optomechanical state transfer. The trampoline membrane, resonator 2, is driven via the dielectric force, after which the two tone laser drive periodically transfers the excitation back and forth between the two resonators. (b) Zoom of the outlined region in (a) showing that the coherent state transfer is well described by two coupled damped harmonic oscillators.

monitored via a probe beam locked with the Pound-Drever-Hall method (PDH) to a cavity resonance. The PDH error is used for feedback as well as for the read-out of the mechanical motion. Using a lock-in amplifier, the error signal is filtered in the frequency domain around the mechanical frequencies of the two resonators. In this way, the amplitude of mechanical motion is obtained.

A difference in energy between the two mechanical resonators is needed for any state transfer to take place. We achieve this by using actuation via the dielectric force, as demonstrated in chapter 9, to drive the trampoline membrane. The results are shown in Fig. 11.5. With the mechanical drive, the amplitude of resonator 2 is increased with respect to thermal motion. When the mechanical drive is turned off and the two lasers are turned on, optomechanical state transfer occurs and energy is periodically transferred between the two mechanical resonators. Figure 11.5(a) displays multiple of these cycles, showing that the transfer is very reproducible. With the two lasers turned on, the optomechanical system is well described by two coupled damped harmonic oscillators, as is shown in Fig. 11.5(b). Furthermore, the amplitude of motion of each resonator periodically drops back to the value corresponding to thermal motion, indicating full state transfer.

The measurements presented so far are a classical demonstration, but from Fig. 11.5 it is clear that an optical pulse of the correct length should be able to partially transfer energy from one resonator to the other, showing that a $\pi/2$ pulse is feasible. The next step is therefore to repeat these experiments at, or close to, the quantum mechanical ground-state together with a rigorous treatment of the quantum mechanical theory of state transfer. For example, both resonators should be cooled to the quantum mechanical ground state after which the state of both resonators can be entangled. As pointed out by Ludwig et al., this is theoretically already a non-trivial problem [146].

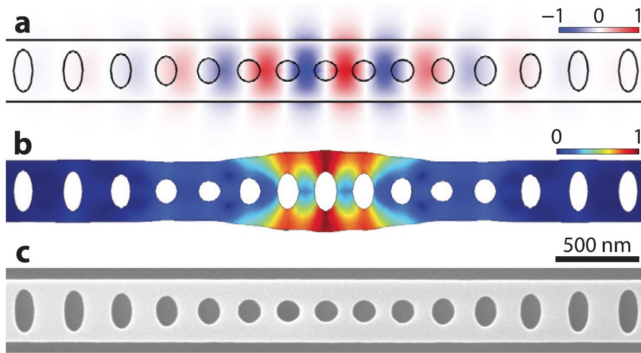


Figure 11.6: Photonic crystal nanobeam cavity in which the optical mode shown in (a) is co-localized with the mechanical mode shown in (b). The whole structure is only a couple of micrometers in size as is shown in the SEM image in (c). This figure is taken from Ref. [118].

11.3 The optimal platform to investigate optomechanical state transfer

The difficulties of ground-state cooling can be reduced by choosing a system with relatively high mechanical frequency, such that the mechanical ground-state can be reached by cryogenic cooling without additional optical cooling. This typically requires a \sim GHz mechanical frequency and mK temperatures. Of the few systems that operate in this regime, photonic crystal nanobeams cavities are a promising candidate for future experiments.

Figure 11.6 shows an example of a photonic crystal nanobeam cavity, as fabricated by the Painter group [118]. The optical mode spatially overlaps with the mechanical mode, creating strong optomechanical coupling. The whole structure is only a couple of micrometers in size. Due to the small mode volume of the cavity and the small mass of the resonator, the optomechanical coupling is quite strong. Furthermore, by decreasing the frequency from \sim GHz to \sim MHz frequencies, record high coupling rates were recently achieved [147].

We can make the comparison between different systems more quantitative by selecting the proper figure of merit. In chapter 4 the optomechanical cooperativity was introduced as $C = C_0 n_{cav}$ where n_{cav} is the cavity photon number and $C_0 = 4g_0^2/\kappa\Gamma_m$ is the single-photon cooperativity. Also the effect of side-band cooling can be expressed in terms of C . When the cooling laser is located at $\Delta = -\Omega_m$ the optical damping rate is given by $\Gamma_{opt} = \Gamma_m C$. As a reference, the system presented in this thesis has $C_0 = 0.003$.

In the quantum regime, the coherent state transfer discussed in the previous section requires single photons to excite one resonator from the ground state to the first excited state. This in turn requires a large single photon cooperativity to have a reasonable success rate. Photonic crystal nanobeam cavities with \sim GHz frequency resonators can have $C_0 = 3$ [148], while a modified design with \sim MHz frequency resonators have achieved $C_0 = 1.1 \times 10^3$ [147]. The trade-off, however, is that these

lower frequency resonators are not easily cooled to the ground state, even when cryogenic cooling is combined with optical cooling.

The potential of an optomechanical system which is cooled to the ground state by cryogenic means only, has recently been demonstrated [90]. By placing a photonic crystal cavity in a dilution refrigerator at a base temperature of 25 mK, the mechanical mode at 5.3 GHz was cooled to an average phonon occupation number of 0.025. Via a sequence of optical pulses, non-classical correlations between single photons and phonons have been observed.

These experiments involved a single cavity coupled to a single mechanical mode. Already photonic crystal cavities are fabricated in which a single mechanical resonator couples to two cavities [149], creating the equivalent of a membrane-in-the-middle system. A design for two mechanical resonators coupled to a single optical cavity is recently proposed to create an optomechanically induced effect analogous to a phononic band gap [150]. Furthermore, this design can also be used to investigate the optomechanical state transfer in the quantum regime.

Although the mode-mass of the nanobeam resonators might be too small for observing gravitationally induced decoherence, it would still be interesting to perform other quantum experiments such as an optomechanical Bell test [151] or observing phonon jumps [138]. Alternatively, because of the small size, a network of optomechanical cavities on a single chip can be created, which can lead to interesting many-body effects [152]. Finally, hybrid quantum networks can be constructed by coupling qubits such as quantum dots or NV centers to photonic crystal cavities [153].

Bibliography

- [1] J. Kepler, *De cometis libelli tres* (Avgvstae Vindelicorvm, 1619).
- [2] J. C. Maxwell, *Philosophical Transactions of the Royal Society of London* **158**, 643 (1868).
- [3] P. Lebedev, *Annalen der Physik* **311**, 433 (1901).
- [4] E. F. Nichols and G. Hull, *Physical Review (Series I)* **13**, 307 (1901).
- [5] M. Planck, *Annalen der physik* **309**, 553 (1901).
- [6] A. Einstein, *Annalen der physik* **322**, 132 (1905).
- [7] E. Schrödinger, *Naturwissenschaften* **23**, 807 (1935).
- [8] W. Marshall, C. Simon, R. Penrose, and D. Bouwmeester, *Physical Review Letters* **91**, 130401 (2003).
- [9] D. Kleckner, I. Pikovski, E. Jeffrey, L. Ament, E. Eliel, J. Van Den Brink, and D. Bouwmeester, *New Journal of Physics* **10**, 095020 (2008).
- [10] L. Diosi, *Physical Review A* **40**, 1165 (1989).
- [11] P. Pearle, *Physical Review A* **39**, 2277 (1989).
- [12] G. Ghirardi, R. Grassi, and A. Rimini, *Physical Review A* **42**, 1057 (1990).
- [13] R. Penrose, *General relativity and gravitation* **28**, 581 (1996).
- [14] B. Pepper, R. Ghobadi, E. Jeffrey, C. Simon, and D. Bouwmeester, *Physical Review Letters* **109**, 023601 (2012).
- [15] R. Ghobadi, S. Kumar, B. Pepper, D. Bouwmeester, A. Lvovsky, and C. Simon, *Physical Review Letters* **112**, 080503 (2014).

- [16] M. Aspelmeyer, T. J. Kippenberg, and F. Marquardt, *Reviews of Modern Physics* **86**, 1391 (2014).
- [17] A. Schließer, Ph.D. thesis, LudwigMaximiliansUniversity (2009).
- [18] R. Riviere, Ph.D. thesis, LudwigMaximiliansUniversity (2011).
- [19] C. Law, *Physical Review A* **51**, 2537 (1995).
- [20] F. Marquardt, J. P. Chen, A. Clerk, and S. Girvin, *Physical Review Letters* **99**, 093902 (2007).
- [21] I. Wilson-Rae, N. Nooshi, W. Zwerger, and T. Kippenberg, *Physical Review Letters* **99**, 093901 (2007).
- [22] A. Siegman, *Lasers* (University Science Books, 1986).
- [23] H. Haus, *Waves and fields in optoelectronics* (Prentice-Hall, 1984).
- [24] C. Gardiner and M. Collett, *Physical Review A* **31**, 3761 (1985).
- [25] A. Dorsel, J. McCullen, P. Meystre, E. Vignes, and H. Walther, *Physical Review Letters* **51**, 1550 (1983).
- [26] H. Nyquist, *Physical Review* **32**, 110 (1928).
- [27] H. B. Callen and T. A. Welton, *Physical Review* **83**, 34 (1951).
- [28] R. Kubo, *Reports on progress in physics* **29**, 255 (1966).
- [29] A. Clerk, M. Devoret, S. Girvin, F. Marquardt, and R. Schoelkopf, *Reviews of Modern Physics* **82**, 1155 (2010).
- [30] S. Mancini, D. Vitali, and P. Tombesi, *Physical Review Letters* **80**, 688 (1998).
- [31] A. Xuereb, R. Schnabel, and K. Hammerer, *Physical Review Letters* **107**, 213604 (2011).
- [32] H. Kogelnik and T. Li, *Applied Optics* **5**, 1550 (1966).
- [33] D. Kleckner, B. Pepper, E. Jeffrey, P. Sonin, S. M. Thon, and D. Bouwmeester, *Optics Express* **19**, 19708 (2011).
- [34] B. J. Pepper, Ph.D. thesis, University of California, Santa Barbara (2014).
- [35] M. J. Weaver, B. Pepper, F. Luna, F. M. Buters, H. J. Eerkens, G. Welker, B. Perrock, K. Heeck, S. de Man, and D. Bouwmeester, *Applied Physics Letters* **108**, 033501 (2016).
- [36] D. Kleckner, W. T. Irvine, S. S. Oemrawsingh, and D. Bouwmeester, *Physical Review A* **81**, 043814 (2010).
- [37] R. V. Pound, *Review of Scientific Instruments* **17**, 490 (1946).

- [38] E. D. Black, *American Journal of Physics* **69**, 79 (2001).
- [39] J. Teufel, T. Donner, D. Li, J. Harlow, M. Allman, K. Cicak, A. Sirois, J. Whittaker, K. Lehnert, and R. Simmonds, *Nature* **475**, 359 (2011).
- [40] J. Chan, T. M. Alegre, A. H. Safavi-Naeini, J. T. Hill, A. Krause, S. Gröblacher, M. Aspelmeyer, and O. Painter, *Nature* **478**, 89 (2011).
- [41] R. Riviere, S. Deleglise, S. Weis, E. Gavartin, O. Arcizet, A. Schliesser, and T. J. Kippenberg, *Physical Review A* **83**, 063835 (2011).
- [42] I. Pikovski, M. R. Vanner, M. Aspelmeyer, M. Kim, and Č. Brukner, *Nature Physics* **8**, 393 (2012).
- [43] M. Arndt and K. Hornberger, *Nature Physics* **10**, 271 (2014).
- [44] S. Gröblacher, K. Hammerer, M. R. Vanner, and M. Aspelmeyer, *Nature* **460**, 724 (2009).
- [45] A. Nunnenkamp, K. Børkje, and S. Girvin, *Physical Review Letters* **107**, 063602 (2011).
- [46] E. Verhagen, S. Deléglise, S. Weis, A. Schliesser, and T. J. Kippenberg, *Nature* **482**, 63 (2012).
- [47] V. Braginsky, S. Strigin, and S. P. Vyatchanin, *Physics Letters A* **287**, 331 (2001).
- [48] P.-F. Cohadon and S. Gras, in *Advanced Interferometers and the Search for Gravitational Waves* (Springer, 2014), pp. 315–331.
- [49] F. Marquardt, J. Harris, and S. Girvin, *Physical Review Letters* **96**, 103901 (2006).
- [50] M. Ludwig, B. Kubala, and F. Marquardt, *New Journal of Physics* **10**, 095013 (2008).
- [51] T. Carmon, H. Rokhsari, L. Yang, T. J. Kippenberg, and K. J. Vahala, *Physical Review Letters* **94**, 223902 (2005).
- [52] T. Kippenberg, H. Rokhsari, T. Carmon, A. Scherer, and K. Vahala, *Physical Review Letters* **95**, 033901 (2005).
- [53] F. Marino and F. Marin, *Physical Review E* **87**, 052906 (2013).
- [54] L. Bakemeier, A. Alvermann, and H. Fehske, *Physical Review Letters* **114**, 013601 (2015).
- [55] C. Metzger, M. Ludwig, C. Neuenhahn, A. Ortlieb, I. Favero, K. Karrai, and F. Marquardt, *Physical Review Letters* **101**, 133903 (2008).
- [56] V. Fiore, Y. Yang, M. C. Kuzyk, R. Barbour, L. Tian, and H. Wang, *Physical Review Letters* **107**, 133601 (2011).

- [57] J. T. Hill, A. H. Safavi-Naeini, J. Chan, and O. Painter, *Nature Communications* **3**, 1196 (2012).
- [58] A. H. Safavi-Naeini, T. M. Alegre, J. Chan, M. Eichenfield, M. Winger, Q. Lin, J. T. Hill, D. E. Chang, and O. Painter, *Nature* **472**, 69 (2011).
- [59] K.-J. Boller, A. Imamoglu, and S. E. Harris, *Physical Review Letters* **66**, 2593 (1991).
- [60] L. V. Hau, S. E. Harris, Z. Dutton, and C. H. Behroozi, *Nature* **397**, 594 (1999).
- [61] S. Weis, R. Rivière, S. Deléglise, E. Gavartin, O. Arcizet, A. Schliesser, and T. J. Kippenberg, *Science* **330**, 1520 (2010).
- [62] J. Teufel, D. Li, M. Allman, K. Cicak, A. Sirois, J. Whittaker, and R. Simmonds, *Nature* **471**, 204 (2011).
- [63] M. Karuza, C. Biancofiore, M. Bawaj, C. Molinelli, M. Galassi, R. Natali, P. Tombesi, G. Di Giuseppe, and D. Vitali, *Physical Review A* **88**, 013804 (2013).
- [64] J. Qin, C. Zhao, Y. Ma, X. Chen, L. Ju, and D. G. Blair, *Physical Review A* **89**, 041802 (2014).
- [65] W. H. P. Nielsen, Y. Tsaturyan, C. B. Møller, E. S. Polzik, and A. Schliesser, *Proceedings of the National Academy of Sciences* p. 201608412 (2016).
- [66] G. Agarwal and S. Huang, *Physical Review A* **81**, 041803 (2010).
- [67] H. Eerkens, F. Buters, M. Weaver, B. Pepper, G. Welker, K. Heck, P. Sonin, S. de Man, and D. Bouwmeester, *Optics Express* **23**, 8014 (2015).
- [68] R. W. Boyd and D. J. Gauthier, *Science* **326**, 1074 (2009).
- [69] O. Arcizet, P.-F. Cohadon, T. Briant, M. Pinard, and A. Heidmann, *Nature* **444**, 71 (2006).
- [70] A. Schliesser, R. Rivière, G. Anetsberger, O. Arcizet, and T. J. Kippenberg, *Nature Physics* **4**, 415 (2008).
- [71] A. Schliesser, O. Arcizet, R. Riviere, G. Anetsberger, and T. Kippenberg, *Nature Physics* **5**, 509 (2009).
- [72] T. Purdy, R. Peterson, P. Yu, and C. Regal, *New Journal of Physics* **14**, 115021 (2012).
- [73] A. H. Safavi-Naeini, J. Chan, J. T. Hill, T. P. M. Alegre, A. Krause, and O. Painter, *Physical Review Letters* **108**, 033602 (2012).
- [74] G. A. Phelps and P. Meystre, *Physical Review A* **83**, 063838 (2011).
- [75] T. Corbitt, Y. Chen, E. Innerhofer, H. Müller-Ebhardt, D. Ottaway, H. Rehbein, D. Sigg, S. Whitcomb, C. Wipf, and N. Mavalvala, *Physical Review Letters* **98**, 150802 (2007).

- [76] A. Borrielli, A. Pontin, F. Cataliotti, L. Marconi, F. Marin, F. Marino, G. Pandraud, G. Prodi, E. Serra, and M. Bonaldi, *Physical Review Applied* **3**, 054009 (2015).
- [77] J. C. Sankey, C. Yang, B. M. Zwickl, A. M. Jayich, and J. G. Harris, *Nature Physics* **6**, 707 (2010).
- [78] D. W. Brooks, T. Botter, S. Schreppler, T. P. Purdy, N. Brahms, and D. M. Stamper-Kurn, *Nature* **488**, 476 (2012).
- [79] V. Singh, S. Bosman, B. Schneider, Y. Blanter, A. Castellanos-Gomez, and G. Steele, *Nature nanotechnology* **9**, 820 (2014).
- [80] X.-Y. Lü, Y. Wu, J. Johansson, H. Jing, J. Zhang, and F. Nori, *Physical Review Letters* **114**, 093602 (2015).
- [81] A. Aspect, J. Dalibard, and G. Roger, *Physical Review Letters* **49**, 1804 (1982).
- [82] J.-W. Pan, M. Daniell, S. Gasparoni, G. Weihs, and A. Zeilinger, *Physical Review Letters* **86**, 4435 (2001).
- [83] E. Togan, Y. Chu, A. Trifonov, L. Jiang, J. Maze, L. Childress, M. G. Dutt, A. S. Sørensen, P. Hemmer, A. Zibrov, et al., *Nature* **466**, 730 (2010).
- [84] W. Gao, P. Fallahi, E. Togan, J. Miguel-Sánchez, and A. Imamoglu, *Nature* **491**, 426 (2012).
- [85] M. Paternostro, D. Vitali, S. Gigan, M. Kim, C. Brukner, J. Eisert, and M. Aspelmeyer, *Physical Review Letters* **99**, 250401 (2007).
- [86] D. Vitali, S. Gigan, A. Ferreira, H. Böhm, P. Tombesi, A. Guerreiro, V. Vedral, A. Zeilinger, and M. Aspelmeyer, *Physical Review Letters* **98**, 030405 (2007).
- [87] S. G. Hofer, W. Wieczorek, M. Aspelmeyer, and K. Hammerer, *Physical Review A* **84**, 052327 (2011).
- [88] P. Sekatski, M. Aspelmeyer, and N. Sangouard, *Physical Review Letters* **112**, 080502 (2014).
- [89] T. Palomaki, J. Teufel, R. Simmonds, and K. Lehnert, *Science* **342**, 710 (2013).
- [90] R. Riedinger, S. Hong, R. A. Norte, J. A. Slater, J. Shang, A. G. Krause, V. Anant, M. Aspelmeyer, and S. Gröblacher, *Nature* (2016).
- [91] S. Gröblacher, J. B. Hertzberg, M. R. Vanner, G. D. Cole, S. Gigan, K. Schwab, and M. Aspelmeyer, *Nature Physics* **5**, 485 (2009).
- [92] A. Jayich, J. Sankey, A. Petrenko, and J. Harris, in *Quantum Electronics and Laser Science Conference* (Optical Society of America, 2011), p. QThM3.
- [93] E. Kreyszig, *Differential geometry* (Dover Publications, 1991).

- [94] M. Uphoff, M. Brekenfeld, G. Rempe, and S. Ritter, *New Journal of Physics* **17**, 013053 (2015).
- [95] A. Weinstein, C. Lei, E. Wollman, J. Suh, A. Metelmann, A. Clerk, and K. Schwab, *Physical Review X* **4**, 041003 (2014).
- [96] T. P. Purdy, P.-L. Yu, N. S. Kampel, R. W. Peterson, K. Cicak, R. W. Simmonds, and C. A. Regal, *Physical Review A* **92**, 031802 (2015).
- [97] M. Underwood, D. Mason, D. Lee, H. Xu, L. Jiang, A. Shkarin, K. Børkje, S. Girvin, and J. Harris, *Physical Review A* **92**, 061801 (2015).
- [98] F. Diedrich, J. Bergquist, W. M. Itano, and D. Wineland, *Physical Review Letters* **62**, 403 (1989).
- [99] T. Hart, R. Aggarwal, and B. Lax, *Physical Review B* **1**, 638 (1970).
- [100] D. Rugar, H. Mamin, and P. Guethner, *Applied Physics Letters* **55**, 2588 (1989).
- [101] A. Gualdino, V. Chu, and J. Conde, *Journal of Applied Physics* **113**, 174904 (2013).
- [102] T. P. M. Alegre, A. Safavi-Naeini, M. Winger, and O. Painter, *Optics Express* **19**, 5658 (2011).
- [103] P.-L. Yu, K. Cicak, N. Kampel, Y. Tsaturyan, T. Purdy, R. Simmonds, and C. Regal, *Applied Physics Letters* **104**, 023510 (2014).
- [104] J. Hertzberg, T. Rocheleau, T. Ndikum, M. Savva, A. Clerk, and K. Schwab, *Nature Physics* **6**, 213 (2010).
- [105] E. E. Wollman, C. Lei, A. Weinstein, J. Suh, A. Kronwald, F. Marquardt, A. Clerk, and K. Schwab, *Science* **349**, 952 (2015).
- [106] J. Suh, A. J. Weinstein, C. U. Lei, E. E. Wollman, S. K. Steinke, P. Meystre, A. A. Clerk, and K. C. Schwab, *Science* **344**, 1262 (2014).
- [107] M. Bahrami, M. Paternostro, A. Bassi, and H. Ulbricht, *Physical Review Letters* **112**, 210404 (2014).
- [108] J. Milatz, J. Van Zolingen, and B. Van Iperen, *Physica* **19**, 195 (1953).
- [109] H. Hirakawa, S. Hiramatsu, and Y. Ogawa, *Physics Letters A* **63**, 199 (1977).
- [110] P.-F. Cohadon, A. Heidmann, and M. Pinard, *Physical Review Letters* **83**, 3174 (1999).
- [111] M. Pinard, P.-F. Cohadon, T. Briant, and A. Heidmann, *Physical Review A* **63**, 013808 (2000).
- [112] C. H. Metzger and K. Karrai, *Nature* **432**, 1002 (2004).
- [113] D. Kleckner and D. Bouwmeester, *Nature* **444**, 75 (2006).

- [114] M. Poggio, C. Degen, H. Mamin, and D. Rugar, *Physical Review Letters* **99**, 017201 (2007).
- [115] A. G. Krause, T. D. Blasius, and O. Painter, arXiv preprint arXiv:1506.01249 (2015).
- [116] D. Wilson, V. Sudhir, N. Piro, R. Schilling, A. Ghadimi, and T. J. Kippenberg, *Nature* **524**, 325 (2015).
- [117] I. Wilson-Rae, P. Zoller, and A. Imamoglu, *Physical Review Letters* **92**, 075507 (2004).
- [118] A. H. Safavi-Naeini, J. Chan, J. T. Hill, S. Gröblacher, H. Miao, Y. Chen, M. Aspelmeyer, and O. Painter, *New Journal of Physics* **15**, 035007 (2013).
- [119] Q. P. Unterreithmeier, E. M. Weig, and J. P. Kotthaus, *Nature* **458**, 1001 (2009).
- [120] K. Ekinci and M. Roukes, *Review of Scientific Instruments* **76**, 061101 (2005).
- [121] G. Binnig, C. F. Quate, and C. Gerber, *Physical Review Letters* **56**, 930 (1986).
- [122] G. D. Cole, I. Wilson-Rae, K. Werbach, M. R. Vanner, and M. Aspelmeyer, *Nature Communications* **2**, 231 (2011).
- [123] I. Wilson-Rae, R. Barton, S. Verbridge, D. Southworth, B. Ilic, H. Craighead, and J. Parpia, *Physical Review Letters* **106**, 047205 (2011).
- [124] P.-L. Yu, T. Purdy, and C. Regal, *Physical Review Letters* **108**, 083603 (2012).
- [125] E. Serra, A. Borrielli, F. Cataliotti, F. Marin, F. Marino, A. Pontin, G. Prodi, and M. Bonaldi, *Physical Review A* **86**, 051801 (2012).
- [126] G. M. Harry, L. S. Collaboration, et al., *Classical and Quantum Gravity* **27**, 084006 (2010).
- [127] S. Schmid, M. Wendlandt, D. Junker, and C. Hierold, *Applied Physics Letters* **89**, 163506 (2006).
- [128] A. Bouwers and P. Cath, *Philips Technisch Tijdschrift* **6**, 274 (1941).
- [129] A. Den Haan, G. Wijts, F. Galli, O. Usenko, G. Van Baarle, D. Van Der Zalm, and T. Oosterkamp, *Review of Scientific Instruments* **85**, 035112 (2014).
- [130] K. Heeck, Tech. Rep., Leiden Institute of Physics (2016).
- [131] B. Tellegen, *Philips Technical Review* **5**, 324 (1940).
- [132] G. A. Campbell, *Bell System Technical Journal* **1**, 1 (1922).
- [133] B. Zink and F. Hellman, *Solid State Communications* **129**, 199 (2004).
- [134] H. Mamin and D. Rugar, *Applied Physics Letters* **79**, 3358 (2001).

- [135] A. Jayich, J. Sankey, K. Børkje, D. Lee, C. Yang, M. Underwood, L. Childress, A. Petrenko, S. Girvin, and J. Harris, *New Journal of Physics* **14**, 115018 (2012).
- [136] J. Thompson, B. Zwickl, A. Jayich, F. Marquardt, S. Girvin, and J. Harris, *Nature* **452**, 72 (2008).
- [137] C. M. Caves, K. S. Thorne, R. W. Drever, V. D. Sandberg, and M. Zimmermann, *Reviews of Modern Physics* **52**, 341 (1980).
- [138] A. Jayich, J. Sankey, B. Zwickl, C. Yang, J. Thompson, S. Girvin, A. Clerk, F. Marquardt, and J. Harris, *New Journal of Physics* **10**, 095008 (2008).
- [139] A. Clerk, F. Marquardt, and K. Jacobs, *New Journal of Physics* **10**, 095010 (2008).
- [140] S. Chakram, Y. Patil, L. Chang, and M. Vengalattore, *Physical Review Letters* **112**, 127201 (2014).
- [141] R. A. Norte, J. P. Moura, and S. Gröblacher, *Physical Review Letters* **116**, 147202 (2016).
- [142] C. Reinhardt, T. Müller, A. Bourassa, and J. C. Sankey, *Physical Review X* **6**, 021001 (2016).
- [143] Y. Tsaturyan, A. Barg, E. S. Polzik, and A. Schliesser, arXiv preprint arXiv:1608.00937 (2016).
- [144] R. Fischer, N. Kampel, G. Assumpção, P.-L. Yu, K. Cicak, R. Peterson, R. Simmonds, and C. Regal, arXiv preprint arXiv:1611.00878 (2016).
- [145] L. Buchmann and D. Stamper-Kurn, *Physical Review A* **92**, 013851 (2015).
- [146] M. Ludwig, K. Hammerer, and F. Marquardt, *Physical Review A* **82**, 012333 (2010).
- [147] R. Leijssen, G. La Gala, L. Freisem, J. T. Muhonen, and E. Verhagen, arXiv preprint arXiv:1612.08072 (2016).
- [148] J. Chan, A. H. Safavi-Naeini, J. T. Hill, S. Meenehan, and O. Painter, *Applied Physics Letters* **101**, 081115 (2012).
- [149] T. K. Paraíso, M. Kalaei, L. Zang, H. Pfeifer, F. Marquardt, and O. Painter, *Physical Review X* **5**, 041024 (2015).
- [150] X. Xu, T. Purdy, and J. M. Taylor, arXiv preprint arXiv:1608.05717 (2016).
- [151] V. C. Vivoli, T. Barnea, C. Galland, and N. Sangouard, *Physical Review Letters* **116**, 070405 (2016).
- [152] M. Ludwig and F. Marquardt, *Physical Review Letters* **111**, 073603 (2013).
- [153] B. Hausmann, B. Shields, Q. Quan, Y. Chu, N. De Leon, R. Evans, M. Burek, A. Zibrov, M. Markham, D. Twitchen, et al., *Nano letters* **13**, 5791 (2013).

Samenvatting

In dit proefschrift is gekeken hoe stralingsdruk gebruikt kan worden om de beweging van een trampoline-resonator, een spiegeltje (80 micrometer diameter) vastge maakt aan vier dunne siliciumnitride armpjes, te reduceren. Dit optisch koelen is interessant omdat een combinatie van optische en cryogene koeltechnieken het mogelijk maakt deze resonator af te koelen naar de kwantummechanische grondtoestand. Dit is een vereiste voor vervolgent experimenten waarin de precieze grens van de kwantummechanica en de wisselwerking met zwaartekracht kan worden onderzocht. Hoofdstuk 1 geeft een korte introductie van deze experimenten.

Omdat de stralingsdruk zelf erg zwak is, is de bewegende spiegel onderdeel van een optische trillholte. Hierdoor botst het licht duizenden malen tegen de spiegel. Het effect van de stralingsdruk kan beïnvloed worden door de frequentie van het licht aan te passen ten opzichte van de resonantiefrequentie van de optische trillholte. Afhankelijk van deze frequentie is de stralingsdruk voornamelijk een optische veer of een optische demper. Met een optisch dempende kracht is het mogelijk om de mechanische beweging te reduceren en daardoor de resonator af te koelen. Naast theorie geeft hoofdstuk 2 ook een kort overzicht van de optische opstelling en de trampoline-resonator zelf.

Behalve optisch koelen is het ook mogelijk om de mechanische beweging optisch te versterken. In hoofdstuk 3 is de dynamica onderzocht van dit optisch aandrijven. Het effect van de stralingsdruk kan weergegeven worden in een attractordiagram. Bij een vaste laserfrequentie is de optische kracht aandrijvend, dan wel dempend afhankelijk van de precieze amplitude van de trampoline-resonator. De overgang tussen beide gebieden leidt tot instabiele en stabiele punten (attractors). Dit attractordiagram is verkend door de laserfrequentie te variëren en het licht dat terug komt van de trillholte te bestuderen en te vergelijken met simulaties. Hierbij is het mogelijk om specifieke contouren te bewandelen in het attractordiagram.

Waar hoofdstuk 3 laat zien dat een enkele laser de resonator optisch kan aandrijven, wordt in hoofdstuk 4 een manier met twee lasers gedemonstreerd. Eén laser

("probe") is resonant met de optische trilholtte. De frequentie van de tweede laser (pomp) is precies de mechanische frequentie lager dan de eerste laser. De stralingsdruk in de trilholtte varieert hierdoor met het frequentieverschil tussen beide lasers en drijft de resonator aan. De beweging van de resonator moduleert het licht in de trilholtte, wat leidt tot destructieve interferentie tussen het gemoduleerde licht en de "probe"-laser. De mate van destructieve interferentie zegt iets over de sterkte van de optomechanische interactie. De in hoofdstuk 4 beschreven methode is een handige manier om de gehele optomechanische interactie te karakteriseren.

Een andere manier om de optomechanische interactie te meten is door optisch te koelen. In hoofdstuk 5 wordt beschreven hoe, door de laserfrequentie een mechanische frequentie lager te zetten dan de optische resonantie frequentie, zijbandkoeling kan worden gedaan. Naast een laser om te koelen wordt gebruik gemaakt van een tweede laser voor de uitlezing van de beweging. Deze tweede laser is resonant met de optische trilholtte. Zowel de lengte van de trilholtte als de frequenties van de lasers variëren met de tijd. Om deze variaties tegen te gaan, wordt gebruik gemaakt van verschillende regelsystemen. De laser die gebruikt wordt voor de uitlezing wordt continu resonant gehouden met de trilholtte via een regelaar. De tweede laser wordt, via een andere regelaar, op variabele afstand gezet van de eerste laser. Door de frequentie van de tweede laser te variëren, is het effect van de laserfrequentie op de mechanische beweging onderzocht.

Naast intensiteit en frequentie kan ook de polarisatie van het licht aangepast worden. Dit kan interessant zijn wanneer de optische trilholtte zich anders gedraagt voor de ene polarisatie dan voor de andere. De spiegel op de trampoline-resonator is niet vlak maar een beetje bol door de stress in het materiaal van de spiegel. Samen met de vier siliciumnitride armpjes zorgt dit ervoor dat de bolle spiegel twee kromtestralen heeft die loodrecht op elkaar staan. Hierdoor heeft de optische trilholtte voor horizontaal en verticaal gepolariseerd licht een andere frequentie. In hoofdstuk 6 wordt beschreven en gedemonstreerd hoe deze opsplitsing gebruikt kan worden voor optomechanische experimenten.

Tijdens de metingen van hoofdstuk 5 is opgemerkt dat de analyse van de data aanzienlijk bemoeilijkt wordt door aanwezigheid van extra signalen. Dit is verder onderzocht in hoofdstuk 7. Numerieke simulatie van het volledige experiment laat zien dat laagfrequente lengteveranderingen van de optische trilholtte een groot effect kunnen hebben, maar dat deze in principe kunnen worden gecompenseerd door de laserfrequentie aan te passen. In het tweede deel van hoofdstuk 7 is onderzocht of het vastklemmen van het sample van invloed is op de mechanische eigenschappen. Door het sample in te klemmen tussen dun indiumfolie is een goed mechanisch contact mogelijk, waardoor de mechanische eigenschappen positief beïnvloed worden en de additionele signalen aanzienlijk worden onderdrukt. Hieruit is geconcludeerd dat mechanische bewegingen van het substraat de trampoline-resonator beïnvloeden. Door de trampoline-resonator te omringen met een grotere resonator (buiten-resonator) wordt de koppeling tussen het substraat en de trampoline-resonator (binnen-resonator) sterk gereduceerd.

Hoofdstuk 8 laat zien dat met deze dubbele resonator optisch koelen tot 23 mK vanaf kamertemperatuur mogelijk is. Daarnaast wordt in hoofdstuk 8 een model van de dubbele resonator besproken om te verklaren waarom voor sommige laser-

frequenties de beweging van de resonator niet stabiel is. Dit heeft geleid tot de implementatie van een elektrische methode om de buiten-resonator te stabiliseren, beschreven in hoofdstuk 9. Via een elektrode, vlak achter de dubbele resonator, is het mogelijk om een elektrische veldgradiënt aan te brengen waarmee electrostatisch een kracht op de buiten-resonator kan worden uitgeoefend. Hierdoor is zogenaamde actieve "feedback"-koeling mogelijk, alsmede het stabiliseren van de lengte van de trilholtte.

In hoofdstuk 10 worden alle technieken van voorgaande hoofdstukken gecombineerd in een experiment bij lage temperaturen. De opstelling is vastgemaakt aan een trillingsisolatie-platform beschreven in het eerste deel van hoofdstuk 10. Dit geheel is geplaatst in een cryostaat. De mechanische beweging van de trampoline-resonator is uiteindelijk, via optisch koelen, afgekoeld tot 3 mK beginnende vanaf 6 Kelvin. De limiterende factor voor de eind-temperatuur blijkt de optische absorptie van het licht door de spiegel en de slechte warmtegeleiding door de siliciumnitride armpjes te zijn.

Het laatste hoofdstuk blikst vooruit naar een volgend experiment. Twee losse resonatoren kunnen optisch aan elkaar gekoppeld worden wanneer ze beide interactie hebben met de trilholtte. Hierdoor is het mogelijk om energie van de ene resonator door te geven aan de andere en weer terug. Dit is vooral interessant wanneer beide resonatoren zich in, of vlakbij, de kwantummechanische grondtoestand bevinden. De twee resonatoren kunnen dan zo aan elkaar gekoppeld worden dat er kwantumverstrengeling ontstaat. Een variant op dit experiment maakt gebruik van twee verschillende mechanische modes van één resonator. Dit heeft als voordeel dat een nieuw type resonator, een siliciumnitride membraan gebruikt kan worden. Niet alleen hebben zulke membranen uitstekende mechanische eigenschappen, door deze op een knoop midden in de trilholtte te plaatsen kan de optische absorptie geminimaliseerd worden. Hiermee kan het probleem beschreven in hoofdstuk 10 worden opgelost.

Acknowledgment

I would like to take this opportunity to thank some people without whose help this work was not possible. I would like to thank my promotor Dirk Bouwmeester for providing me with the freedom, confidence and possibilities during my PhD.

The last four years I was part of a research team with scientists from Leiden and the University of California, Santa Barbara. From the Leiden team, I would like to thank Sven de Man for his help and guidance with the experiments, but also with the non-scientific challenges. The majority of the experiments presented in this thesis have been performed together with Hedwig Eerkens. It was nice to have someone to share the good and the bad times with. Four years I shared a desk with Kier Heeck, whose positive attitude and vast knowledge of almost all things technical were vital for this project. I would also sincerely like to thank Harmen van der Meer of the Fine Mechanics department. Whatever he fabricated, large or small, it was always perfect. Finally, before I started in Leiden, Petro Sonin and Evan Jeffrey have done a lot of the ground work for this project. I am grateful to both.

Across the ocean, my colleagues in Santa Barbara designed and fabricated the trampoline resonators. Early devices were fabricated by Brian Pepper, while Matthew Weaver and Fernando Luna have fabricated the majority of the devices used in this thesis. Your visits to Leiden were always fun and inspiring. Good luck to both of you with finishing your PhD.

I had the pleasure to work with several students during my PhD. I would like to thank Myles Huang in particular, who has spend almost two years in our group. I would also like to thank the Quantum Optics group members for the nice and interesting discussions during the coffee break and lunch. A special thanks to Wolfgang Löffler. His willingness to always help out in the lab, with proofreading articles, with referee replies or with science in general, is invaluable. I would like to thank Henriëtte van Leeuwen for the administrative support.

Finally I would like to thank my parents and brother for their love and support during my PhD.

Curriculum vitae

Frank Buters was born on the 20th of October 1989 in Velsbroek. He graduated cum laude from the Gymnasium Felisenum high school in 2008 with a specialization in natural sciences and went to study physics at the Vrije Universiteit Amsterdam. Frank obtained his BSc cum laude. His final research project involved photocatalysis of NaTaO_3 crystals in the group of Rinke Wijngaarden. He went on to do an MSc at the Vrije Universiteit Amsterdam with a focus on experimental condensed matter physics. In 2012 he was elected to attend the Lindau Nobel meetings. He performed his final research project on the optical properties of SiGe nanocrystals in the group of Tom Gregorkiewicz at the University of Amsterdam and obtained his MSc cum laude in 2013. He then moved to Leiden to work on the optomechanics experiment in the group of Dirk Bouwmeester. As of September 2017 Frank is working as a consultant at RiskQuest in Amsterdam.

List of publications

1. **F.M. Buters**, K. Heeck, F. Luna, M.J. Weaver, H. Eerkens, S. de Man and D. Bouwmeester, *Vibration free platform for cavity optomechanics*, in preparation (Chapter 10 of this thesis)
2. M.J. Weaver, **F.M. Buters**, J. Luna, H. Eerkens, K. Heeck, S. de Man and D. Bouwmeester, *Coherent optomechanical state transfer between dissimilar mechanical modes*, accepted for publication in Nature Communications (Chapter 11 of this thesis)
3. **F.M. Buters**, F. Luna, M. Weaver, H.J. Eerkens, K. Heeck, S. de Man, and D. Bouwmeester, *Optomechanically induced transparency with a trampoline resonator*, Optics Express 25, 12935 (2017) (Chapter 4 of this thesis)
4. **F.M. Buters**, K. Heeck, H. Eerkens, M. J. Weaver, F. Luna, S. de Man, and D. Bouwmeester, *High-nested resonator in an actively stabilized optomechanical cavity*, Appl. Phys. Lett. 110, 104104 (2017) (Chapter 9 of this thesis)
5. **F.M. Buters**, M.J. Weaver, H.J. Eerkens, K. Heeck, S. de Man, and D. Bouwmeester, *Optomechanics with a polarization non-degenerate cavity*, Phys. Rev. A 94, 063813 (2016) (Chapter 6 of this thesis)
6. M.J. Weaver, B. Pepper, F. Luna, **F.M. Buters**, H.J. Eerkens, G. Welker, B. Percock, K. Heeck, S. de Man, and D. Bouwmeester, *Nested trampoline resonators for optomechanics*, Appl. Phys. Lett. 108, 033501 (2016)
7. **F.M. Buters**, H. J. Eerkens, K. Heeck, M.J. Weaver, B. Pepper, S. de Man, and D. Bouwmeester, *Experimental exploration of the optomechanical attractor diagram and its dynamics*, Phys. Rev. A 92, 013811 (2015) (Chapter 3 of this thesis)
8. H. J. Eerkens, **F.M. Buters**, M.J. Weaver, B. Pepper, G. Welker, K. Heeck, P. Sonin, S. de Man, and D. Bouwmeester, *Optical side-band cooling of a low fre-*

- quency optomechanical system*, Optics Express 23, 8014 (2015) (Chapter 5 of this thesis)
9. **F.M. Buters**, H. J. Eerkens, K. Heeck, M.J. Weaver, B. Pepper, P. Sonin, S. de Man, and D. Bouwmeester, *Large parametric amplification in an optomechanical system*, Physica Scripta T165, 014003 (2015) (Chapter 3 of this thesis)
 10. S. Saeed, **F.M. Buters**, K. Dohnalova, L. Wosinski, and T. Gregorkiewicz, *Structural and optical characterization of self-assembled Ge nanocrystal layers grown by plasma-enhanced chemical vapor deposition*, Nanotechnology 25, 405705 (2014)